

Quantitative investigation of the cycling behavior and SEI formation via the time-resolved mass spectrometry

Von der Fakultät Chemie der Universität Stuttgart zur Erlangung der Würde eines
Doktors der Naturwissenschaften (Dr. rer. nat.) genehmigte Abhandlung

Vorgelegt von

Ke Wang

Aus Henan, China

Hauptberichter: Prof. Dr. Dr. h. c. Guido Schmitz

Mitberichter: Prof. Dr. Joachim Maier

Prüfungsvorsitzender: Prof. Dr. Oliver Clemens

Tag der mündlichen Prüfung: 23. 02. 2023

Institut für Materialwissenschaft (IMW) der Universität Stuttgart

2023

Erklärung über die Eigenständigkeit der Dissertation

Ich versichere, dass ich die vorliegende Arbeit mit dem Titel Quantitative investigation of the cycling behavior and SEI formation via the time-resolved mass spectrometry

selbständig verfasst und keine anderen als die angegebenen Quellen und Hilfsmittel benutzt habe; aus fremden Quellen entnommene Passagen und Gedanken sind als solche kenntlich gemacht.

Declaration of Authorship

I hereby certify that the dissertation entitled

Quantitative investigation of the cycling behavior and SEI formation via the time-resolved mass spectrometry

is entirely my own work except where otherwise indicated. Passages and ideas from other sources have been clearly indicated.

Name/Name: Ke Wang

Unterschrift/Signed: _____

Datum/Date: _____

Abstract

As part of overcoming the environment and energy problem, rechargeable lithium-ion batteries (LIB) have brought great convenience to our lives and have attracted intensive research. However, the capacities of commercial lithium-ion batteries have not reached the desired level, especially for the requirements of automobiles. The Solid Electrolyte Interphase (SEI) which can protect the electrode from a continuous corrosion causes a high irreversible specific capacity fade during initial battery charging. Due to the complex formation process, a systematic research of its instability, microstructure, chemical composition is desired.

In this work, the long-term SEI formation process and cycling behavior on anodes based on the fourth group of the periodic table including Silicon (Si) germanium (Ge) and tin(Sn) were investigated by combining quartz crystal microbalance (QCM) with electrochemical Cyclic Voltammetry (CV), where the composition of species loaded and uploaded on the electrode are identified by their mass per charge (MPE) which is calculated by combining the data from QCM and CV. Furthermore, scanning electron microscopy, transmission electron microscopy, X-ray diffraction and X-Ray Photoelectron Spectroscopy were also processed to corroborate the conclusions of QCM-CV.

In the case of Sn: three different experimental characteristics namely mass spectra, real-time MPE and average MPE were combined for the study on the long-term SEI formation. During the long-term cycling, various stages in the evolution of the SEI are identified. Except the organic and inorganic SEI layer formed in first cycle, the SEI is continuously affected by the formation of inorganic SEI (probably Li_2O and Li_2CO_3) during lithiation in the second stage and the oxidation of

Sn during de-lithiation in the second and third stages. Furthermore, apart from Li storage, reversible processing of Li_2O contributes 23% of the capacity of a 100 nm Sn anode. Based on the model of the SEI formation and cycling behavior on Sn, the influence of the voltage window and the electrode thickness on SEI formation were further investigated. Remarkably, SEI thickness reveals a linear relation to the electrode thickness which is linked to continuous cracking and oxidization of Sn. A critical thickness (X_0) is introduced to describe that SEI formation is first dominated by cracking ($X_{\text{Sn}} > X_0$), and later by diffusion ($X_{\text{Sn}} \leq X_0$). Furthermore, the density calculation clarifies the roles of the organic species. Surprisingly, after serious fracture of Sn, QCM mass spectrometry confirms that a significant amount of Li_2O is cycled reversibly. This reversible contribution clearly increases with the sample thickness. Despite the general belief that the SEI should be formed before the lithiation, SEI, mainly composed of Li_2O and Li_2CO_3 , unexpectedly forms in the voltage range of 0.36 to 0.27 V simultaneous to the lithiation. This part of the SEI plays the most important role on stabilizing the electrode. Suppressing this inorganic SEI by an unsuitable voltage window, the electrode continuously cracks and finally becomes a fully porous layer. We believe that our quantitative investigation on Sn would be similarly applicable to other electrode materials.

Also on Ge anode, the QCM mass spectroscopy identifies Li_2O as a reversibly processed species that contributes a significant part to the electrochemical capacity. The amount of reversibly stored Li_2O decreases weakly with increasing cycling rate but increases significantly with the thickness of the Ge anodes. Interestingly, the amount of Li_2O decreases, if pronounced anode cracking appears, which is probably attributed to the fact that the fracture introduces short circuit transport paths deep into the volume of the Ge which accelerates lithiation. Furthermore,

a direct comparison between Si and Ge anodes indicates that the formation of Li_2O and the insertion of Li are competitive reactions and the amount of reversible Li_2O also depends on the onset potential of lithiation, which provides a good foundation for balancing the interfacial and bulk storage of Li.

Kurzfassung

Im der Bewältigung des Umwelt- und Energieproblems haben wiederaufladbare Lithium-Ionen-Batterien (LIB) unser Leben sehr erleichtert und sind Gegenstand intensiver Forschung. Allerdings, die Kapazitäten der handelsüblichen Lithium-Ionen-Batterien haben noch nicht das gewünschte Niveau erreicht, speziell für die Anforderungen von Kraftfahrzeugen. Die feste Elektrolyt-Zwischenphase (Solid Elektrolyte Interphase, SEI), die die Elektrode vor einer kontinuierlichen Korrosion schützen kann, verursacht einen hohen irreversiblen Verlust der spezifischen Kapazität während der ersten Batterieladung. Aufgrund des komplexen Entstehungsprozesses sollten die Instabilität, Mikrostruktur und chemische Zusammensetzung der SEI systematisch untersucht werden.

In dieser Arbeit wurden der langfristige SEI-Bildungsprozess und das Zyklusverhalten auf Anoden, aus der vierten Gruppe des Periodensystems, speziell Germanium (Ge) und Zinn (Sn), durch die Kombination von elektrochemischer Quarzkristallmikrowaage (QCM) und zyklischer Voltammetrie (CV) untersucht. Dabei wird die Zusammensetzung der auf die Elektrode deponierten oder desorbierten und hochgeladenen Spezies durch Ihre Masse pro Ladung (MPE) identifiziert, die durch die Kombination der Daten aus QCM und CV berechnet wird. Darüber hinaus wurden Rasterelektronenmikroskopie, Transmissionselektronenmikroskopie, Röntgenbeugung und Röntgenphotoelektronenspektroskopie durchgeführt, um die Ergebnisse der QCM-CV zu bestätigen.

Im Falle von Sn: Drei verschiedene Merkmale, darunter Massenspektren, Echtzeit-MPI und durchschnittliche MPE, wurden für die Gesamt- und die segmentierte Studie über die langfristige.

Entwicklung der SEI kombiniert. Während der Zyklisierung werden verschiedene Stadien der SEI-Bildung beobachtet. Abgesehen von der organischen und anorganischen SEI-Schicht, die im ersten Zyklus abgeschieden wird, wird die SEI kontinuierlich durch die Bildung von anorganischer SEI (zumeist Li_2O und Li_2CO_3) während der Lithiierung, im zweiten und die Oxidation von Sn während der De-Lithiierung im zweiten und dritten Stadium beeinflusst. Darüber hinaus trägt neben der Li-Speicherung auch die reversible Deposition von Li_2O zu 23 % der Kapazität der 100 nm Sn-Anode bei. Auf der Grundlage des Modells der SEI-Bildung und des Zyklusverhaltens auf Sn wurde der Einfluss des Spannungsfensters und der Elektrodendicke auf die SEI-Bildung weiter untersucht. Bemerkenswerterweise zeigt die SEI-Dicke eine lineare Beziehung zur anfänglichen, die mit kontinuierlicher Rissbildung und Oxidation von Sn zusammenhängt. Es wird eine kritische Dicke (X_o) eingeführt, um zu beschreiben, dass die SEI-Bildung zunächst durch Rissbildung ($X_{sn} > X_o$) und später durch Diffusion ($X_{sn} \leq X_o$) dominiert wird. Darüber hinaus liefert die Dichteberechnung Hinweise auf die Rolle der organischen Spezies. Überraschenderweise bestätigt die QCM nach einem starken Bruch von Sn, dass eine beträchtliche Menge an Li_2O reversibel umgewandelt wird. Dieser Beitrag nimmt mit zunehmender Probendicke deutlich zu. Entgegen der allgemeinen Annahme, dass sich die SEI innerhalb der Lithiierungs Halb-Zyklus vor der Lithiierung bilden sollte, bilden sich SEI, die hauptsächlich aus Li_2O und Li_2CO_3 bestehen, unerwartet in einem Spannungsbereich von 0.36 bis 0.27 V gleichzeitig mit der Lithiierung, vorwiegend im Stadium Zwei. Dieser Teil der SEI spielt die wichtigste Rolle bei der Stabilisierung der Elektrode. Wenn diese anorganische SEI durch ein ungeeignetes Spannungsfenster verhindert wird, bekommt die Elektrode kontinuierlich Risse und wandelt sich schließlich zu einer vollständig porösen Schicht.

Wir glauben, dass unsere quantitative Untersuchung von Sn in ähnlicher Weise auch auf andere Elektrodenmaterialien übertragbar ist.

Im Falle der Ge Anoden: Die QCM-Massenspektroskopie identifiziert Li_2O als eine reversibel deponierte Spezies, die einen erheblichen Teil zur elektrochemischen Kapazität beiträgt. Die Menge an reversibel gespeichertem Li_2O nimmt mit zunehmender Zyklusrate nur geringfügig ab, steigt jedoch deutlich mit der Dicke der Ge-Anoden. Interessanterweise nimmt die Menge an Li_2O ab, wenn eine ausgeprägte Rissbildung an der Anode auftritt, was wahrscheinlich darauf zurückzuführen ist, dass der Bruch Kurzschluss-Transportwege tief in das Ge-Volumen einführt, was die konkurrierende Lithiierung beschleunigt. Darüber hinaus zeigt der direkte Vergleich zwischen Si- und Ge Anoden, dass die Bildung von Li_2O und die Einlagerung von Li konkurrierende Reaktionen sind und die Menge des reversiblen Li_2O auch vom der thermodynamischen Stabilität der LiGe-Phase Diese Untersuchungen legen eine Reihe von Parametern offen um die Anteile von Grenzflächen und Volumen Speicherung zu kontrollieren.

Table of contents

Abstract.....	I
Kurzfassung.....	IV
Table of contents	VII
1 Introduction	1
1.1 Rechargeable Li-ion Battery.....	2
1.1.1 Working principle	2
1.1.2 Electrode.....	4
1.1.1.1 Anode materials.....	5
1.1.1.2 Cathode materials.....	8
1.1.3 Electrolyte.....	10
1.1.3.1 Solvent.....	11
1.1.3.2 Lithium-based salts	12
1.2 Solid electrolyte interphase.....	13
1.2.1 The formation of solid electrolyte interphase	13
1.2.2 The model of the anode electrolyte interphase.	14
1.2.3 Techniques for studying solid electrolyte interphases.....	16
1.2.3.1 Characterization of phase structure	17
1.2.3.2 Morphology.....	18
1.2.3.3 Characterization of chemical composition	19
1.3 Quartz crystal microbalance	20
1.3.1 Working principle	20
1.3.2 Application of QCM for LIB research	22
1.3.2.1 Gravimetry with other techniques.....	23
1.3.2.2 Gravimetry with dissipation.....	24
1.3.2.3 Studying the long-term SEI formation and cycling behavior on electrodes (anodes)	26

1.4	Motivation.....	27
2	Experimental methods and data analysis.....	28
2.1	Thin film sample deposition.....	28
2.1.1	DC ion-beam sputter deposition.....	29
2.1.2	RF ion-beam sputter deposition.....	29
2.2	Structural characterization.....	30
2.2.1	Scanning electron microscopy (SEM).....	30
2.2.2	Transmission electron microscopy (TEM).....	30
2.2.3	X-ray diffractometer (XRD).....	31
2.2.4	X-ray photoelectron spectroscopy (XPS).....	31
2.3	In-situ mass measurement during electrochemical processing.....	32
2.4	Data analysis.....	33
2.4.1	Capacity.....	33
2.4.2	Mass from QCM.....	33
2.4.3	Mass per charge.....	34
2.4.4	Mass from CV and the amount of Li_2O	35
2.4.5	Time-resolved mass spectra.....	36
3	In situ characterization of the SEI formation on Sn anode by using a quartz crystal microbalance.....	37
3.1	Microstructure of as-deposited Sn thin film.....	38
3.2	Electrochemical performance of Sn anode.....	39
3.3	The SEI formation at a 100 nm Sn anode.....	40
3.4	A top-down (from overall to detail) analysis strategy.....	44
3.5	Characterization of the electrode before and after cycling.....	57
3.6	In-situ SEI formation of SnO_x	60
3.7	Summary.....	62
4	The effect of Sn thickness and working potential window on the SEI growth and cycling behavior of Sn.....	65

4.1	Microstructure of Sn thin films with different thickness.....	66
4.2	Electrochemical performance of Sn anodes of different thickness.....	66
4.3	The SEI formation and cycling behavior on 20 nm Sn	69
4.4	The dependence of SEI growth on the Sn thickness.....	73
4.5	The SEI formation in dependence on potential window of cycling.....	81
4.6	Conclusion.....	89
5	Quantitative investigation of the reversible Li_2O formation on Germanium anodes using time-resolved microgravimetry	91
5.1	The microstructure of as-deposited Ge thin film	92
5.2	100 nm thick Ge film cycled between 0.1 V - 1.5V vs Li/Li ⁺ at 0.5mV/s	92
5.3	100 nm thick Ge film cycled between 0.3 V – 1.5 V vs Li/Li ⁺ at 0.5mV/s	97
5.4	20 nm thick Ge film cycled between 0.3 V – 1.5 V vs Li/Li ⁺ at 0.5mV/s	99
5.5	20 nm thick Ge film cycled between 0.3 V – 1.5 V vs Li/Li ⁺ at different scan rates (from 0.125mV/s to 16mV/s).....	101
5.6	Li_2O formation mechanism: Silicon vs Germanium	103
5.7	Conclusion.....	109
6	Conclusion.....	110
7	Outlook	113
	References	115
	Acknowledgement	126
	Appendix	128
	List of Figures	136
	List of Tables	141
	List of publication (2019-2022).....	142
	Curriculum vitae.....	143

1 Introduction

There is no doubt that continuous and excessive consumption of fossil fuels has caused serious environmental pollution and exacerbated energy shortage¹. Thus, an energy transition away from fossil fuels to renewable energy is required. Meanwhile, larger scale of electric energy storage plays an important role for various demands, especially the electric vehicles (EVs). Furthermore, for small scale consumer electronics, many kinds of commercial batteries or capacitors are currently in use and have broad convenience in our daily lives. As shown in Fig 1.1 (a), the lithium ion battery is one of the most promising candidate for EVs market based on its combination of high specific power and energy². However, there is still a certain distance to achieve the EV target defined by the United States Advanced Battery Consortium (USABC), where the targets of USABC is 235 Wh kg⁻¹ pack level (350 Wh kg⁻¹ cell level) cycled at least 1000 cycles³. Moreover, the lithium-ion batteries as one of the important solutions to achieve carbon neutrality are rapidly increasing in demand. As shown in Fig 1.1 (b), the amount of EV sales are projected to increase from today's volume all over the world by one order of magnitude until 2040 predicted by U.S. energy information administration⁴. Therefore, under the huge demand, it is urgent to develop lithium-ion batteries to attain above target for competitive EVs.

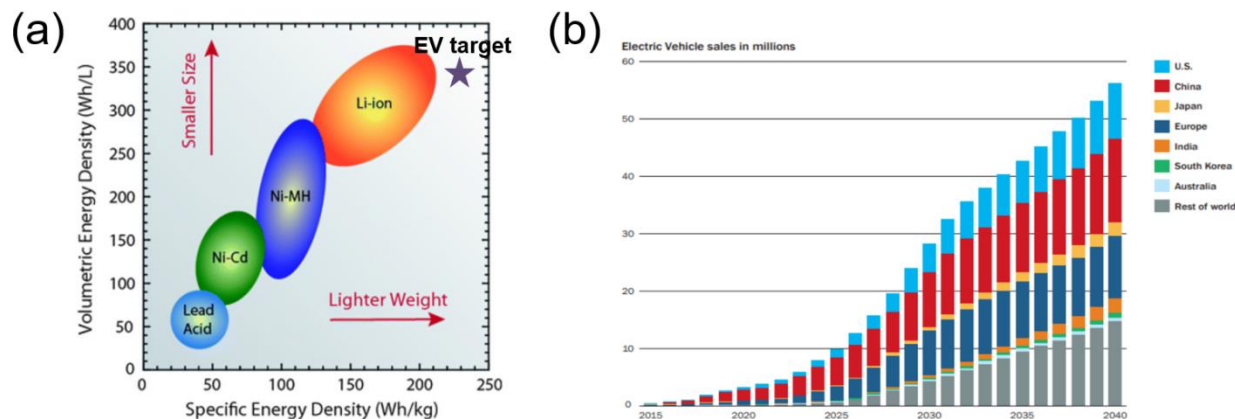


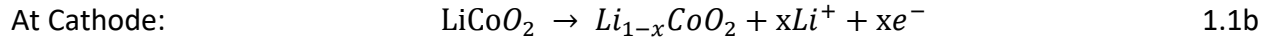
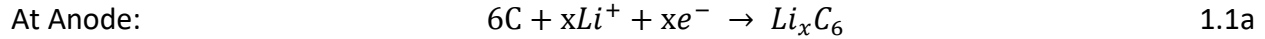
Figure 1.1: (a) Specific Energy densities of different kinds batteries (source: www.epectc.com), (b) Annual sales of the electric vehicle (source: BloombergNEF Long-Term Electric Vehicle Outlook 2019).

1.1 Rechargeable Li-ion Battery

1.1.1 Working principle

The principle of electrochemical battery was invented more than 200 years ago, and the first electrochemical cell was built using zinc and silver plates separated by a cloth soaked in sodium chloride solution. This provided a model that each cell consists of two electrodes that are in contact with an electrolyte and connected to the external electrical circuit of the battery⁵. Subsequently, many kinds of battery were invented such as lead acid battery or the nickel-iron (or cadmium) battery. But with the increase in demand for high energy and power density battery, Li metal with low density (0.534 g/cm^3), high theoretical capacity (3860 mAh/g) and alternative reduction potential (-3.04 V vs a standard hydrogen electrode [SHE]) was firstly used as the negative electrode for “rocking chair” style rechargeable lithium battery by M. Stanley Whittingham in 1970s⁶. However, owing to the risk taken by the lithium dendrites, in 1991, rechargeable Li-ion battery was first commercialized by Sony. They used hard carbon^{7,8} as anode

material and LiCoO_2 as cathode (reported by Goodenough in 1981⁹) for their battery, which undergoes chemical reactions according to the equation 1.1a and 1.1b:



The processes of discharge and charge are schematically plotted in Fig. 1.2

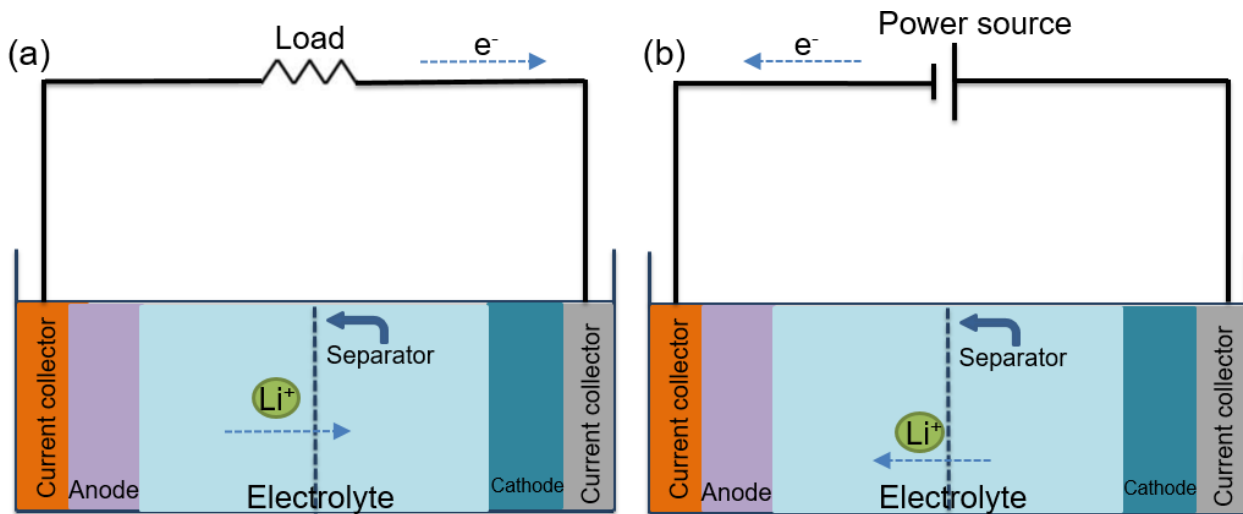


Figure 1.2: (a) Discharging and (b) charging of a lithium ion battery.

During charging the battery, due to the applied electric field, the lithium ions move from the cathode through the electrolyte to the anode. Among discharge, the Li stored in the anode with high chemical potential can move back to the cathode. Meanwhile, to maintain electrical neutrality of electrode, the electrons in the outer circuit also move from anode to cathode to generate a current and provide energy. It is worth mentioning that the electrolyte should be a non-electronic conductor, otherwise, the flow of electrons and lithium ions through electrolyte will cause short circuit and will only generate heat¹⁰.

1.1.2 Electrode

The electrodes in a LIB consist of active material (Li insertion and de-insertion) and current collector foil (conduct the flow of electrons) where the active material are always coated on the top of current collector. Typically, aluminum is chosen as the current collector on the cathode side, while copper is selected as the current collector on the anode side due to their electrochemical stability at the working potential of the corresponding electrode. Usually, active material should mix with polymeric binder and conductive carbon which enhances the mechanical integrity of the electrode and increase the electronic conductivity between particles of the active material and the current collector, respectively¹¹. As shown in equation 1.2, the electrical energy ($E_{battery}$) is not only dominated by the amount of charge/ions, but also depended on the electrochemical potential between cathode ($U_{cathode}$) and anode (U_{anode}). Thus, the ideal electrode should be able to insert or extract more lithium in a wider potential window to obtain a high electrochemical capacity.

$$E_{battery} = \int I \cdot (U_{cathode} - U_{anode}) \cdot dt \quad 1.2$$

Various anodes and cathodes which can be used in a lithium ion battery are summarized in Fig. 1.3 (a) and (b), respectively.

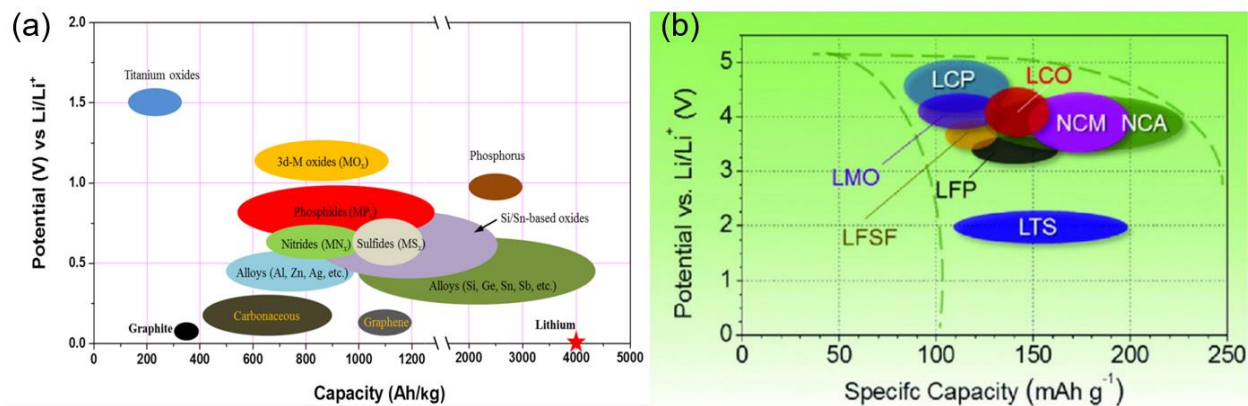


Figure 1.3: Comparison between specific capacity and operating potential of various anode materials (a)¹² and cathode materials (b)¹³.

1.1.1.1 Anode materials

As discussed in section 1.1.1, the anode serves as an acceptor of lithium ions during charging of a battery i.e. itself it needs to operate at low potentials. The ideal anode is Li, attributed to its big specific capacity and low reduction potential of -3.04 V vs the standard hydrogen electrode¹⁴ or zero with respect to itself. However, due to inhomogeneous deposition of Li on the surface of lithium metal during charging, the formed 'lithium-dendrites' can penetrate the separator and short-circuit the cell¹⁵. In order to overcome the security risk of lithium dendrites, different concept have been proposed¹⁶. For example, Li et al. added lithium polysulfide and lithium nitrate in an ether-based electrolyte. The formed solid electrolyte interphase (SEI) effectively prevented dendrite growth and minimized the electrolyte decomposition¹⁷. However, the sensitivity of lithium to the ambient atmosphere poses great difficulties to its characterization. Until now, the working mechanism of lithium metal batteries is still poorly understood and the commercial application of pure Li anodes is still a challenge.

Nowadays, many kinds of carbonaceous material such as graphite, hard carbon and graphene are commercially used as anodes of LIB. The operating potential is between 0.1 - 0.2 V vs Li/Li⁺, while the amount of reversible Li insertion depends on the structure of carbonaceous material. For example, in case of highly ordered graphitic carbon, six carbon atoms serving as host can accept insertion of up to one lithium atom, which sums up to a theoretical specific capacity of 372 mAh g⁻¹¹⁸. In addition, Li can also be absorbed into the microporous structures of hard carbons or hydrogen containing carbons which increases the theoretical specific capacity^{19,20}. However, their high hygroscopicity, their low density and the degradation of the capacity when cycled at high current density limited their commercial value²¹.

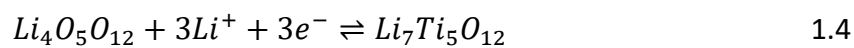
Beside the intercalation of Li into the host, Li can also reversibly alloy with several kinds of metals or semiconductors, especially those in the IV group of the periodic table (Si, Ge and Sn). As show in equation. 1.3



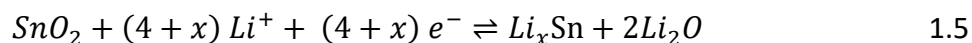
When fully lithiated to Li₂₂M₅, the theoretical capacity of Silicon (Si), Germanium (Ge) and Tin (Sn) are 4200 mAh g⁻¹, 1570 mAh g⁻¹ and 990 mAh g⁻¹, respectively, while the corresponding onset voltages of alloying are 0.6 V, 0.5 V and 0.4 V (for the initial LiM phase)²². Unfortunately, the huge volume expansions caused by the formation of the Li₂₂X₅ intermetallic phase leads to fracture of electrode and consequently continuous formation of SEI during cycling, which decreases the stability of the electrode and causes a continuous capacity fade²³. To overcome their drawback, research has demonstrated that the morphology of anodes plays a key role for their stability. For example, Si, Ge and Sn nanowires exhibit very stable capacity since fracturing is largely

suppressed. Furthermore, a composite of Si-C also shows long-cycle stability. Considering price, capacity, stability and preparation, the Si-C anode is one of the promising candidates for the next generation anode material in LIB.

In addition to the elemental anodes, some compounds like oxides²⁴, nitrides²⁵, phosphides²⁶, and $\text{Li}_4\text{Ti}_5\text{O}_{12}$ (LTO) can also serve as anode of LIBs. As shown in equation 1.4, the spinel type LTO enables reversible Li insertion based on a two phase reaction occurring at 1.55 V vs $\text{Li}^+/\text{Li}^{\cdot}$ of this material. It is worth to mention that there is almost no volume expansion during the lithiation, and the lithiation occurs within the electrochemical stability window of most electrolytes. Thus, LTO has ultra-long cycle life²⁸. However, the low electronic conductivity and specific capacity (175 mAh g^{-1} or 60.8 $\mu\text{Ah cm}^{-2} \mu\text{m}^{-1}$) hinder its further application.



Furthermore, as shown in equation 1.5, except the alloying with Sn, for SnO_2 anode, the reversible transfer between SnO_2 and Sn provide extra capacity (around 711 mAh g^{-1})²⁹. In view of the limited inter-diffusion depth, the sustained reversible conversion into SnO_2 only occurred with small particles. However, the large surface area of the nanoparticles is considered to cause poor initial coulombic efficiency and also the mechanical fractures of SnO_2 leading to complete pulverization should be prevented for further application³⁰.



1.1.1.2 Cathode materials

Cathode materials are typically oxides of transition materials, which can undergo oxidation to higher valences to maintain charge neutrality when lithium is removed. The electrochemical potential of cathodes is dominated by the electrons in d orbitals, mostly 3d orbitals³¹. Furthermore, in view of the phase changes affected by the large compositional changes, a stable crystal structure over wide ranges of composition is preferable³². According to the structure classification, cathode materials can be divided into three main categories³³: layer structure (LiMO_2), spinel (LiM_2O_4) and Olivine (LiMPO_4).

Cathodes with layer structure

Layered LiCoO_2 (LCO) has been the first commercial cathode used in Li-ion battery and is still used in many kinds of portable devices like cell phones, laptops and cameras. Li atoms occupy alternate layers between anion sheets, they are intercalated into or de-intercalated out of the host layers, which results in a relatively high theoretical specific capacity of 274 mAh g^{-1} and an onset voltage of over 4.2 V vs Li^+/Li ³⁴. However, during the delithiation, LCO is not stable and the crystalline structure will be changed if more than 50% of lithium de-intercalate out of the electrode. Thus, the practical specific capacity of LCO is limited to half of its high theoretical specific capacity (around 140 mAh g^{-1})³⁵. In addition, less availability of Co, and therefore its high cost in comparison to other transition metals is another issue which limits commercial value of LCO currently.

Co may be substituted by Nickel (Ni) to obtain LiNiO_2 (LNO) which has similar crystalline structure as LCO³⁶. Ni is much cheaper than Co, but the lower thermodynamical stability of LNO and less order compared to LCO, still hinder the large-scale commercialization of LNO³⁷. Additionally,

mixing other transition metals into LNO, such as Co and aluminum, can significantly improve electrochemical performance and its stability³⁸. The cathode $\text{LiNi}_x\text{Co}_y\text{Al}_z\text{O}_2$ ($x+y+z=1$) has already been used in electric vehicle such as Tesla and Pruis α . The high-cost and difficulty of NCA preparation can still be optimized in the future.

In addition of Ni, Co or Ni and Co, LiMnO_2 can also be synthesized with layer structure³⁹. Inevitably, the transformation from layered structure to spinel structure during the delithiation leads to the leaching of Manganese (Mn) resulting in unstable electrochemical properties³⁹. Practically, Ni, Co and Mn are usually combined in different stoichiometry to obtain $\text{LiMn}_x\text{Co}_y\text{Ni}_z\text{O}_2$ ($x+y+z=1$) which has good capacity and stability⁴⁰. Furthermore, the stoichiometry of Ni, Co and Mn can be adjusted to meet application requirements. Ni and Co work as active atom, while Mn only improves the stability and safety⁴¹.

Furthermore, due to its remarkable theoretical specific capacity more than 350 mAh/g and practical specific capacity more than 250 mAh/g, Li-rich Mn-based cathode (LRMO) $x\text{Li}_2\text{MnO}_3 \cdot (1-x)\text{LiMO}_2$ ($M = \text{Mn, Co, Ni, Fe, Cr, etc.}$) have been considered as promising cathodes for the next generation power batteries⁴². However, the large initial irreversible capacity, poor rate capability, severe voltage decay and security risk derived from the oxygen evolution hinder large-scale commercialization of LRMO. Many strategies such as doping, protective coating and reduction of the size of the material have been used to improve its electrochemical performance⁴³. Possibly, in the near future we can see its commercial use in our daily life.

Cathodes with spinel structure

In the spinel LiMn_2O_4 , the Li^+ ions occupy the tetrahedral sites within the Mn_2O_4 polyhedral frameworks adjacent to empty octahedral sites, has a reasonable theoretical specific capacity of 148 mAh/g (fully delithiated). Similar to cathodes with layer structure, irreversible structural changes occur when too much lithium is de-intercalating from the cathode, thus, the practical specific capacity of LiMn_2O_4 is around 110-120 mAh/g⁴⁴. Due to its lower cost, $\text{Li}_{1+x}\text{Mn}_{2-x}\text{O}_4$ prepared by using more Li partly replacing Mn exhibits better rate capability and has been used in electric vehicle such as Nissan leaf and Chevy volt⁴⁵.

Cathodes with olivine structure

LiFePO_4 (LFP) was first reported as cathode materials by Goodenough et. al in 1997. Li^+ and Fe^{2+} atoms are located in octahedral sites and the phosphorus occupies tetrahedral sites in a hexagonal close-packed oxygen array⁴⁶. As a commercial LIB, LFP exhibits around a moderate capacity of 170mAh/g, but a relatively low equilibrium voltage of 3.4 V vs Li^+/Li . In addition, carbon coated nano-LFP was proposed to balance for the poor Li-ion diffusion coefficient ($10^{-10} \text{ cm}^2/\text{s}$) and low electronic conductivity (10^{-10} S/cm) of LFP⁴⁷. Due to its low cost and safety, LFP also have been used in many EV especially BYD⁴⁸.

1.1.3 Electrolyte

The electrolyte in Li-ion battery cells blocks the direct contact of the two electrodes, and enables Li-ion diffusion between the cathode and anode. The electrolyte is mainly composed of two parts: solvent and Li-based salts. Fundamentally, as the electrolyte of LIB, it should meet the following requirements^{49,50}:

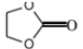
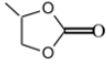
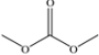
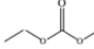
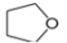
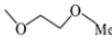
1. No reacting with electrodes.

2. Stable in a wide temperature, and a wide electrochemical window (with electrode passivation).
3. Fast ion transport around $10^{-3} - 10^{-2}$ S/cm.
4. Good compatibility with other parts in LIB, like electrode, current collector and separator.
5. Low cost, safe and environment friendly.

1.1.3.1 Solvent

Solvent as the main part of electrolyte should have good electrochemical stability, high dielectric constant, high solubility for lithium salt, high boiling and low melting temperature and low viscosity. Table.1 summarize the physical and chemical property of the common organic carbonate and ether solvents⁴⁹.

Table 1.1: Overview of typical electrolyte solvent used in LIB⁴⁹

solvent	structure	melting temperature (°C)	Viscosity (cp 25°C)	Dielectric constant
EC		36.4	1.9 (40°C)	89.78
PC		-48.8	2.53	64.92
DMC		4.6	0.59	3.107
EMC		-53	0.65	2.958
THF		-109	0.46	7.4
DME		-58	-0.46	7.2
AN	$\text{H}_3\text{C}-\text{C}\equiv\text{N}$	-43.8	3	0.37

The data of Table 1.1 show it is difficult for a single solvent to meet all requirements of the ideal solvent, as mentioned above. Practically, two or more solvents are mixed to be used on electrolyte. For example, liquid solvents, such as EC/DMC and EC/DEC, are widely known in commercial application.

Besides, Polymer/gel combining the advantages of the liquid solvents and solid solvents is another promising solvent candidate for LIBs, Such as Poly(vinylidene fluoride) and Poly(ethylene oxide)⁵¹.

1.1.3.2 Lithium-based salts

The function of the lithium salt is to provide lithium ions and lithium ion conduction. Thus, lithium salt should have strong polarity (easily soluble in solvents), small binding energy between anions and lithium ions, good electrochemical stability and good passivation of Al (the corrosion of Al is occurred upon anodic polarization (> 4.0 V vs. Li/Li⁺))⁵². The physical and chemical property of the common lithium-based salts are shown in Table 1.2⁴⁹.

Table 1.2: Overview of lithium salts used in LIB⁴⁹

Lithium salt	Molecular mass g/mol	Decomposition temperature °C	Conductivity in (EC/DMC) mS/cm	Corrosive to aluminum
LiClO ₄	106.4	>100	8.4	No
LiAsF ₆	195.9	>100	11.1	No
LiBF ₄	93.9	>100	4.9	No
LiPF ₆	151.9	80 in (EC/DMC)	10.7	No
LiTFSI	286.9	>100	9.0	Yes
LiBOB	193.9	>100	7.5	No
LiFAP	451.9	>100	8.2	No

1.2 Solid electrolyte interphase

The formation/existence of Solid Electrolyte Interphase (SEI) is a double-edged sword⁵³. On the one hand, the formation of SEI consumes lithium which causes an irreversible capacity fade and also increases the resistance against further lithium insertion. On the other hand, SEI works as a protecting layer which prevents the electrode from the continuous reaction with the electrolyte and thus enables the stability of the electrode. Thus, research on the composition and structure of SEI is necessary⁵⁴.

1.2.1 The formation of solid electrolyte interphase

As discussed in section 1.1.2, in order to get a high E_{battery} , electrodes should work in a wide potential window. If the redox potential of the electrodes used in a battery lies outside the electrochemical stability window of the electrolyte, the decomposition of electrolyte is unavoidable. As shown in Fig. 1.4, Goodenough and Kim schematically illustrate the condition of the decomposition of the electrolyte. If the highest occupied molecular orbital (HOMO) of the electrolyte is higher than the cathode Fermi energy (μ_c) or the lowest unoccupied molecular orbital (LUMO) of the electrolyte is lower than the Fermi energy of anode level (μ_A), the electrolyte can be oxidized or reduced, respectively¹¹. In fact, the decomposition of electrolyte is not only determined to its electronic structure, but also attributed to other factors such as the transport of ions. Thus, the electrochemical stability of electrolytes was corrected to the potential of electrolyte reduction at negative potentials, and of potential of solvent oxidation at positive potentials⁵⁵.

Furthermore, the solid products of the electrolyte decomposition will adhere on the surface of the electrodes and so prevent further decomposition of the electrolyte. In the above discussion, the electrolyte was considered as a complete system. In fact, the electrolyte contains various solvents, lithium salt and various additives (if necessary), therefore, we have to separately discuss components of the electrolyte when analyzing the process of SEI formation.

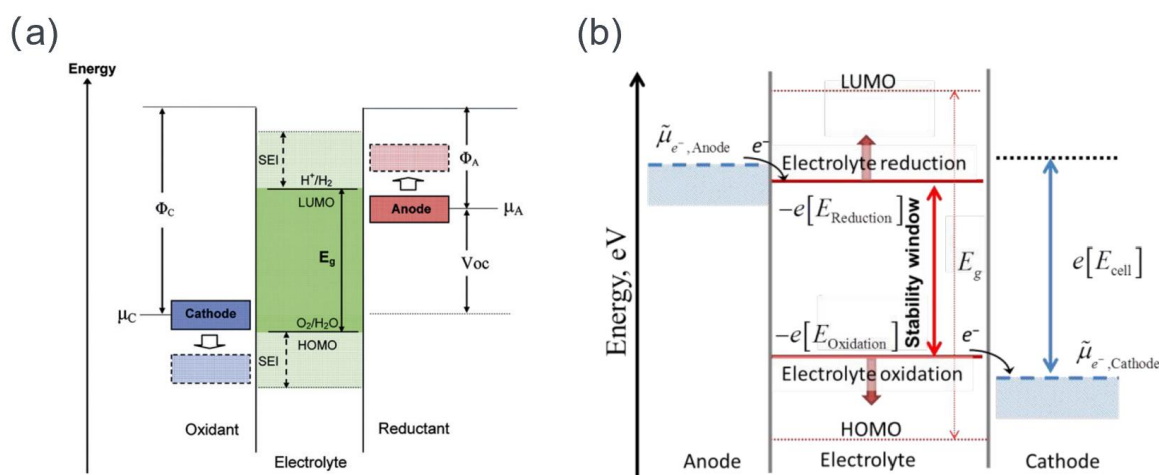


Figure 1.4: Schematic energy diagram of an aqueous electrolyte. (a) Φ_A and Φ_C are the work function of anode and cathode, respectively; E_g is the thermodynamic stability window of electrolyte; μ_A and μ_C are the redox potential of the anode and cathode, respectively. A $\mu_A > LUMO$ or $\mu_C < HOMO$ requires a kinetic stability by the formation of an SEI layer¹¹. (b) the electrochemical stability of electrolytes was corrected to the potential of electrolyte reduction at negative potentials, and of potential of solvent oxidation at positive potentials⁵⁵.

1.2.2 The model of the anode electrolyte interphase.

Attributed to the unique role of SEI for the electrochemical performance of the anode, in the last four decades, a significant progress in our understanding of the SEI has been obtained. Early in 1970, Dey et al. first proposed the passivation layer formed by the decomposition of propylene

carbonate on lithium metal. Subsequently in 1979, Peled et al. first introduced the concept of SEI⁵⁶. Shortly in 1983, he postulated that the SEI has a double layered structure with a compact layer on the side adjacent to the lithium metal anode, while a porous outer layer on the side toward to the electrolyte⁵⁷. In 1985, Nazri et al investigated the composition of SEI by in-situ X-ray diffraction (XRD), they identified that Li_2CO_3 is the main component of the inner SEI and the outer SEI mainly consists of polymers⁵⁸. Later in 1987, Aurbach et al. found that alkyl carbonate is main component of this outer layer by infrared (IR) and X-ray photoelectron spectroscopy (XPS)⁵⁹. At around 1997, Peled proposed a mosaic structure of the SEI and its equivalent circuit⁶⁰. In 1999, Aurbach et al. summarized many of the previous works and illustrated the forming process of SEI (multi-layered structure) starting from the initial decomposition of electrolyte⁶¹. In 2006, Edström et al showed a model of SEI on graphite anode cycled in the electrolyte (LiPF_6 in EC/DEC) for which Li_2O and LiF were detected by soft XPS, while the presence of Li_2CO_3 is a matter of debate⁶¹. In 2012, Siqi Shi et al. reported a two-layer/two-mechanism model having combined many characterizations and investigated the Li diffusion in two layers, respectively⁶². In 2017, Yi Cui et al. used cryo-TEM to propose two distinct nanostructures (mosaic and multilayer SEI) formed on Li metal surface⁶³. In 2020, Zhu et al described a-double-layer SEI with a clear model of electric double layer by using a real-time mass spectrometry⁶⁴. Very recently in 2022, Zewen Zhang et al, used cryo-TEM capturing the swelling of SEI in lithium metal batteries⁶⁵.

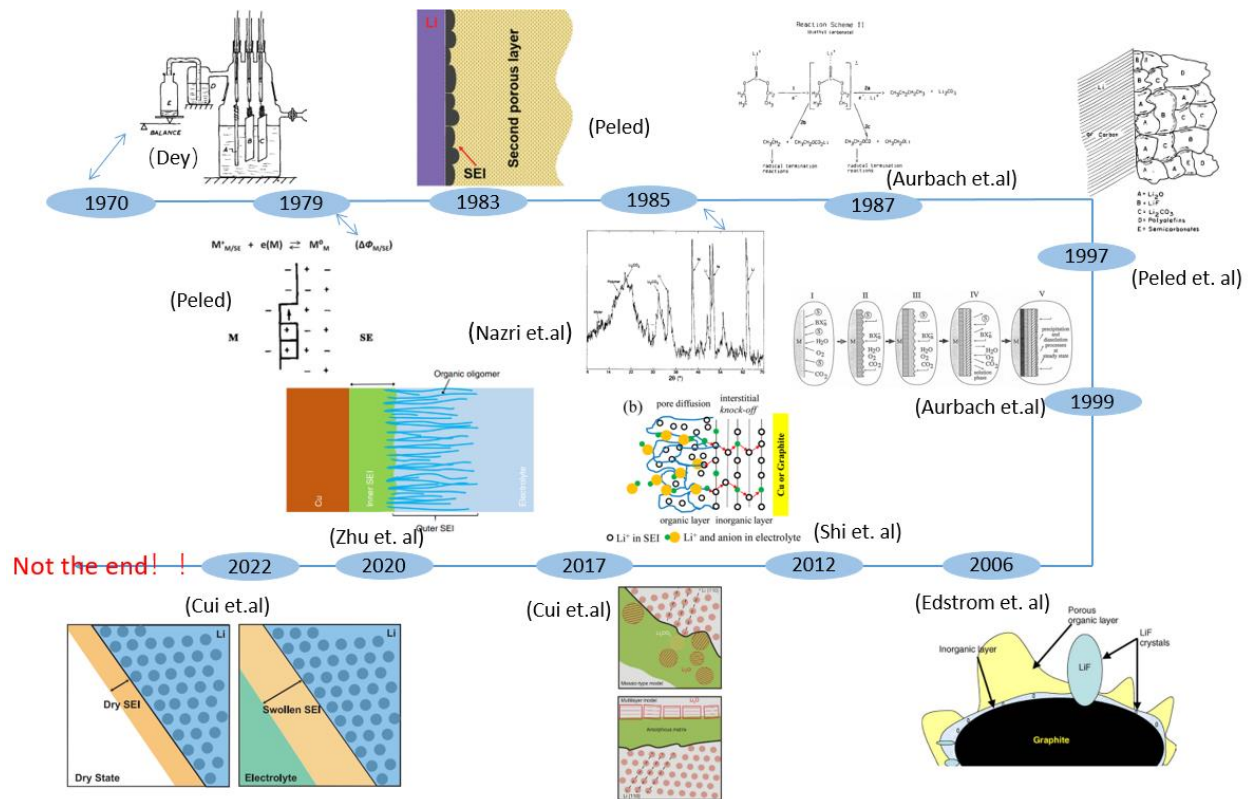


Figure 1.5: A brief history of SEI on anode.

In general, there is no consensus on which of the three models, mosaic structure, double-layer structure or multi-layer structure provides the better description of an SEI. All of these three models are frequently used in today's interfacial research. Moreover, it is worth noting that these three models postulate a similar general spatial structure that inorganic species are closer to the electrode than organic components.

1.2.3 Techniques for studying solid electrolyte interphases

Owing to the sensitivity of SEI, the sample should not be exposed to air during the characterization or transfer into the instruments. Otherwise, the results may be misleading. For example, some groups claimed that compounds such as Li_2CO_3 could originate from poor

environmental control during ex-situ analysis⁶⁶. Thus, the cell disassembling should be operated inside the glove box and transfer vessels are needed to protect original samples during the transfer.

Generally, electrochemical properties, chemical composition, phase structure and morphology of SEI can be characterized via various instruments. Fig. 1.6 shows an overview of the available techniques for the SEI characterization⁶⁷. Each method has its own unique advantage, thus, various techniques are applied sequentially and simultaneously to possibly achieve a complete characterization of the cycling behavior and SEI formation process on various time- and length-scales.

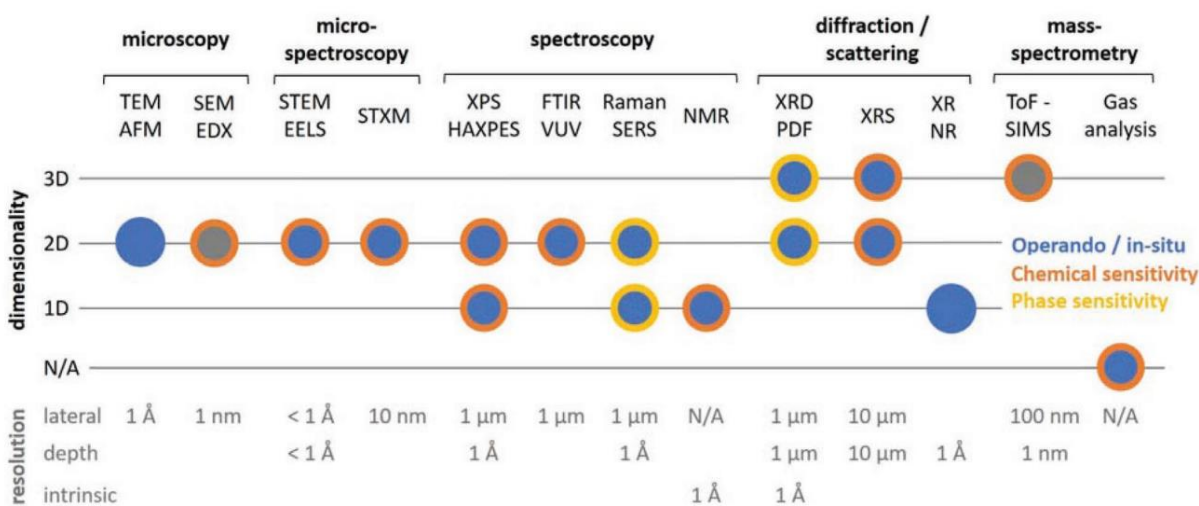


Figure 1.6: An overview of different characterization to study the SEI formation⁶⁷.

1.2.3.1 Characterization of phase structure

The structure of phase is generally investigated using some diffraction technique. With regard to damage to the sample, in-situ X-ray diffraction (XRD) allows the detection of dynamic changes in the phase structure of the sample. However, attributed to the extremely low thickness of SEI,

some details escape the resolution of XRD. Thus, synchrotron-based X-ray diffraction was proposed which enables more precise analysis of thin SEI, where Shadiké et al. used this method to prove the existence of LiH in SEI⁶⁸. Furthermore, the wave nature of energetic electrons enables them to diffract when experiencing a periodic crystal. Selected area electron diffraction (SAED) is an important part of transmission electron microscopy that (TEM) supports the simultaneously investigation of phase and morphology⁶⁹. Moreover, due to the neutron's interaction with the nucleus, neutron diffraction can detect the scattering/absorption contrasts for specific elements, crucially lithium and hydrogen, endowing with unique perspectives of structural information and phase composition^{70,71}. Except the crystalline, the amorphous phase can be tracked by X-ray absorption spectroscopy. Based on this technique, Toney et al. found that crystalline Ge lithates inhomogeneously, and eventually convert to amorphous Ge after delithiation⁷².

1.2.3.2 Morphology

The most useful techniques for characterizing the morphology of the electrode is the electron microscopy. Scanning electron microscopy is generally used to investigate the surface of the electrode, while TEM provides way more localized spatial information of the electrode and its surface. Furthermore, TEM can also be used to investigate the spatial variation of the chemical composition. However, some ultra-sensitive species decompose under the irradiation with the high energy electron beam, which makes the results unreliable. Recently, in-situ TEM and cryo-TEM were utilized to understand the working mechanism of the electrodes. For instance, the interfacial insertion of lithium ions into graphene layers was proved by in-situ TEM⁷³, while the effect of additive on the SEI formation was investigated by cryo-TEM⁷⁴. Furthermore, with the in-

situ cell, transmission X-ray microscopy (TXM) provide 3D microstructure of electrodes via reconstructing a series of 2D projections⁷⁵. Compared with electron microscopy, TXM has the advantage of being non-destructive to the sample and the possible combination with in-situ XRD. Moreover, Atomic Force Microscopy (AFM) has demonstrated the surface imaging by ‘feeling’ the surface with a mechanical probe. Due to negligible damage to the sample in non-contact mode, in-situ AFM can provide the dynamic evolution of surface topography of an electrode. For examples, in-situ atomic force microscopy was used to study the surface microstructure of a Sn electrode by Beaulieu et al., who have found that the pulverization of Sn, caused by inhomogeneous volume expansion, leads to a continuous consumption of the electrode and the electrolyte⁷⁶.

1.2.3.3 Characterization of chemical composition

Different species ascribe different chemical, electrochemical and mechanical properties. Thus, characterizing the chemical composition of the electrodes and the SEI is an effective method to evaluate the battery system. Most prominent, X-ray photoelectron spectroscopy (XPS) is the most common technique for identifying the composition of the electrode (ever of particular oxidation states). It detects the escape photoelectrons escaped from the sample being irradiated by X-rays in an ultra-high vacuum^{77,78}. A combination of soft and hard XPS offers great possibilities for chemical speciation with nm depth profiling capabilities⁷⁹ Furthermore, performing resonant XPS or increasing the kinetic energy of electrons with high energy photoemission (HAXPES) also helps to enhance bulk sensitivity and access interfacial chemistry in a non-destructive manner⁷⁹. In addition, nuclear magnetic resonance (NMR)⁸⁰, fourier-transform infrared spectroscopy (FTIR)⁸¹, raman and auger spectroscopies (AES)⁸² and secondary

ion mass spectrometry (SIMS)⁸³ also indirectly or directly identify the chemical composition of SEI.

Generally, due to the complexity of SEI, a single characterization technique is not enough and the combination of various methods provide a higher chance to precisely understand the SEI. One of the techniques which have not been mentioned yet, but is discussed subsequently, is quartz crystal microgravimetry. It has gained recent attention in the electrochemical community and is used extensively in this thesis.

1.3 Quartz crystal microbalance

1.3.1 Working principle

The basis of the quartz crystal microbalance is the inverse piezoelectric effect. AT cut quartz with a cutting angle of $35^{\circ}15'$ is used as a sensor for shear motion in thickness shear mode. As shown in Fig.1.7 (a) and (b), when two contacts are brought to the faces of the quartz plate, the electric field induces reorientation of the dipoles, resulting in an anisotropic lattice strain and shear deformation of the material. In quartz, this deformation is fully elastic. The opposite polarity produces an identical strain, but in the opposite direction. As shown in Fig. 1.7 (c), it follows that an alternating potential across the crystal causes a vibrational motion in the quartz crystal with amplitude parallel to the surface of the crystal. A standing wave condition can be established when the acoustic wavelength is equal to 2 times of the crystal thickness. Thus, we can get the relationship between frequency of the acoustic wave in the resonant condition.⁸⁴ As shown in Fig. 1.6 (d), if a layer is deposited on the surface of the quartz crystal, the acoustic wave will propagate through the deposited layer as well and shear stresses are continuous over the sensor-

film interface. The quartz surface should be at an antinode of the acoustic wave. In this case, the layers on quartz close to the surface influence the natural frequency only through their inertial mass instead of their elastic properties. If the film is thin, homogeneous and rigid, the acoustic properties of the foreign layer are identical to those of quartz, then the resonance frequency decreases linearly as a function of layer mass according to the well-known Sauerbrey equation⁸⁵.

$$\Delta m_Q = - \frac{\sqrt{\rho \cdot u}}{2n \cdot f^2} \cdot \Delta f = -\Delta f \cdot C_f^{-1} \quad 1.7$$

where ρ is the density of the quartz, u is the effective piezoelectrically stiffened shear modulus of quartz, n is the overtone order and f is the resonance frequency of the quartz, Δf is the frequency change in Hz and Δm_Q is the mass change from QCM. All geometry and material dependent parameter may be comprised in the sensitivity factor C_f , which mainly depends on the thickness of the given quartz crystal.

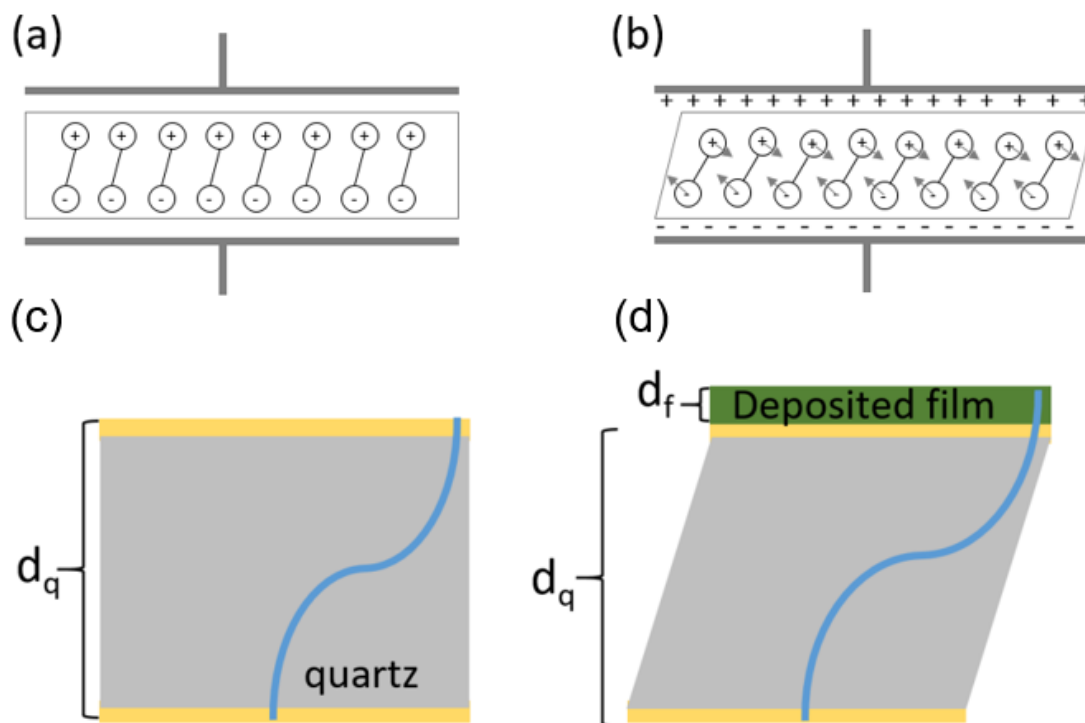


Figure 1.7: An external electrical field induces strain in an acentric AT-cut quartz single crystal (a) and (b). Resonance wavelength increase with layer deposition on the sensor surface (c) and (d).

1.3.2 Application of QCM for LIB research

QCM as an ultra-sensitive weight detector can measure the mass change on the electrode with sensitivity at the level of nano-grams. After combining with electrochemical test especially cycle voltammetry (CV), the loaded or uploaded species can be identified by the Mass per charge (further discussed in section 2.5.5). Furthermore, QCM can provide the accurate working potential window of each reactions allowing dynamic investigation on the working mechanisms of LIB. In view of processes that may cause mass change of the electrode during the cycling, QCM-

based measurements usually are used in the following aspects⁸⁶: (1) Lithium ion insertion/extraction behavior in the electrodes; (2) the formation/evolution of the solid electrolyte interphase (SEI); (3) the oxidization/ reduction of electrode. Based on this methods, the charge/discharge process on many kinds of electrodes, such as LiMn_2O_4 ⁸⁷, $\text{Li}_4\text{Ti}_5\text{O}_{12}$ ⁸⁸, Sn ^{89,90}, Si ⁹¹, have been successfully investigated. Following, three areas are introduced that researchers mostly concerned.

1.3.2.1 Gravimetry with other techniques

QCM exhibits irreplaceable advantages and can provide unique information for battery studies. Nevertheless, the premise of MPE- based interpretation is under the assumption that only one species forming and decomposing in a time interval. However, the surface of the electrode is not smooth, especially after SEI formation which brings different voltage drop at different positions. Normally, there must be multiple reactions occurring at a time. Therefore, the results for this time may not be ambiguously. Furthermore, there are some species having similar MPE but derived from completely different reactions such as the decomposition products of solvents ($\text{C}_4\text{H}_4\text{O}_6\text{Li}_2$: MPE = 81 g/mol from EC reduction, $\text{C}_2\text{H}_3\text{O}_3\text{Li}$: MPE = 82 g/mol from DMC reduction)⁹²

Therefore, complementary characterizations need to be introduced for accurate analysis. Meanwhile, they also bring other characterizations of electrode, such as the phase structure, morphology and mechanical properties. Although some of ex-situ characterizations can effectively prove the assumptions made from QCM results, there is no doubt that the contamination of the electrode and the change in the electrode environment reduce the reliability of these ex-situ results. Thus, some of in-situ and nondestructive electrodes techniques

were combined with QCM to provide comprehensive insights into the charge–discharge mechanism of battery, and the summarize were shown in Table 1.3^{92, 93, 94, 95, 96, 97}.

Table 1.3: summary of works reported by combining QCM and other in situ techniques

Combined technique	Electrode	Main conclusion	Reference
In-situ FTIR	Sn	The MPE shift by solvation/desolvation of Li ⁺	88
In-situ DEMS and AFM	Graphite	Redox mediator on discharge products	87
In-situ AFM	LiMn ₂ O ₄	Volume change of crystalline material	89
In-situ XRD	Graphite	Intercalation of solvated Na-ions	90
In-situ Raman	Li-O ₂	The effect of water and HF on discharge products	91
In-situ EIS	Graphite	The effect of VC and FEC on SEI formation	92

1.3.2.2 Gravimetry with dissipation

The limitation of the Sauerbrey equation make it only appropriate for rigid films in a non-viscous liquid. However, in LIB systems, the viscoelasticity of electrode especially after the SEI formation and the viscosity of electrolyte may dampen the oscillations of QCM sensor. In other words, an underestimate of the resonance frequency and the mass change is unavoidable during the QCM measurements. As shown in equation 1.8, the measured frequency change (Δf) is the sum of the the frequency change associated with the mass change (Δf_m) and the changes in viscoelastic properties of the liquid (Δf_L)

$$\Delta f = \Delta f_m + \Delta f_L \quad 1.8$$

In 1985, Kanazawa et al analyzed the frequency shift by the change in the density (ρ_L) and viscosity (η_L) of the liquid⁹⁸. As shown in equation 1.9:

$$\Delta f_L = -f_0^{3/2} \sqrt{\frac{\Delta(n_L \rho_L)}{\pi u_q \rho_q}} \quad 1.9$$

$$\Delta R = \sqrt{2\pi f_0 \Delta(\eta_L \rho_L)} \frac{A}{k^2} = -(\pi \sqrt{2u_q \rho_q} \frac{A}{k^2 f_0}) \Delta f_L \quad 1.10$$

Due to the difficulty in direct measuring the ρ_L and η_L of electrolyte, as shown in equation 1.10, Resistance (R) was introduced to estimate the $\eta_L \rho_L$, where k is the electromechanical factor. It can be seen that the Δf_L has a negative linear relationship with ΔR . However, attributed to the inhomogeneous concentration of the electrolyte near the electrode during the charge–discharge process, a semi-quantitative interpretation can be obtained by ΔR ⁸⁷.

Energy dissipation (D) was introduced to quantitatively analyze the viscoelasticity of the solid/liquid system. Specifically, sensor resonance dissipation is recorded by either measuring half the bandwidth of the resonance peak⁹⁹ (Γ) or by using the so-called ring-down technique¹⁰⁰.

On the one hand, the quartz crystal admittance (QCA) was firstly proposed in 2002 for the impedance analysis by measuring the Γ ¹⁰¹. Furthermore, penetration depth δ_n of shear wave emitted by an oscillating quartz crystal towards the viscous liquid was calculated via equation 1.11 and the relationship of δ_n and Γ is shown in equation 1.12⁹⁴.

$$\delta_n = \sqrt{\frac{\eta_L}{\pi n \rho_L f_0}} \quad 1.11$$

$$\frac{\Gamma}{n \rho_L f_0^2} = \frac{-\delta_n}{\sqrt{u_q \rho_q}} \quad 1.12$$

Both of these two equations can be used to evaluate the structure of electrode via viscoelastic property and morphology.

On the other hand, as shown in equation 1.13, the dissipation factor (D) was investigated by switching on and off the applied alternative voltage regularly to measure the energy loss from quartz sensor to liquid¹⁰².

$$D = \frac{E_{dissipated}}{2\pi E_{stored}} \quad 1.13$$

Where $E_{dissipated}$ is the energy dissipated during one period of oscillation and E_{stored} is the initial energy of the QCM sensor. Generally, a large D demonstrates the sample is soft and thick, while a small D implies that the sample is rigid and compact¹⁰³. Furthermore, the Voigt viscoelastic models were investigated by measuring the f and D at different overtones, which allow researcher to demonstrated the deviation of mass caused by its viscoelasticity. For example, Yang et. al, studied the mass and viscoelasticity of interfacial films on Sn anode. Combined the Sauerbrey and Voigt viscoelastic models, they found the SEI layer formed at FEC-based electrode has higher shear elastic modulus than that in pure electrolyte⁹⁰.

1.3.2.3 Studying the long-term SEI formation and cycling behavior on electrodes (anodes)

For rechargeable lithium ion batteries, attributed to the rapture of the structure of the electrode, the capacity of battery decreases with the cycle number. As a non-destructive-electrode technique, recently, the long-term SEI formation and cycling behavior of electrodes were investigated by our group. In view of the long cycle time (more than a week) or many cycle number (more than 100 cycles), Terwort et al. proposed a detailed time resolved in-situ mass spectrometry based on QCM that even enables in suitable cases the identification of reversibly or irreversibly processed species (at the example of V_2O_5)¹⁰⁴. With this technique, later the long-term cycling behavior of Si was studied by Kohler et al. Remarkably, they found that half of the

chemical storage in thin film Si electrodes is not due to lithiation but due to reversible adsorption of Li_2O to the SEI layer⁹¹.

1.4 Motivation

After more than 40 years of research, the fundamental understanding of the cycling behavior and SEI formation on various electrodes is still unclear, attributed to their complex formation/dissolution process, instability, environmental sensitivity and variability over time. This thesis presents a systematic research on the long-cycle behavior and SEI formation on anodes (group IV: Sn and Ge) by combining electrochemical Quartz Crystal Microbalance (QCM) and Cyclic Voltammetry (CV). This approach allows the direct simultaneous measurement of the in-situ mass change and charge transfer. Furthermore, the calculated mass per charge (MPE) provided the in-situ changes in chemical composition within a small time interval ($< 14\text{s}$). We combine three different characteristics including mass spectra, real-time MPE and average MPE, to study the overall process and various stage of the long-term SEI formation. Besides the irreversible SEI formation, the reversible redox shuttle was also quantitatively investigated based on the comparison of QCM and CV mass amplitude. Since the amount of formed Li_2O appeared to be dependent on the onset of the lithium insertion potential, the study brings in a new variable to control the amount of reversible Li_2O and better design new electrode materials.

2 Experimental methods and data analysis

This chapter describes the equipment used in this work and the corresponding working principle, including the equipment of sample preparation and characterization. Besides, because systematic analysis of data is the most important part of this work, data processing and the corresponding formulas are also derived in this chapter.

2.1 Thin film sample deposition

In this work, thin film anodes are deposited by ion-beam sputter deposition. Generally, ion-beam sputter is a typical physical vapor deposition (PVD) technique. In order to get a high purity thin film, the base pressure of the chamber was around 1×10^{-7} mbar. Activated Ar served as plasma, considering some samples need oxygen during sputtering, two kinds of gun including direct current (DC)⁸⁹ and radio frequency (RF)¹⁰⁵ were used and the corresponding schematics are shown in Fig. 2 - 1 (a) and 2 - 1(b), respectively.

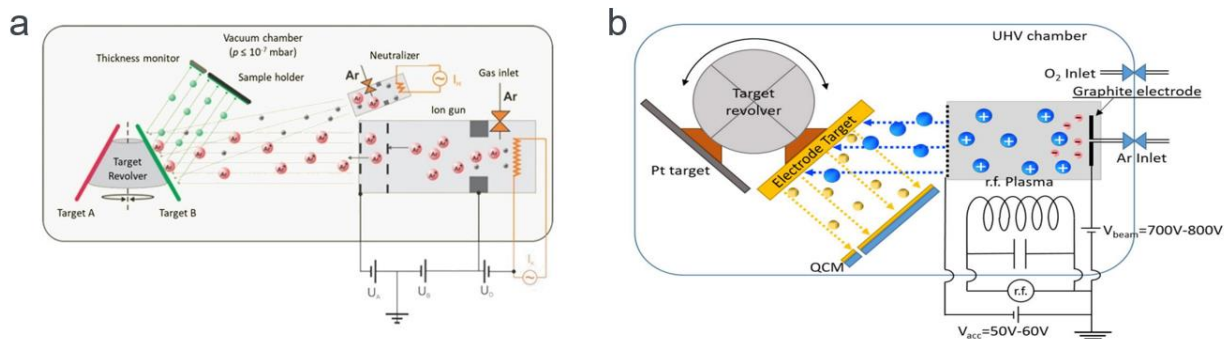


Figure 2.1: Schematics of (a) the DC ion beam sputtering and (b) the RF ion beam sputtering.

The electrodes which do not need oxygen during sputter were deposited by a custom-made DC ion-beam sputter system equipped with an Ion-Tech KF/F 40 Kaufman type ion source. As shown

in Fig. 2 - 1 (a), during the sputtering, the Ar gas was ionized by a cathode made of a 7 turns W-thoriumoxid filament. A discharge voltage is applied to both sides of the cathode, which can accelerate the electrodes towards a ring anode. Thus, electrons ionize the Ar atoms by penning ionization and a conductive plasma is formed. An acceleration system consisting of two isolated carbon grids is added to get the high energy plasma. Before bombarded against the target, the ions are neutralized by another W filament to prevent the charging of the target. By the energetic Ar hitting the target, the atoms of the target surface are evaporated and deposited on the substrate.

2.1.1 DC ion-beam sputter deposition

In this works, a beam voltage of 1 kV, a beam current of 21 mA and an acceleration voltage of 100 V have been used. During deposition, the growth rate is measured with a quartz crystal microbalance (SQM-160, Inficon) placed next to the substrate, calibrated by comparison with TEM cross section micrographs. Commercial Ti/Au-coated 5MHz quartz QCM sensors were used as the substrate. A sketch of the sample geometry is shown in Fig. 2.2 (a).

2.1.2 RF ion-beam sputter deposition

Since tungsten filament is easily oxidized, RF sputtering is often used for reactive sputtering with oxygen, since no filament is needed to ignite the plasma. Generally, the argon plasma is generated in a small ceramic cavity which is surround by an inductive coil. This coil is powered by an RF source operating at 13.56 Mhz and a power of 120 W and will ionize Ar atoms via atomic collision attributed to the high pressure by purging. Electronically, the setup can be considered as a strain factor, where the inductive coil act as the primary coil and the discharge plasma as a

secondary coil. Thus, under the high frequency of the RF source, the argon atoms in the ceramic cavity gets ionized. Moreover, a beam voltage of 900 V and an accelerate voltage of 65 V are used to accelerate and focus the plasma via the graphite grids. Due to insulating character of some targets, a beamswitch switches the polarity of beam and accelerator potential periodically to neutralize the target from time to time. Additionally, for the deposition of oxide, oxygen is inserted along with the argon plasma to provide the oxygen required by the thin film growth.

2.2 Structural characterization

2.2.1 Scanning electron microscopy (SEM)

The surface topography of electrode was characterized by SEM. The incoming electrons strike the atoms of the sample, and generate various signals containing information about the surface topography and composition of the sample are collected by respective detectors. In this work, a Thermo Fisher Scios Dual-Beam instrument was used at 5 kV 1.6 nA for the investigation of the surface.

2.2.2 Transmission electron microscopy (TEM)

In TEM, a high energy beam of electrons transit through the very thin samples. The interactions between the electrons and atoms of thin film can be used to investigated the structure and chemistry of sample. Generally, the sample is an ultrathin section less than 100 nm thick or a suspension on a grid. In this thesis, cross section samples were prepared via lamella lift-out in the FIB dual beam microscope (Thermo Fischer SCIOS). TEM characterization has been obtained with a Philips CM200-FEG instrument operated at 200 kV.

2.2.3 X-ray diffractometer (XRD)

XRD as a non-destructive analysis technique can characterize the crystal structure and the texture of a sample. The produced X-rays are scattered elastically by the periodic crystal lattice, which results in a specific diffractogram. The analysis of the reflections is based on Bragg's law:

$$2 \times d \times \sin(\theta) = n \times \lambda \quad 2.1$$

where n is the diffraction order, λ is the wavelength of incident X-ray, d is the distance between two adjacent parallel lattice planes and θ is the incident Bragg angle between the X-ray and the sample.

In this work, the electrodes (before and after cycling) were characterized by XRD using a Rigaku smartlab 3kW diffractometer with Cu-K α radiation, at a scan rate of 1°/min from 10° to 80°. Due to the sensitivity to air, an air tight cell was loaded inside the glove box and prevented the sample from contamination during the XRD measurement.

2.2.4 X-ray photoelectron spectroscopy (XPS)

The composition of the SEI layer was identified by XPS. The working principle of XPS is to analyze escaped photoelectrons from the sample when irradiated by X-rays in an ultra-high vacuum. Different species have different kinetic energy and number of escaping electrons.

$$E_{binding} = E_{photon} - (E_{kinetic} + \phi) \quad 2.2$$

where $E_{binding}$ is the binding energy, E_{photon} is the energy of the X-ray photons, $E_{kinetic}$ is the kinetic energy of the electron and ϕ is the work function of the instrument detector. Moreover, an Argon sputter ion gun was used to produce depth profiles of composition. Attributed to the

inhomogeneity of the SEI, the accurate sputter rate may vary considerably. The sputter rate 10 nm min^{-1} used in this work is estimated and provides only a rough depth scale. The XPS measurements were conducted with a spectrometer from Thermo Fischer Scientific Inc., equipped with an Al $K\alpha$ X-ray source emitting radiation with an energy of 1486.4 eV.

2.3 In-situ mass measurement during electrochemical processing

Electrochemical cycling of the electrode on the quartz crystals was carried out in a custom made cell with two electrodes. A lithium foil was used as combined counter and reference electrode. A sketch of the setup is shown in Fig. 2.2 (b). Besides, QCM and CV work independently, but correlated in time.

A mixture of 50 wt% ethylene carbonate (EC, alpha Aesar, 99%), 50 wt% dimethyl carbonate (DMC, sigma Aldrich, 99%), containing 1 mol L^{-1} lithium perchlorate (LiClO_4 , sigma Aldrich, 99.99%) was used as electrolyte. Cyclic voltammetry (CV) were performed using a BioLogic VSP-300 potentiostat controlling the relevant electric parameters. Simultaneously, a Maxtek RQCM was used to measure the resonance oscillation frequency of the AT-cut quartz crystals to determine the mass change during the lithiation and delithiation. To stabilize the equipment, a 24h OCV measurement was carried out before cycling. Both the installation and the measurement were done inside a glove box to prevent oxygen or water contamination (O_2 and H_2O content < 0.5 ppm).

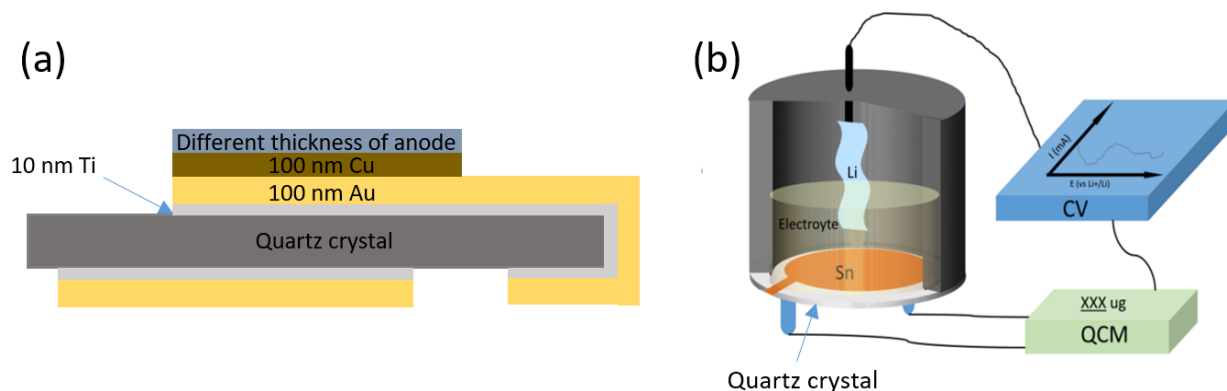


Figure 2.2: Scheme of (a) the working electrode and (b) of the setup for the CV-QCM measurement with the working electrode at the bottom.

2.4 Data analysis

The data analysis has been calculated by MATLAB and the corresponding code is shown in the appendix.

2.4.1 Capacity

As shown in equation 2.3, total charge was integrated as current over time, and normalized by the corresponding volume (or mass) to get the respective specific capacity.

$$C = \frac{Q}{V} = \frac{1}{V} \int I dt \quad 2.3$$

2.4.2 Mass from QCM

The mass change (Δm_Q) during the lithiation and delithiation cycles was calculated from the change of resonance frequency according to the Sauerbrey equation⁸⁵ (equation 2.4).

$$\Delta m_Q = -\frac{\sqrt{\rho \cdot u}}{2n \cdot f^2} \cdot \Delta f = -\Delta f \cdot C_f^{-1} \quad 2.4$$

where ρ is the density of the quartz, u is the effective piezoelectrically stiffened shear modulus of quartz, n is the overtone order and f is the initial resonance frequency of the quartz, Δf is the change of this resonance frequency in Hz. All geometry and material dependent parameter may be comprised in the sensitivity factor C_f , which mainly depends on the thickness of a given quartz crystal. In this work, a 5 MHz Quartz crystal of 330 μm thickness with the corresponding sensitivity factor of $1.767 \cdot 10^{-8}$ Hz/ng/cm² has been used. Moreover, the detection limit of the QCM controller (Maxtek RQCM) is 0.1 Hz, which corresponds to a mass change sensitivity of 1.8 ng/cm².

2.4.3 Mass per charge

In order to further analyze the reactions during the cycling, QCM mass and CV charge data are combined to get the real time mass per elementary charge (MPE) (equation 4)¹⁰⁶, which could be used to conclude for the main species processed during the cycling.

$$\text{MPE} = \frac{\Delta M}{\Delta Q/e} = \frac{-e \cdot \Delta m_Q}{I \Delta t} = F \cdot \frac{\Delta m_Q}{\Delta Q} \quad 2.5$$

In which Δm denotes the QCM mass change during a short time interval Δt . The time interval of our instrumentation is 13 s, we will plot the data as “real time” MPE. However, in certain potential ranges, the respective curves may become quite noisy because of tiny currents. In this case, suitable larger time intervals can reduce the noise. Or, as also suggested in literature⁹², the average MPE may be calculated by the slope of the Mass change versus charge curve. Both calculation concepts have their own advantages. In real time MPE calculated for short periods, we can distinguish details that are otherwise overlooked. Also by choosing a reasonable time

interval we can compile a kind of mass spectrum (see below). But when these data become too noisy, evaluation of the slope is required to derive meaningful information.

2.4.4 Mass from CV and the amount of Li₂O

As a comparison measure, the expected mass change was also calculated from the CV data (Δm_{cv}) by equation 2.6, under the assumption that only lithiation and delithiation does change the sample mass and charge. m_{Li} is the mass of a lithium atom, Q is the measured charge, e is the elementary charge, M_{Li} is the molar mass of Li and F represents Faraday's constant.

$$\Delta m_{cv} = m_{Li} \cdot \frac{Q}{e} = M_{Li} \cdot \frac{\Delta Q}{F} \quad 2.6$$

However, in fact, based on previous works⁹¹, both Li and Li₂O can work as reversible species. The fraction of a reversible Li₂O to that of total reversible processed mass and the absolute mass change of reversible Li₂O (Δm_{Li_2O}) were calculated as follows.

Firstly, the weighted average mass ($m_{average}$) and the weighted average mass per charge ($MPE_{average}$) of mixture (Li and Li₂O) are calculated according equation 2.7.

$$\Delta m_Q = m_{average} \cdot \frac{\Delta Q}{e} = MPE_{average} \cdot \frac{\Delta m_{cv}}{MPE_{Li}} \quad 2.7$$

Then, mass proportion of Li₂O (A) and (Δm_{Li_2O}) are calculated by equation 2.8 and 2.9

$$MPE_{average} = A \cdot MPE_{Li_2O} + (1 - A)MPE_{Li} \quad 2.8$$

$$\Delta m_{Li_2O} = \frac{14.9A}{8A+6.9} \cdot \Delta m_Q \quad 2.9$$

where, MPE_{Li_2O} is the MPE value of Li₂O (14.9 g/mol).

2.4.5 Time-resolved mass spectra

In order to intuitively identify each processed species and their relative amounts, mass spectra are derived based on many MPE values¹⁰⁴. To be more specific, the MPE values calculated from equation 2.5 for many time intervals were assorted into a histogram with a class width of $1 \text{ g}\cdot\text{mol}^{-1}$, where the x -axis is the MPE, while the y -axis is the corresponding abundance of the selected MPE.

3 In situ characterization of the SEI formation on Sn anode by using a quartz crystal microbalance

Tin (Sn) has received particular attention as a high-capacity anode of which the theoretical capacity (994 mAh g^{-1}) is much larger than that of graphite (372 mAh g^{-1}). But, the formation of the $\text{Li}_{4.4}\text{Sn}$ intermetallic phase causes 257 % volume expansion, which leads to pronounced stress and cracking of Sn. As a result, delamination and pulverization of Sn provokes the loss of contact and finally leads to a severe capacity fade^{22,107}.

Numerous studies have characterized the SEI formation and Li storage mechanism of Sn. In-situ AFM was used by Beaulieu et al to study the surface topography of Sn anodes during cycling⁷⁶. The inhomogeneous volume expansion of Sn induces fragmentation which further leads the failure of Sn. Depth profiling XPS was performed to study the composition of the Sn anode by Xu et al⁸³. They concluded that Sn is oxidized and participates in the formation of SEI. Furthermore, the SEI on different single crystal Sn electrodes were investigated by Qiao et al. They stated that the SEI on Sn (100) mainly consists of porous Li_2CO_3 , while the SEI formed on Sn (001) consisted of LiF and organic species¹⁰⁸. However, in view of the cracking and delamination of parts of the Sn, the SEI formation on Sn must be a continuous process. As far as we know, no data focusing on the long-term cycling behavior and the growth of SEI on Sn are known.

In this chapter, as shown in Fig.2.2, QCM and CV were combined to study the SEI formation process on Sn thin film anodes under a relatively long-term cycling. For the investigation of the long-term cycling, the most challenges are the preparation of electrode with sufficient performance and the analysis of huge data. Here, we combine three different characteristics

including mass spectra, real-time MPE and average MPE, for the overall and segmented study of various stage during the long-term SEI formation.

3.1 Microstructure of as-deposited Sn thin film

Before starting the electrochemical and in-situ mass measurements, the microstructure of deposited Sn films of 100 nm thickness was characterized. As shown in Fig. 3.1 (a), the SEM images of as deposited thin film demonstrate significant roughness which was further proved by the bright field TEM cross section (Fig. 3.1 (b)). The observed island growth of Sn is probably due to very low melting temperature of Sn ($T_m=231.9\text{ }^\circ\text{C}$) and has been reported by others, too. Moreover, due to the low re-crystallization temperature of Sn, as shown in Fig 3.1 (c), the XRD curve demonstrate that the as-deposited Sn thin film is crystalline instead of the typical amorphous film of Si and Ge, when deposited at room temperature¹⁰⁹.

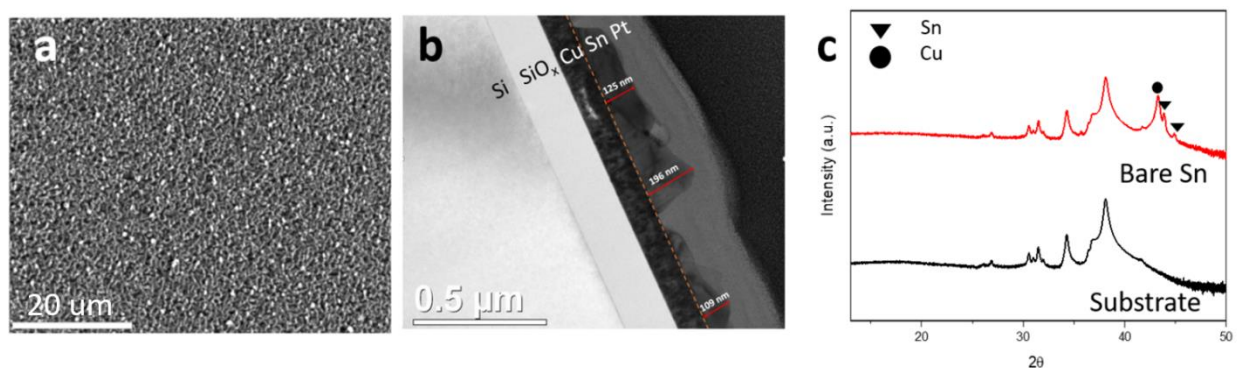


Figure 3.1: The (a) SEM surface image, (b) TEM cross section micrograph and (c) XRD pattern of as-deposited 100 nm Sn.

3.2 Electrochemical performance of Sn anode

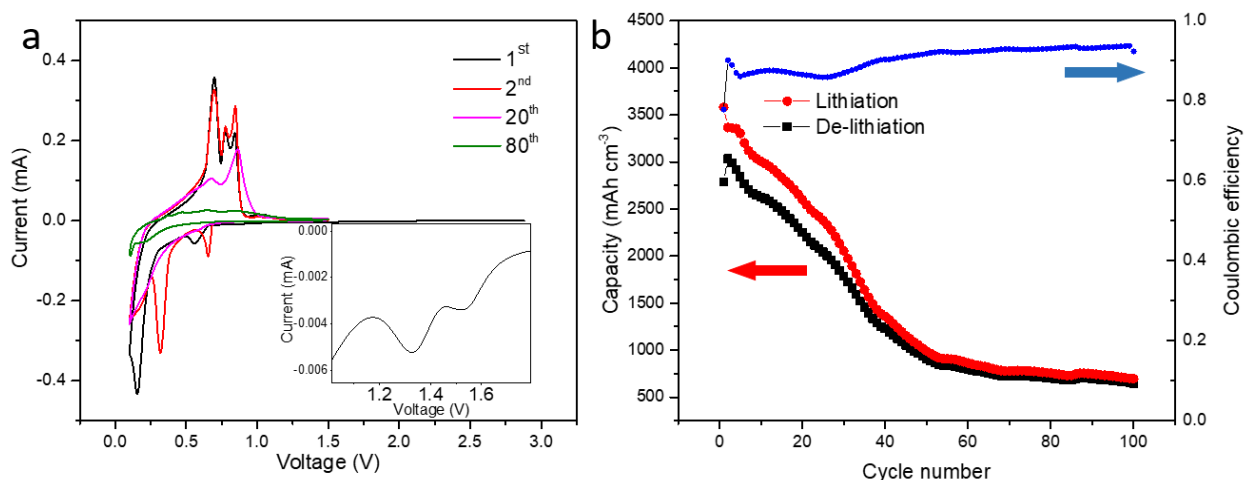


Figure 3.2: (a) CV curves of different cycles and (b) electrochemical capacity of a 100 nm Sn electrode at a scan rate of 0.5 mV/s in a potential window of 0.1-1.5V.

As shown in the CV curve in Fig. 3.2 (a), a 100 nm Sn anode was cycled in the potential window between 0.1-1.5 V, obtained at a scan rate of 0.5 mV/s. Negative and positive currents represent the charging and discharging, respectively. Specifically, the 1st, 2nd, 30th and 80th cycles were chosen representing the different SEI formation stages, which are further discussed below. In detail, for the first cycle, as shown inset of Fig. 3.2 (a), there is a broad discharging peak that ranges from 1.2-1.67 V, which is assigned to the electrolyte decomposition and SEI formation¹¹⁰. Furthermore, the negative peaks around 0.6 V, 0.15 V and the positive peaks at 0.7 V, 0.78 V, 0.86V corresponded to the lithiation and delithiation, respectively, which are in good agreement with other literature¹¹¹. Besides, with the cycle number increase, the intensity and position of peaks change systematically, and we will discuss what happens in the following part.

As shown in section 2.4.1, based on the CV data, the electrochemical capacity of the Sn anode was calculated by integrating the current over time. As shown in Fig. 3.2 (b), the maximum lithiation and delithiation capacities were 3580 mAh cm^{-3} and 3034 mAh cm^{-3} , respectively. The lower capacity in comparison to the theoretical one (7316 mAh cm^{-3}), is mainly attributed to the relatively high lower boundary (0.1 V) of the potential window. The investigation of Sn cycled at different potential window will be discussed in chapter 4. Interestingly, the capacity decreases continuously until around the 60th cycle and then remains at around 680 mAh cm^{-3} . This capacity fading could be attributed to the continuous formation of SEI layer, therefore, the long-term cycling behavior and SEI formation on Sn should be investigated.

3.3 The SEI formation at a 100 nm Sn anode

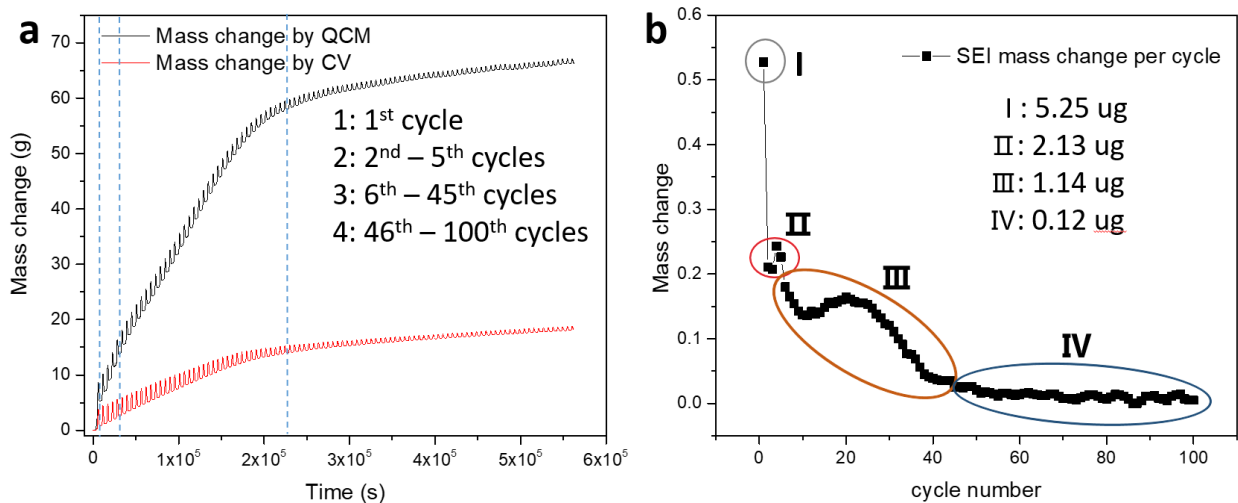


Figure 3.3: (a) Mass change during CV measured by QCM (black) and calculated from CV (red). (b) shows the irreversible mass change (SEI mass change) per cycle (stage I: 1st cycle, stage II: 2nd-5th cycles, stage III: 6th-45th cycles) and stage IV: 46th- 100th cycles).

In order to investigate the failure process of Sn anode, the mass change by QCM and CV (see chapter 2.4.2 and 2.4.3) are compared in Fig. 3.3 (a). The trend line of mass change indicates an

irreversible mass deposition which can be attributed to the SEI formation, while the periodic oscillation of mass change represents the reversible lithiation and delithiation. On the one hand, the loaded irreversible mass, after 100 cycles, Δm_Q and Δm_{cv} were 66.1 μg and 18.1 μg , respectively. The much larger total Δm_Q in comparison to Δm_{cv} indicates that heavier species than Li are irreversibly deposited on the Sn anode during the cycling. On the other hand of the reversible amplitudes, the oscillations of Δm_Q and Δm_{cv} decrease with the cycle number increase which demonstrates the capacity fade, which is in good agreement to the CV capacity (shown in Fig.3.2 (b)). The differences between the oscillation amplitudes of Δm_Q and Δm_{cv} will be discussed in the following sections.

$$\text{Thickness} = \frac{\Delta m_Q}{D_{SEI} \cdot 0.4075 \text{ cm}^2} \quad 3.1$$

Where D_{SEI} represents the density of SEI, 0.4075 is the surface area of working electrode (Sn).

As shown in equation 3.1, the thickness of the SEI can be estimated from the irreversible Δm_Q with reasonable assumptions on the density. As far as we know, the SEI of the Sn anode mainly consists of Li_2CO_3 (2.11 g/cm^3), LiCl (2.07 g/cm^3), LiOH (2.54 g/cm^3) and Li_2O (2.01 g/cm^3)^{90, 91}. Here, assuming equal proportion of each component, the average density 2.18 g/cm^3 is reasonable. Surprisingly, the calculated SEI thickness is 744 nm which is much thicker than Sn thickness (100 nm). As reported in previous work, the SEI thickness on Si anode has been thinner than 60 nm. To our surprise, Sn has more than 10 times thicker SEI than the quite similar anode material Si.

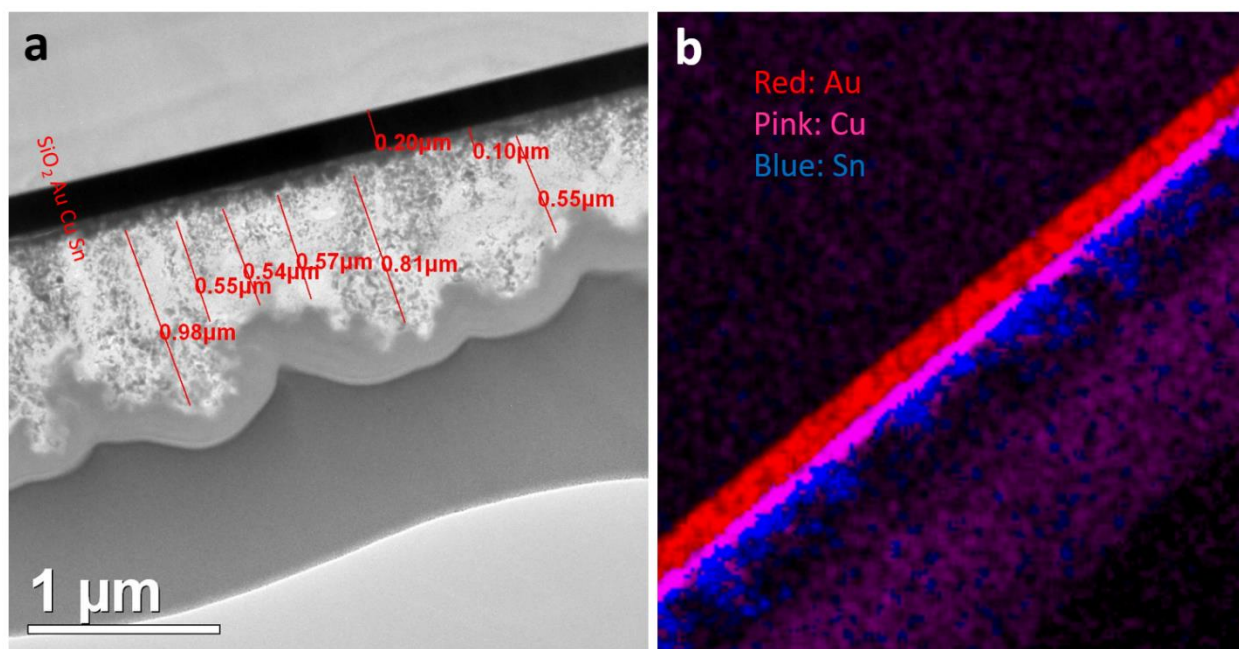


Figure 3.4: (a) TEM micrograph of 100 nm Sn after cycling, labeled with the thickness of SEI layer and (b) the corresponding EDX mapping of the TEM micrograph (Au (red), Cu (Pink) and Sn (Blue)).

In order to prove this remarkable conclusion, TEM lamella of this sample were prepared. As seen in the cross section micrograph (Fig. 3.4 (a)) and the corresponding chemical mapping (Fig. 3.4 (b)), the layer structure of the sample can be completely identified: quartz, Au, Cu, Sn, SEI and Pt (two Pt layers serve as the additional protection deposited during lamella lift-out). The thickness of the SEI layer varies considerably, on average 675 nm are determined. In view of the fluctuating thickness in the micrograph and the rough estimate of density, 10.2% deviation between both methods (QCM and TEM) are in well acceptable range, which confirms that the QCM can be used as a reliable in-situ monitor for the thickness of SEI. It cannot be ignored that, as shown in Fig. 3.4 (b), the signal of Sn (blue) was not only found close to the surface of Cu (current collector), but also distributes throughout the SEI. Thus, Sn probably participates in the formation of SEI which may be the reason why the SEI of Sn is much thicker than that of Si.

In view of the complexity of SEI formation on Sn, the SEI forming rate (irreversible mass change per cycle) was calculated by subtracting the initial mass (measured by QCM) from the final mass of each charging cycle. As shown in Fig. 3.3 (b), with the increase of cycle number, the SEI mass change per cycle shows a downward trend. However, there are two intermediate peaks probably due to the fact that the formation of SEI is dominated by different reactions. Therefore, the overall process was divided into four stages for further interpretation. Specifically, the first stage(I) is the first cycle and represents the fastest growth of 5.247 ug/cycle. Following, the stage II ranges from the 2nd to about the 5th cycle with an average SEI growth of 2.13 ug/cycle. Then stage III, from 6th to 45th cycle exhibit forming rates varying from 2.13 ug per cycle to 1.14 ug per cycle. Finally, the stage IV (from 46th to 100th) shows a quasi-stable SEI with only minor remaining forming rate (0.12 ug/cycle).

3.4 A top-down (from overall to detail) analysis strategy.

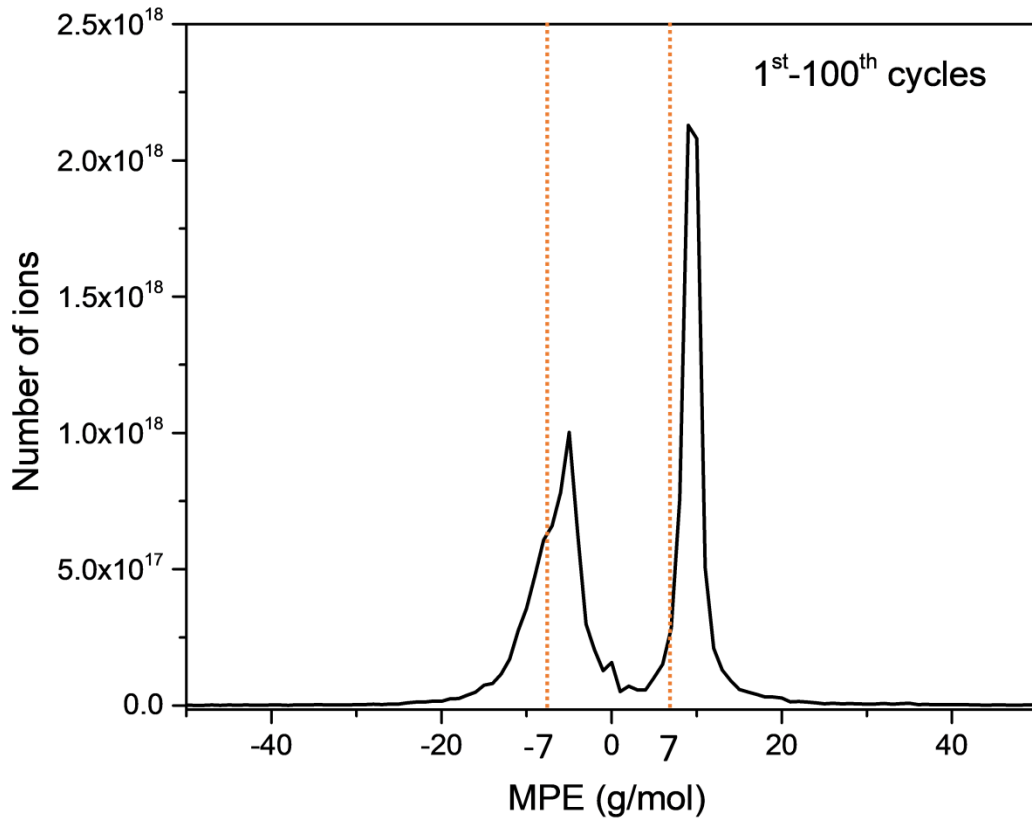


Figure 3.5: The over-all QCM mass spectrum.

The mass spectrum of all 100 cycles was calculated (see chapter 2.4.5) for figuring out the possible composition of the SEI layer. As shown in Fig. 3. 5.there are two peaks located around -7 and +7 g/mol respectively. The positive and negative values distinguish the charging and discharging process (the positive values represents charging, while negative values means discharging). Theoretically, as shown in equation 3.2 and 3.3, the MPE of lithium insertion and extraction are +7 g/mol and -7 g/mol, respectively. However, the calculated value of lithiation and delithion shift significantly apart from the theoretical values. As shown in chapter 1.3.2.2,

the viscoelasticity of SEI could make the Δm_Q overestimated. However, as shown in the work of Yang et al., during the delithiation, the Voigt mass which already adds the effect of damping is very similar with the Sauerbrey mass used in this study since the damping is hardly affected by the delithiation⁹⁰. Thus, the observed shift should be attributed to other reactions occurring during the cycling. As shown in equation 2.5, the MPE is determined by both the mass change and the processed charge. For the calculation of MPE, all the species are considered to be formed by a single electron transfer. In the following analysis process, the mass change is the main factor which causes the peak shifts.

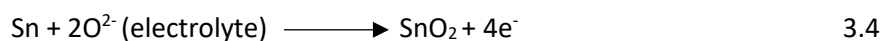
Remarkably, the shifts of both peaks are different. On the one hand for lithiation, the peak shifts to a larger value representing that heavier species are deposited during lithiation beside the expected Li ions. As reported in previous work on Si⁹¹, there two separate peaks clearly point at Li and Li₂O in the over-all MPE spectrum. Only if these heavier species form in different potential range than lithiation, the spectrum would reflect separated peaks. In the case of Sn, a single but shifted peak demonstrates that the formation of heavier compounds and Li insertion must be simultaneous. Taking into account the diversity of SEI without knowledge of their respective contribution, these heavier species cannot be identified. We will discuss this aspect later when discussing different stages of SEI formation. On the other hand for delithiation, a shift to absolutely smaller values means lighter species are desorbed during delithiation. However, it is unreliable that H⁺ exists in the electrolyte, otherwise the electrolyte would be not stable. Apart of hydrogen, we could not image a species of which the relative molecular mass per elementary charge is lighter than 7 g/mol.

Considering the previous conclusion that Sn participates in the formation of SEI, the shift might be attributed to the consumption of Sn. Inspired by studies of SnO_2 ,^{29,30} Sn may become oxidized at the end of the delithiation stage. If the required oxygen element stems from the electrolyte (as shown in equation 3.4), the mass change would increase during the delithiation.

Lithiation



Delithiation



The working principle of QCM only record the mass loaded or uploaded on the sensor while Sn permanently remains on the sensor. Thus, the MPE value of SnO_2 formed by equation 3.3 is + 8 g/mol (i.e. $2 \cdot (+16)/4$, where 2 is the number of oxygen atoms, 16 is the mass of one oxygen atom and 4 is the number of elementary charges required to neutralize the two oxygen ions, in eq. 3.3) Consequently, the calculated MPE value of delithiation should stem from -7 g/mol to +8 g/mol. If the contribution of the oxidation is small, we can expect only a slight peak shift from -7 g/mol to slightly less negative values. The XPS and XRD characterization will be presented later for proving the oxidation of Sn.

As discussed above, the SEI formation process can be divided into four stages. In order to figure out what occurred in each stage, the mass spectra of the four stages were plotted and shown in Fig. 3. 6 (a) - Fig. 3. 9 (a), respectively, since peaks of compounds with low amount are easily ignored in the main spectra. Four representative cycles (1st, 2nd, 20th and 80th) were selected, and the corresponding CV curves are presented in Fig. 3. 6 (b) - Fig. 3. 9 (b), respectively. Their MPE

presented by the two methods outlined in Sect. 2.4.4, real time MPE (Fig. 3.6 (c) - Fig. 3.9 (c)) and integral MPE Fig. 3.6 (d) - Fig. 3.9 (d), respectively.

Stage I: As shown in Fig. 3.6 (a), in the lithiation step (positive values): The highest peak at 10 g/mol must represent the lithiation (7 g/mol) as its shift agree to that of Fig.3.5. To possible explain the other peaks at high values, the chemical composition and its corresponding MPE value for possible species in LiClO₄/EC + DMC electrolyte were collected and shown in Table 3.1. There is a broad peak spreading from 14 g/mol to 20 g/mol which probably attributes to a mixture of inorganic species like Li₂O (14.9 g/mol), LiOH (23.9 g/mol), and Li₂CO₃ (36.9 g/mol). The amount of these inorganic species is less than that of Li. As shown in Fig. 3.6 (c) and 3.6 (d), the charging started at the OCV (2.9V). The large noise at the begin of charging is attributed to the tiny currents. Although little reaction occurs at this stage, the integral MPE clearly indicates a mass around 40 g/mol being deposited. Following, at a potential around 1.8 V, the MPE value increases from 40 g/mol up to 80 g/mol, and then rapidly decreases to below 20 g/mol (orange) at the potential of 0.8 V. As reported before, the SEI may consist of two parts, organic and inorganic parts and the organic part typically forms before the inorganic part. In view that the lithiation potential of Sn is out of the electrochemical stability window of the solvent (EC and DMC), as shown in Table 3.1, the large MPEs (from 40 – 80 g/mol) probably correspond to a varying mixture of the organic compounds: such as CH₃OLi (38 g/mol), CH₂OCO₂Li (81 g/mol), and C₂H₃O₃Li (82 g/mol)⁹². Then, with the decrease in voltage (more negative), the smaller MPE (compared to those of organic compounds), obviously represent the inorganic part of the SEI like: Li₂O (14.9 g/mol), LiOH (23.9 g/mol), and Li₂CO₃ (36.9 g/mol). As shown in Fig. 3.6 (c), there are two observed peaks at 4750s and 5200s in the real time MPE curve, which clearly demonstrates that different reactions

dominate at different voltages. But from the QCM data, it is impossible to distinguish the proportion of various uncertain species. What we can safely deduce is that more than one species is formed in this range and different species are partly formed at different potential windows. The XPS will be used to identify the composition of inorganic SEI in following section. Finally, the MPE decreases to around 9 g/mol (green line) which obviously represents the lithiation of Sn. As discussed above, the bigger MPE value than that of lithium (7 g/mol) must be due to overlay with some side reaction involving a heavier molecule. Finally, at the end of lithiation, the slight increase of MPE may be ascribed to the cracking caused by volume expansion which indicates a consequent reformation of the SEI.

In the delithiation step (negative values), as shown in Fig. 3.6 (a), there are two peaks, one peak is clear centered at the expected -7 g/mol, while another small peak locates at - 10 g/mol. Furthermore, as shown in Fig. 3.6 (c) and (d), at the beginning (below 0.92 V), a bigger MPE value (10 g/mol) indicates some heavier species are decomposed (maybe reversible forming and decomposing) at this step. After 0.92 V, MPE quickly decrease to 7.3 which is very close to the MPE of delithiation (7 g/mol).

Table 3.1: Chemical composition and corresponding MPE values for expect species in the $\text{LiClO}_4/\text{EC} + \text{DMC}$ electrolyte.

Deposited species	MPE (g/mol)
Li	6.9
Li ₂ O	14.9
LiOH	23.9
Li ₂ CO ₃	36.9
CH ₃ OLi	38
(CH ₂ OCO ₂ Li) ₂	81
CH ₂ OCO ₂ Li	82

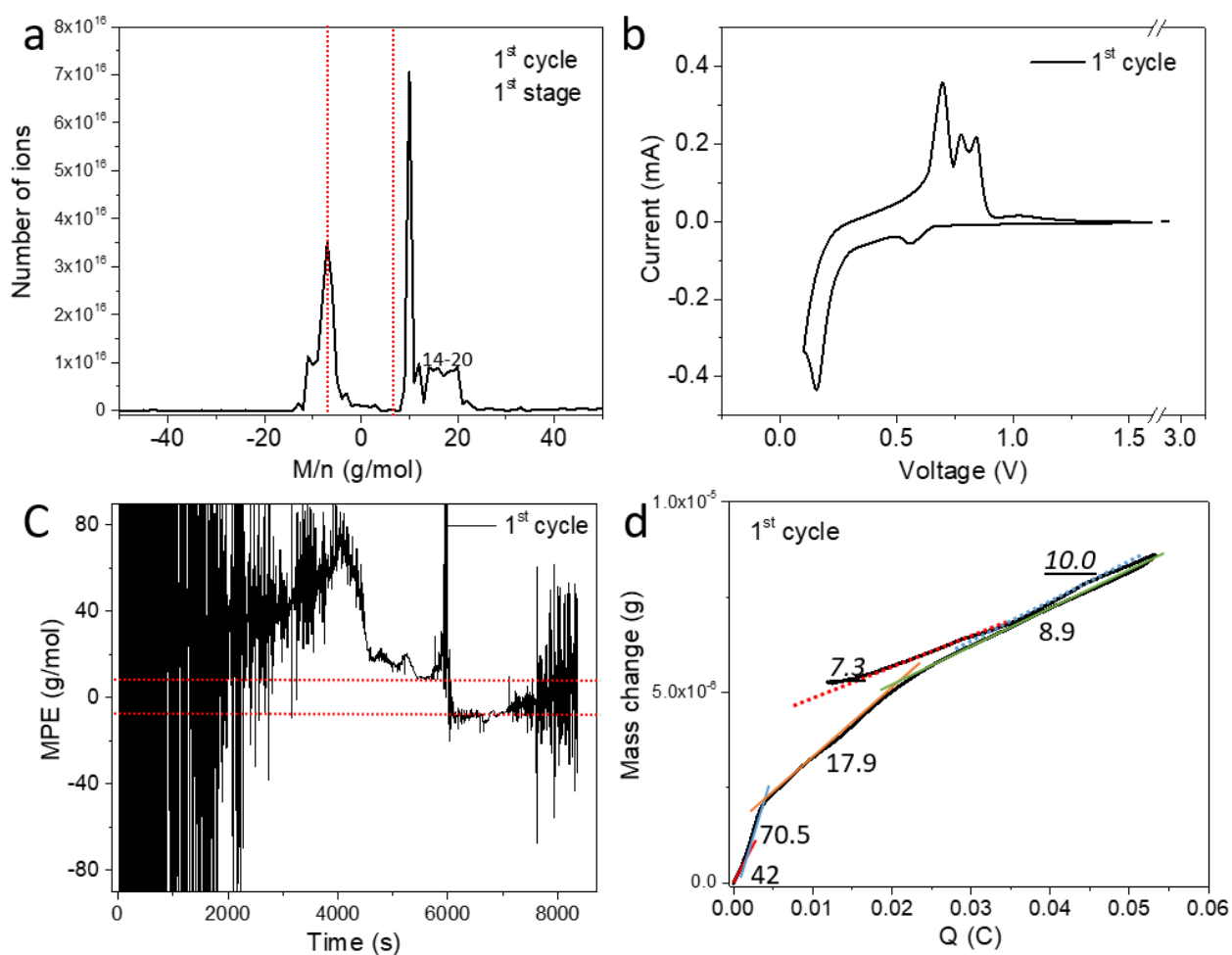


Figure 3.6: (a) The mass spectra of first stage (1st cycle), (b) CV curve, (c) real MPE curve and (d) average MPE curve of 1st cycle

Stage II: Fig. 3.7 (a) shows the mass spectrum of the 2rd to 5th cycle. On the one hand for the lithiation half cycle: Compared with that of in the first stage, the broad peak (14 – 20 g/mol) which is replaced by a small peak located at 13 g/mol in between the values of 7 g/mol (Li) and 14.9 g/mol (Li₂O). As shown in Fig. 3.7 (c) and (d), in the potential range of 0.31-0.28 V, the MPE is 14.7 g/mol (solid blue), close to the expected value of Li₂O. With further cycling, however, this peak decreases and finally disappeared until the end of stage II (5th cycle). It is generally expected that the SEI should be formed before the lithiation of anode¹¹². We will discuss the role of this irreversible Li₂O in chapter 4.

On the other hand, for the delithiation: As shown in Fig. 3.7 (a), similar to that of the over-all mass spectrum (Fig. 3.5), a slight shift of the delithiation peak to 6 g/mol indicates that additional oxidization of Sn starts at this stage. More details are revealed in the real-time and integrated MPE (Fig. 3.7 (c) and (d)). Clearly, the delithiation step can be subdivided into two steps. The MPE of the first step is bigger than 7 g/mol, while above 0.7 V, the MPE decreases to 6.2 g/mol, which demonstrates that the oxidization of Sn tends to occur at the end of the delithiation.

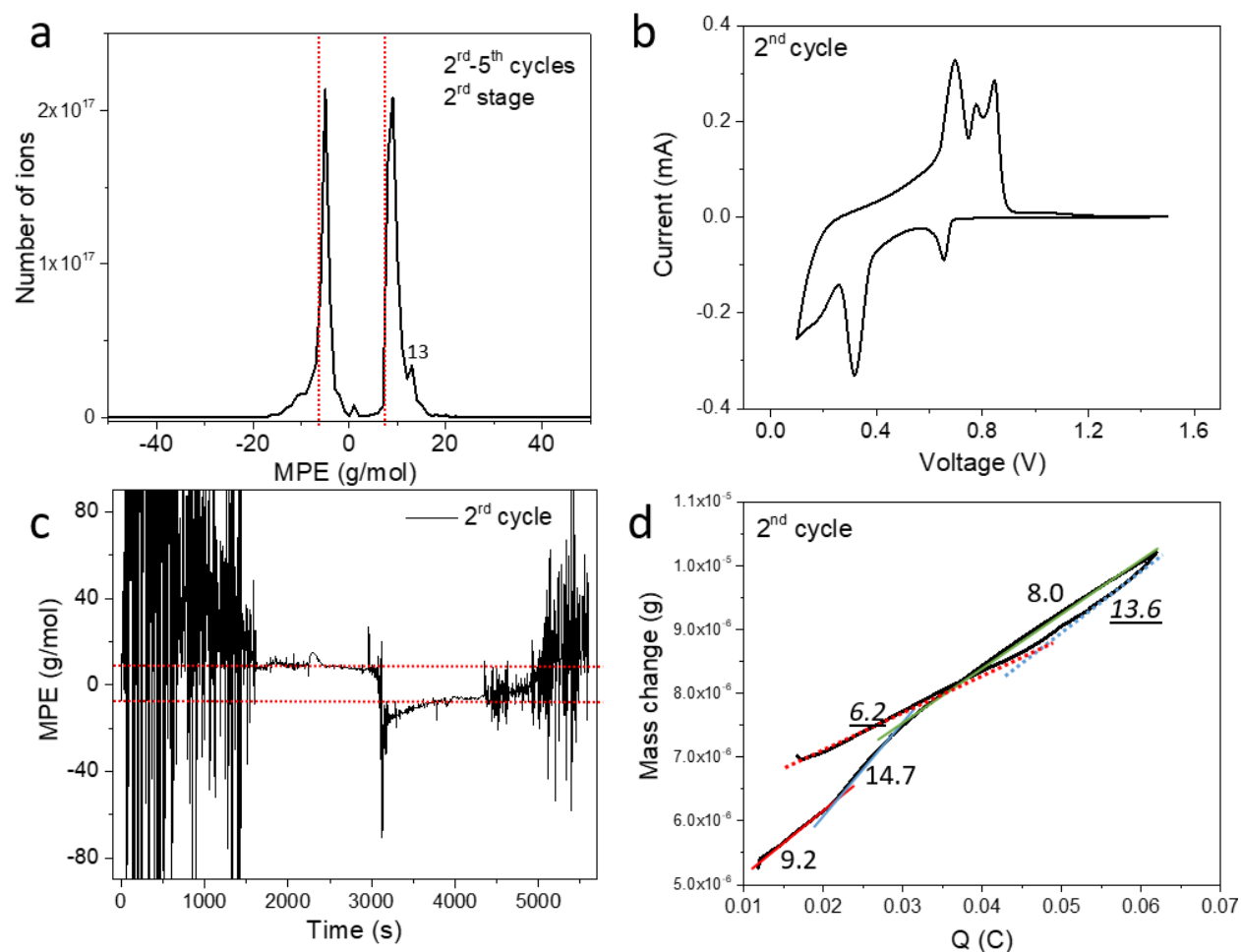


Figure 3.7: (a) The mass spectra of second stage (2nd – 5th cycles), (b) CV curve, (c) real time MPE curve and (d) integrated MPE curve of 2nd cycle

Stage III: Then, Fig. 3.8 (a) presents the mass spectra of the third stage (from 6th to 45th cycles). Similar to the over-all mass spectrum, the center of the lithiation peak locates at around 10 g/mol without extra peak. The delithiation peak still shifts to smaller values. Furthermore, as shown in Fig. 3.8 (c) and (d). Similar to second stage, the MPE value of 5.3 g/mol (red dot line) appear that Sn is oxidized after delithiation.

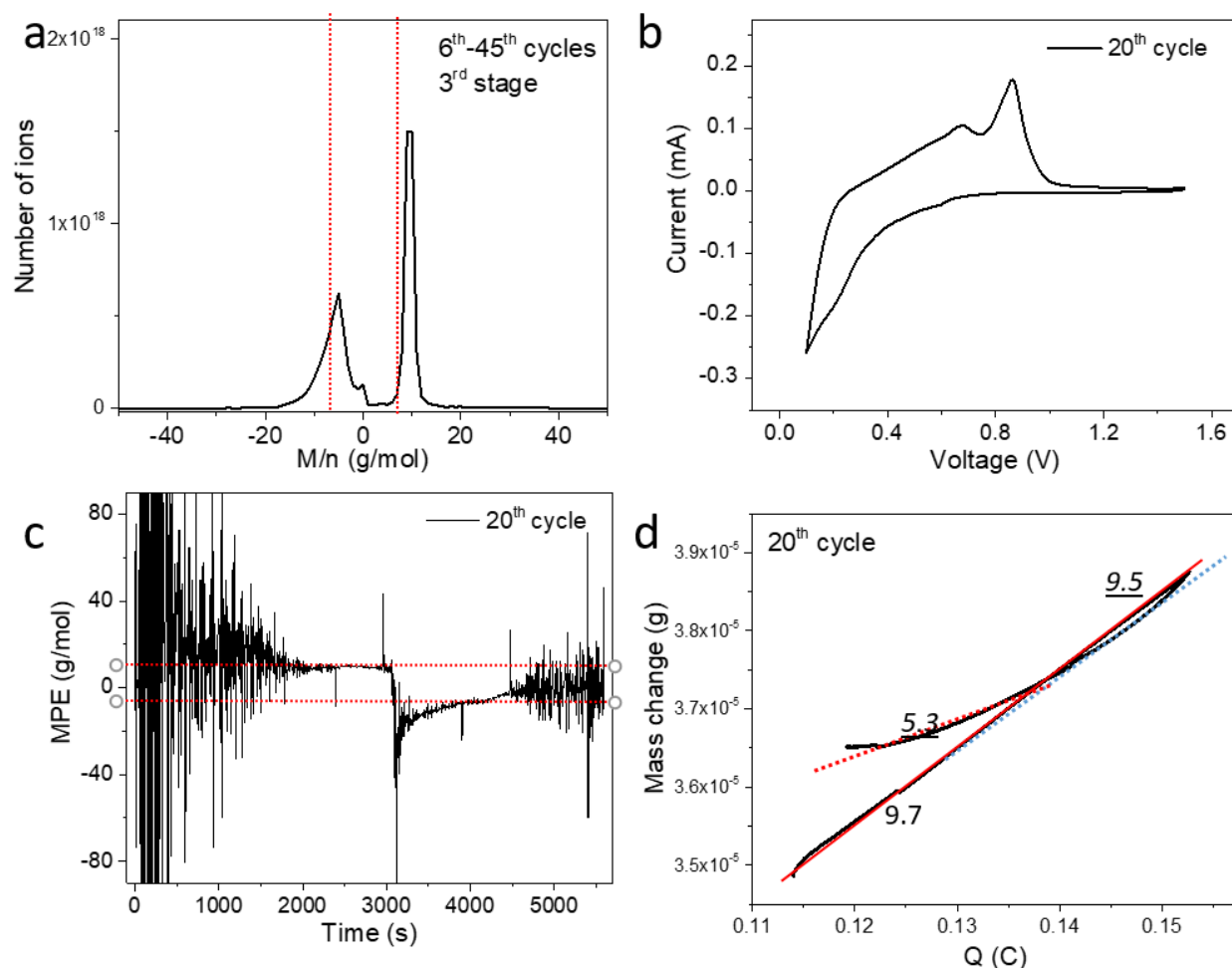


Figure 3.8: (a) The mass spectrum of third stage (6th – 45th cycles), (b) CV curve, (c) real time MPE curve and (d) integrated MPE curve of 20th cycle

Stage IV: Finally, Fig 3.9 (a) presents the mass spectra of stage IV (46th – 100th cycles). The lithiation peak is similar to that in the over-all mass spectrum (Fig. 3.5). However, the delithiation peak shifts to a bigger value (8 g/mol) than the expected MPE of lithiation (7 g/mol). In addition, as shown in Fig. 3.9 (c) and (d), the MPE of the second steps of delithiation is 7 g/mol, which clearly indicates a fact there is no Sn oxidation anymore in stage IV.

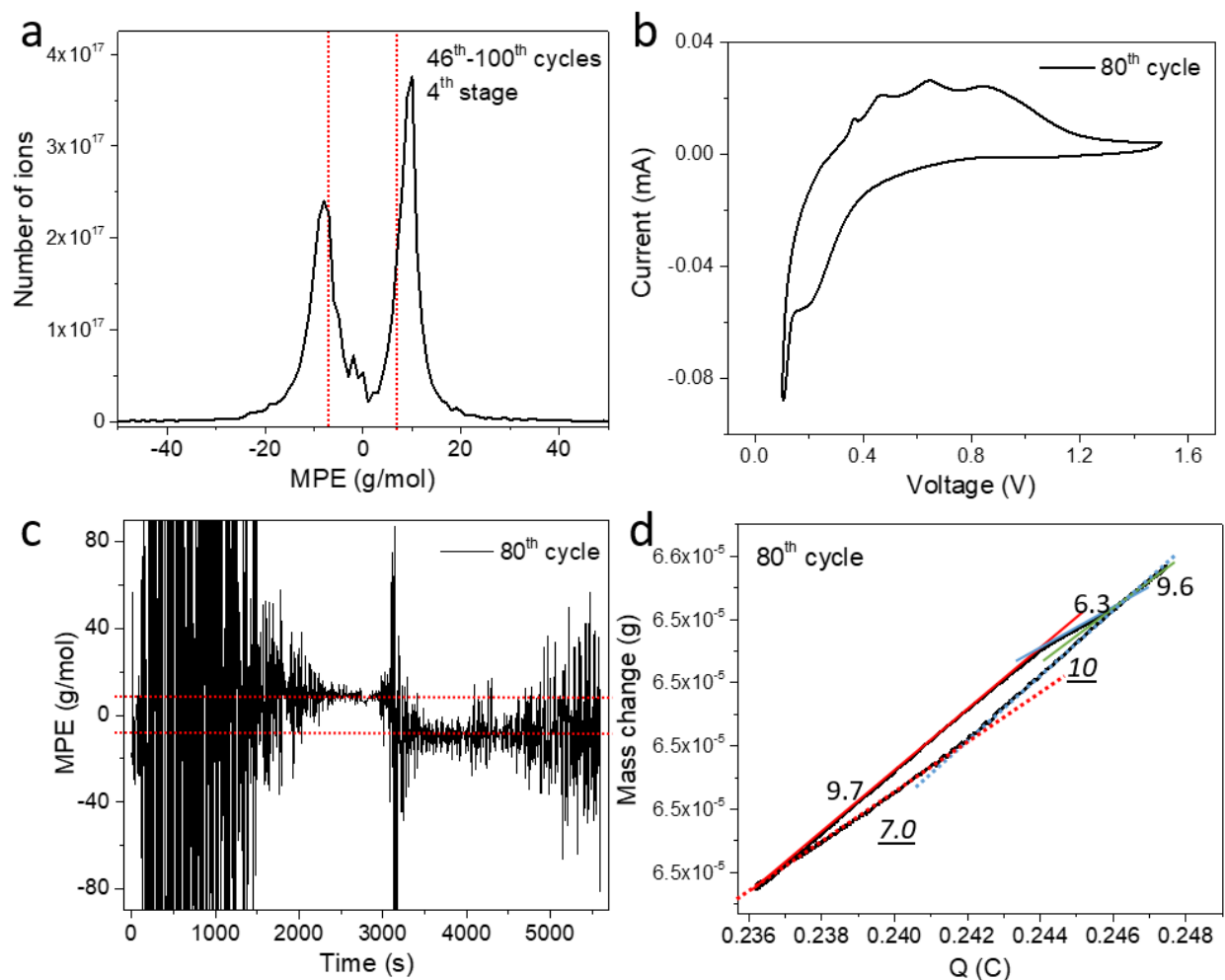


Figure 3.9: (a) The mass spectrum of fourth stage (46th – 100th cycles), (b) CV curve, (c) real time MPE curve and (d) integrated MPE curve of 80th cycle.

From the analysis of the MPE in these four stages, there is obviously a general phenomenon that we cannot ignore. As shown in Fig 3.6 (c) – Fig. 3.9(c), the delithiation steps are always subdivided into two parts, where the MPE value of the first step is bigger than that of the second step. As discussed in Fig. 3.3, Stage IV is a stable, the larger MPE in the first step of delithiation cannot be attributed to the break off of the parts of the electrode. Otherwise, there should be abrupt irregular variation of MPE. Thus, this large desorbed mass must be attributed to the decomposition of some heavier species. In view that the SEI change per cycle is quite small,

consequently, there should be another heavier species form and decompose reversibly. Inspired by previous work of Si, this heavier species might be identified as Li_2O . But, different to the case of Si, there is no separate mass peak of Li_2O . But peak shifts can be naturally attributed to multiple reactions happening simultaneously. To quantitatively investigate the possible amount of reversible Li_2O , the mass change for every lithiation and delithiation half cycle by QCM and CV were calculated, independently. As shown in Fig. 3.10 (a) and (b), in lithiation, QCM mass is systematically bigger than CV mass which is probably attributed to the heavier absorbed species. On the contrary, in delithiation, at the beginning, the QCM mass is smaller than CV mass which is due to the oxidization of Sn (see equation 3.4). But, after the stabilization of the electrode (stage IV), the QCM mass becomes larger than CV mass which clearly points that there are other heavier species reversibly cycling (see Fig. 3. 10 (a)). As shown in Fig. 3.10 (c), in stage IV, the amplitude of the reversible mass oscillations by QCM is constantly 1.25 times that by CV mass. As shown in chapter 2.4.3, assuming this heavier species is Li_2O , the contribution of this oxide to the reversible Li storage amounts to 23 %.

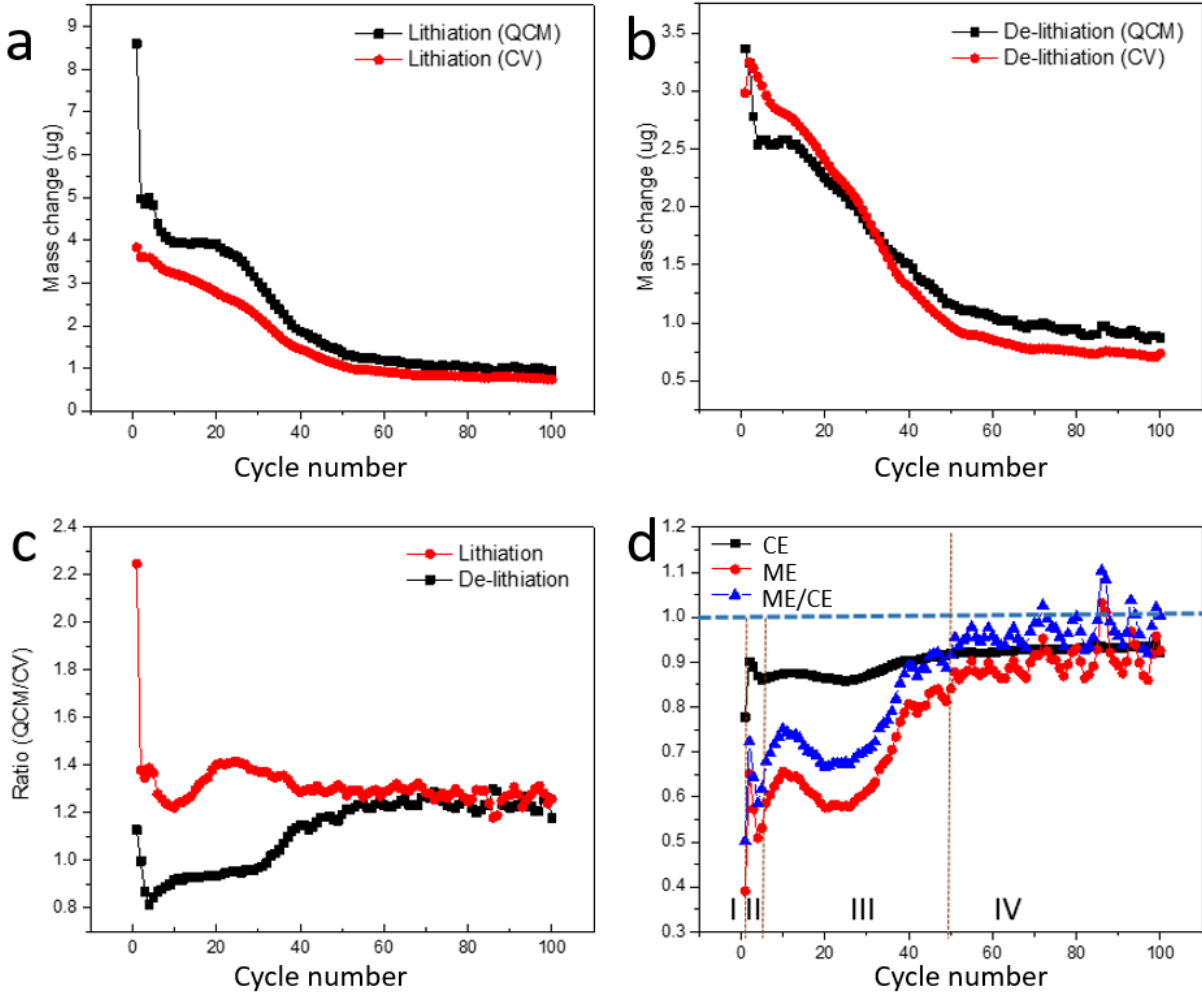


Figure 3.10: The mass change for every half cycle calculated by QCM and CV for (a) the lithiation half cycle and (b) the delithiation half cycle. (c) The ratio between QCM mass change and CV mass change for every half cycle and (d) The Coulombic Efficiency (CE), the Mass Efficiency (ME) and the ratio of ME to CE

Next, it is also insightful comparing the coulombic efficiency (CE) with the QCM mass efficiency (ME), shown in equation 3.5 and 3.6, respectively.

$$CE = \frac{\Delta Q_{\text{discharge}}}{\Delta Q_{\text{charge}}} \quad 3.5$$

$$ME = \frac{\Delta m_{\text{discharge}}}{\Delta m_{\text{charge}}} \quad 3.6$$

Since CE and ME are linked via the MPE, both cannot be independent. Averaging the MPE over the respective half cycles, we can quantitatively formulate:

$$ME = \frac{\overline{MPE}_{\text{discharge}} \cdot \frac{\Delta Q_{\text{discharge}}}{e}}{\overline{MPE}_{\text{charge}} \cdot \frac{\Delta Q_{\text{charge}}}{e}} = \frac{\overline{MPE}_{\text{discharge}}}{\overline{MPE}_{\text{charge}}} \cdot CE$$

$$\frac{ME}{CE} = \frac{\overline{MPE}_{\text{discharge}}}{\overline{MPE}_{\text{charge}}} \quad 3.7$$

Thus, as shown in equation 3.6, the ratio of ME and CE is related to the processed species contributing to MPE which may differ between charging and discharging. Indeed, as shown in Fig. 3.10 (d), the ME/CE (blue triangles) differs significantly from one in the first three stages (I II and III). Specifically, in stage I, the low ME is attributed to the heavy SEI irreversible formed in the first charging halfcycle. In stage II, the irreversible Li_2O increase the $\overline{MPE}_{\text{charge}}$, while the oxidization of Sn decreases $\overline{MPE}_{\text{discharge}}$. In stage III, although the Li_2O is considered reversibly cycling on the surface of Sn, the irreversible oxidization of Sn remains and decrease $\overline{MPE}_{\text{discharge}}$. Finally, in stage IV, most of Li and Li_2O is reversibly cycle. Thus the ME is close to one.

Finally, it is worth to mention that especially in stage IV, the MPE does well match the ideal value of delithiation (7 g/mol), which strongly confirms that the QCM data is reliable, although, also in stage IV, the SEI is the thickest compared with other stages. Thus, the viscosity of SEI do not affect the MPE value of delithiation significantly, which further proves that the shift in the delithiation peak (in stage II and III) represents the oxidization of Sn.

3.5 Characterization of the electrode before and after cycling

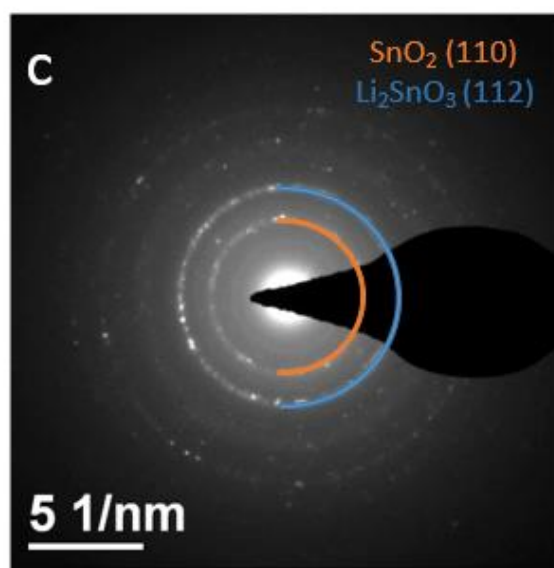
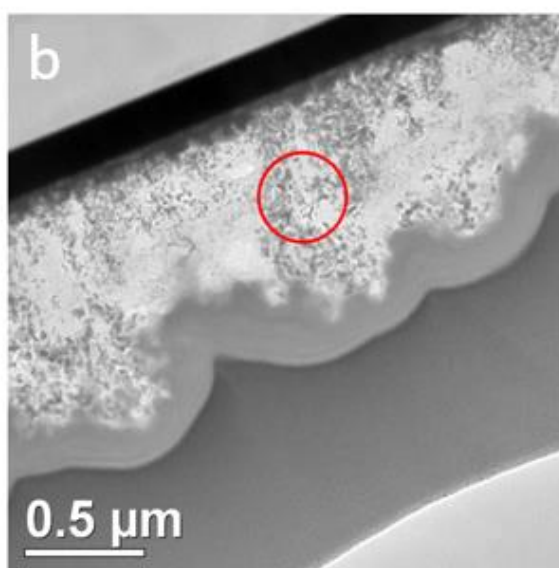
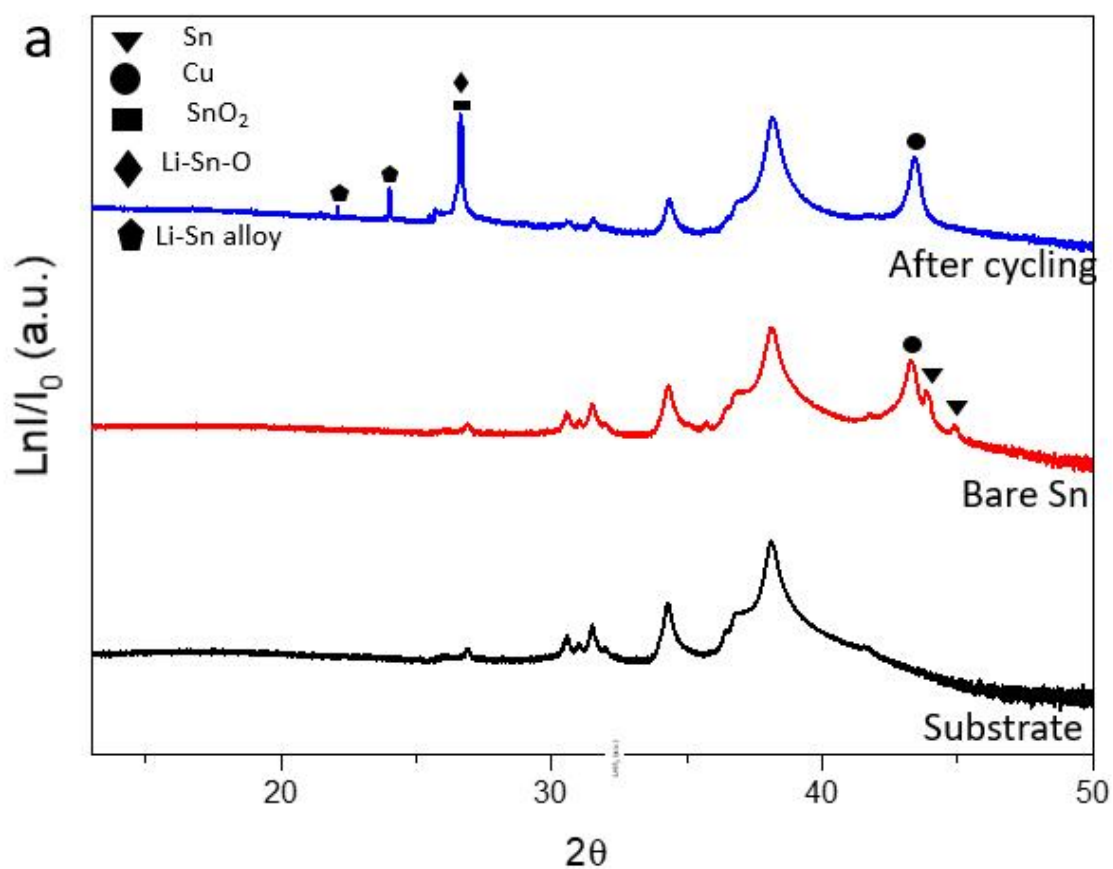


Figure 3.11: (a) XRD pattern of substrate (logarithmic intensity axis), as-deposited Sn on substrate (quartz, Ti and Au) and the electrode after cycling. (b) TEM micrograph of 100 nm Sn after cycling and (c) The diffraction pattern corresponding to the red cycle in the TEM micrograph.

In order to further characterize the formed SEI layer and to prove the conclusions from QCM-CV measurement, XRD, TEM diffraction pattern and XPS were performed. As shown in Fig. 3.11 (a), after long cycling (100 cycles), there is no signal of pure Sn anymore, and only the signal of Cu can be found. As mentioned above (Fig 3.2), any existing pure Sn at room temperature should be in crystalline structure. The disappearance of the Sn peaks indicates that Sn is mostly consumed. Besides, also some new peaks have appeared. A strong signal at 26.6° could correspond to the existence of SnO_2 (100) or Li_2SnO_3 (112), which was further proved by the diffraction pattern of electron microscopy shown in Fig. 3.11 (c) ¹¹³. So, both diffractograms of TEM and XRD strongly provide additional evidence that the oxidization of Sn assumed above is reliable. Finally small peaks at around 22° and 24° indicate a remaining Li-Sn alloy attributed to incomplete delithiation.

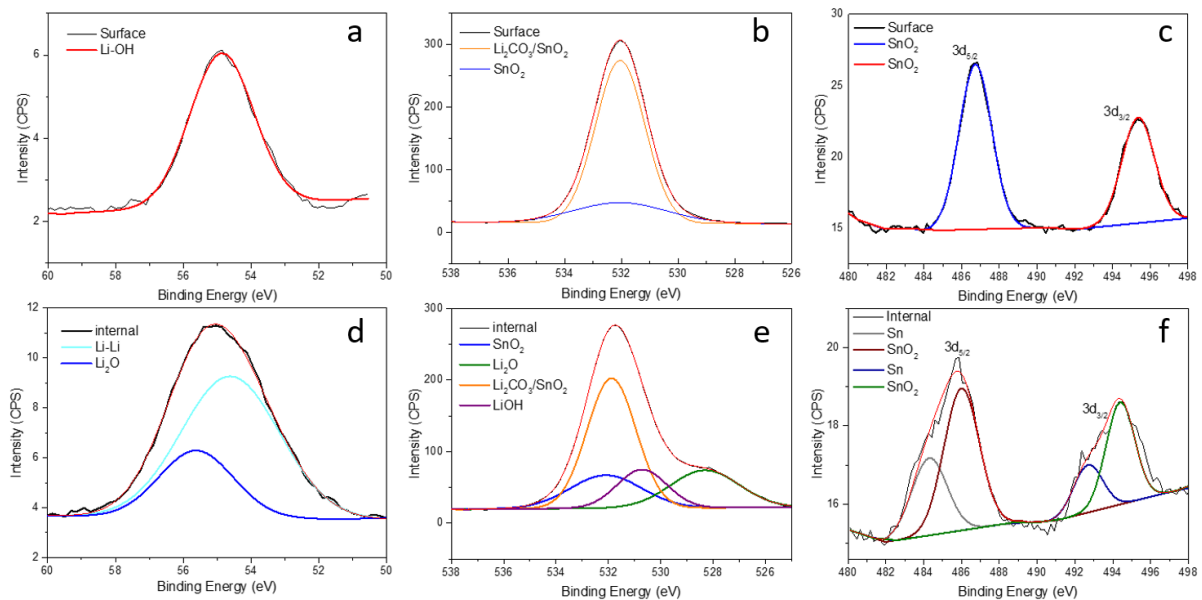


Figure 3.12: XPS data of surface (top (a), (b) and (c)) and volume of the SEI (bottom (d), (e) and (f)). (a) and (d) show the binding energy around the lithium 1s peak; (b) and (e) the binding energy around oxygen 1s peak; (c) and (f) the binding energy close to tin 3d peak.

To further prove the existence of SnO₂ and identify the composition of SEI, XPS measurements of surface and volume of the SEI were performed. As shown in Fig 3.12. (a) and (d), the surface signal of Li 1s peak prove the existence of LiOH and Li₂CO₃ (54.8 eV) representing the inorganic parts of SEI. After sputtering to discover the volume of the SEI (3.12 (d)), the peak shifts to a bigger energy of 55.2 eV which includes the signal Li₂O (55.8 eV) and Li-Li (54.6 eV). In addition, the existence of Li₂O inside the SEI is also proven by the O 1s peaks shown in Fig 3.12 (b) and (e). The signal at 528 eV assigned to Li₂O can only be observed in the volume of the SEI. Furthermore, the signal of SnO₂ can be found both at the surface and volume. As shown in Fig. 3.12 (c) and (f), there is no Sn-Sn signal on the surface, Sn is oxidized to SnO₂. However, in contrast to XRD and TEM electron diffraction patterns, the Sn signal can be found inside the SEI, which indicated that, after cycling, some Sn might remain in small fraction and size which escapes the resolution of XRD.

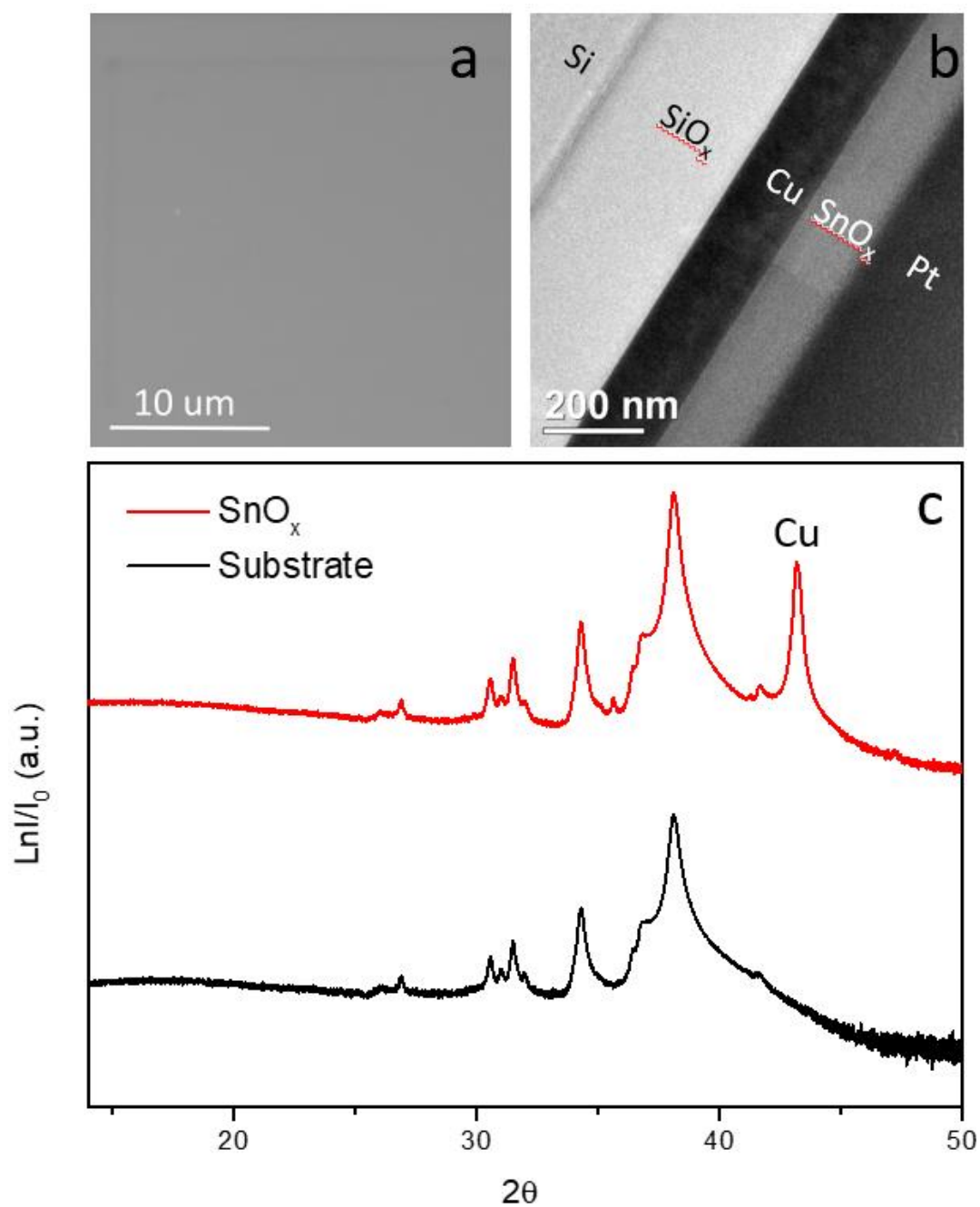
3.6 In-situ SEI formation of SnO_x 

Figure 3.13: Characterization of 100 nm SnO_x anode prepared by ion-beam sputter (a) SEM image, (b) TEM cross section micrograph and (c) XRD pattern of SnO_x .

In order to further check that the shift of the delithiation peak to smaller value is attributed to the oxidation of Sn, a layer of preoxidized SnO_x was deposited by reactive ion-beam sputtering and cycled in the same condition. As shown in Fig. 3.13 (a) and (b), different to pure Sn, both SEM image and TEM cross section indicate that the surface of SnO_x is smooth, which is probably attributed to the higher melting temperature of SnO_2 (1630 °C). Moreover, as shown in Fig. 3.13 (c), XRD patterns show that SnO_x is X-ray amorphous.

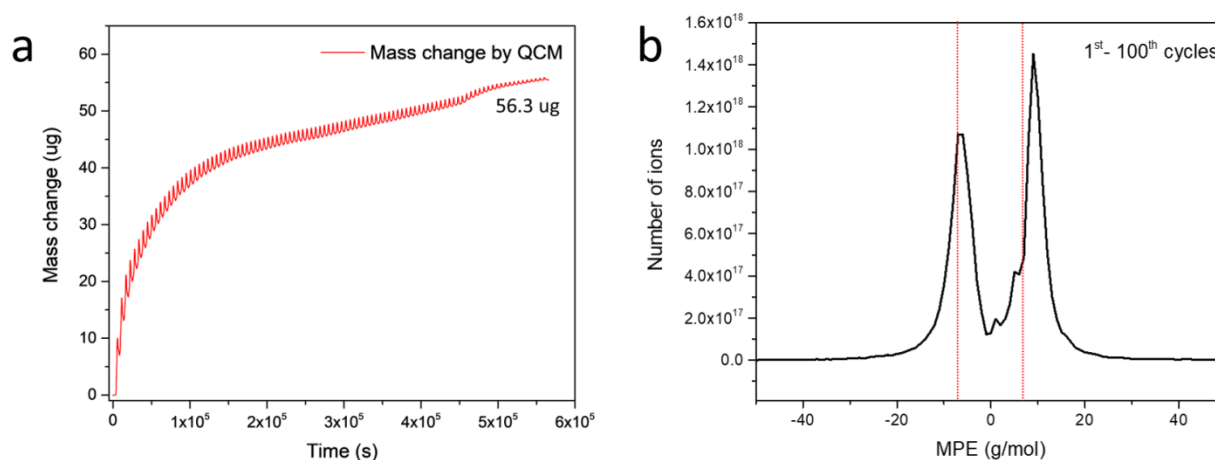


Figure 3.14: (a). Mass change measured by QCM and (b) over-all QCM mass spectrum of SnO_x .

Fig. 3.14 (a) presents the mass change by QCM, after 100 cycles, the total irreversible mass change (SEI mass) is 56.3 μg , somewhat less than that of pure Sn. Compared with pure Sn, the preoxidized SnO_x should have less Sn that could be oxidized during the cycling. Thus, if our assumption is correct, the shift of delithiation peaks in mass spectra must be less than that of Sn. Indeed, as shown in Fig. 3.14 (b), as expected, the delithiation peak (-6.5 - -7 g/mol) is very close to the -7 g/mol . The combination of above results provides convincingly evidence that the shift of the delithiation peak to small values in the mass spectra is attributed to the oxidation of Sn which competes with the delithiation reaction as expressed via equations (3.3) and (3.4).

3.7 Summary

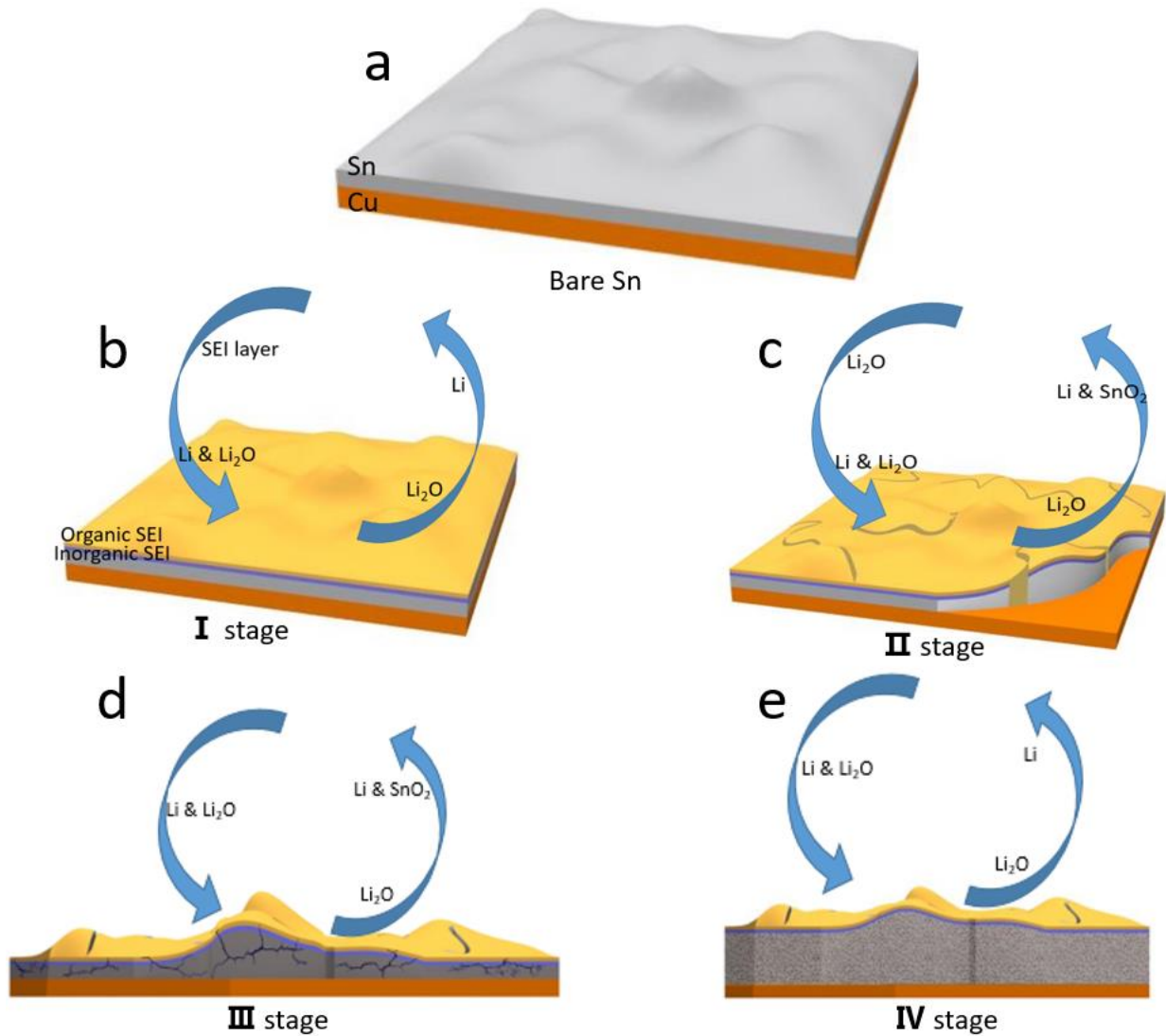


Figure 3.15: Schematics of long-term cycling and SEI formation of Sn

With the support of various characterization techniques (XPS, SEM, XRD and TEM), the mechanism of long-term cycling and SEI formation on Sn anode is proposed based on the three different MPE-based characteristics mass spectra, real-time MPE and integrated MPE. As shown in Fig. 3.15, each stage may be understood based on its reversible reactions (insertion/extraction

of lithium and lithium-based compounds) and irreversible reaction (SEI formation). Moreover, the forming order of various species is also provided, only the amounts of every species are not focused.

As seen in Fig. 3.15 (a), Cu (current collector) and Sn anode were deposited by ion beam sputtering. The surface of Sn is quite rough.

Stage I (1st cycle): As shown in Fig. 3.15 (b), due to the decomposition of electrolyte, the organic SEI including CH₃OLi and CH₂OCO₂Li forms before the inorganic SEI that mainly consisted of Li₂CO₃, LiOH and Li₂O. After the initial SEI formation, lithium alloys with the Sn anode and simultaneously forms also a fraction of Li₂O. In the delithiation step, the decomposition of Li₂O before the extraction of Li.

Stage II (2nd cycle - 5th cycles): As shown in Fig. 3.15 (c), the irreversible Li₂O forms in the potential range of 0.36 - 0.27 V. Subsequent lithiation, simultaneously insertion of Li₂O and Li take place. during the delithiation step, Li₂O still extracts before Li. Remarkably, the oxidization of Sn is found at the end of delithiation together with the extraction of Li. This oxidation appears relatively late at rather high voltage (i.e. >0.9 V vs Li/Li⁺), which is in general agreement with other reports, stating a stability of SnO₂ only above 0.9 V²⁹. Furthermore, in view of the working principle of QCM (measurement of the mass change loaded or uploaded on the electrode), the oxygen for the oxidization of Sn stems from the electrolyte. However, it cannot be decided whether the oxygen stems from decomposition of the organic solvent or the perchlorate counter ions.

Stage III (6th cycle - 45th cycle): As shown in Fig 3.15 (d), most of the processes in stage III are basically the same as those in stage II. The only difference is that no irreversible Li₂O formed anymore (in the potential window of 0.36 - 0.27 V).

Stage IV (46th cycle - 100th cycle): After the SEI formed in the first three stages, the electrode shows a quasi-stable state. Lithium and Li₂O reversible cycle on the Sn anode. Li and Li₂O are inserted simultaneously, while in delithiation, Li extracted after Li₂O. Quantitatively, the number ratio of reversible Li and Li₂O is 77 to 23.

Besides its chemical composition, the thickness of SEI can be measured by the QCM mass increase under a reasonable assumption on the density. Proved by the cross section micrograph of TEM, QCM can be used as a reliable in-situ thickness monitor of the SEI. Remarkably, the SEI formed by the decomposition of electrode and the oxidization of Sn, after 100 cycles, develops a remarkable thickness of 675 nm which is 6.75 times the thickness of the original bare Sn.

4 The effect of Sn thickness and working potential window on the SEI growth and cycling behavior of Sn

In chapter 3, the SEI formation and cycling behavior on a 100 nm Sn anode was investigated. Generally, the formation of SEI happens at the surface of the electrode and should therefore in first approximation be thickness-independent. However, we have found that Sn participates in the formation of SEI as Sn becomes oxidized during stage II and III at the end of delithiation. Moreover, as shown in Fig. 4.1, despite the general belief that SEI should form before the lithiation, the later SEI unexpectedly forms in a voltage range of 0.36 to 0.27 V (red) in which also a significant part of the lithiation happens predominantly in stage II. Thus, the goal of this chapter is a further clarification of the mechanisms of the SEI formation on Sn anodes by means of a controlled variation of the electrode thickness and of the potential window of operation.

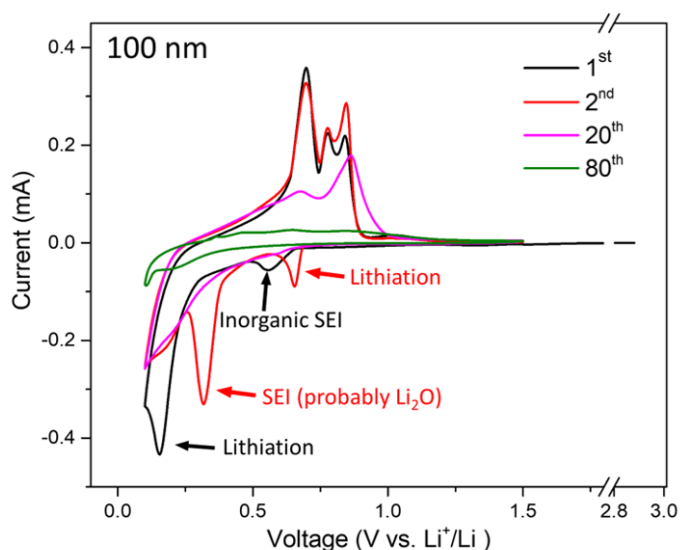


Figure 4.1: CV curves of a 100 nm Sn electrode at a scan rate of 0.5 mV/s in a potential window of 0.1-1.5V (1st, 2nd, 20th and 80th are selected to represent different stage, respectively).

4.1 Microstructure of Sn thin films with different thickness

Sn electrodes in different thickness were deposited by ion-beam sputtering. As shown in Fig. 4.2, the SEM surface images of Sn films of different thickness (20 nm, 50 nm, 100 nm and 150 nm) indicate a pronounced but similar surface roughness independent of thickness. As discussed in chapter 3, the significant roughness of Sn films is attributed to the very low melting temperature of Sn ($T_m=231.9\text{ }^\circ\text{C}$) and therefore relatively low surface energy¹⁰⁹.

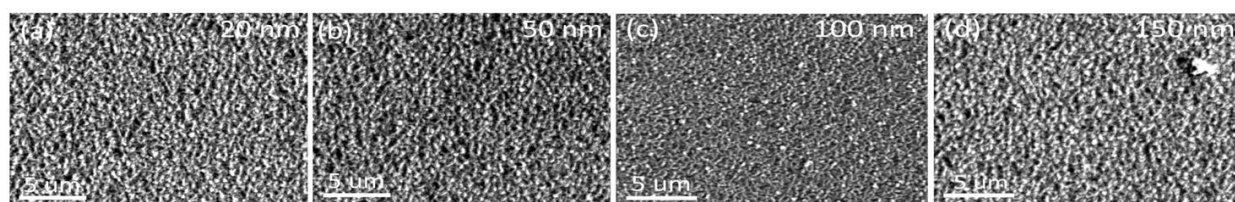


Figure 4.2: SEM surface images of different thickness of Sn (a) 20 nm, (b) 50 nm, (c) 100 nm and (d) 150 nm.

4.2 Electrochemical performance of Sn anodes of different thickness

With the same strategy as that in chapter.3, the electrochemical characterizations of Sn electrodes of different thicknesses (20 nm, 50 nm, 100 nm and 150 nm) were performed. Fig. 4.3 shows the CV curves of these four samples, cycled at a scan rate of 0.5 mV/s in a potential window of 0.1 to 1.5 V (with respect to Li reference). The same cycle number as in chapter.3, the 1st, 2nd, 20th and 80th, cycles were selected to reflect the four main stages of SEI formation, respectively. As shown in Fig. 4.3 (b) to (d), the thicker Sn anodes (50 nm, 100 nm and 150 nm) show a similar electrochemical behavior. As marked in Fig. 4.3 (c), the peak at around 0.6 V (the lithiation of the first cycle, black) and 0.3 V (the lithiation of the second cycle, red) represent the formation of inorganic SEI, while the negative peak at 0.15 V (first cycle, black) and 0.65 V (second cycle, red),

and the positive peaks at 0.7 V, 0.78 V, 0.86 V correspond to the lithiation and delithiation, respectively. Also, with the increase of cycle number, the peak shifting or weakening for these thicknesses are quite similar. However, as shown in Fig. 4.3 (a), the thinner film (20 nm Sn) shows a significantly different redox behavior especially in the 1st and 2nd cycle (black and red). In other words, some of the characteristic peaks representing the stage I and II are not obvious. In detail, for the 1st cycle, the negative current peak at around 0.6 V is weaker indicating that the amount of inorganic SEI formed at the 1st cycle has significantly decreased. Later the MPE based analysis of 20 nm will focus on the new shoulder at 0.4 V. In addition, the positive peaks at 0.7 and 0.78 V disappeared. To our surprise, there is no stage II for 20 nm Sn (irreversible Li₂O formed in a potential window of 0.36 - 0.27 V), But the direct transition to stage III. The stage III and IV (represented by 20th and 80th cycles) are quite similar for all four thickness.

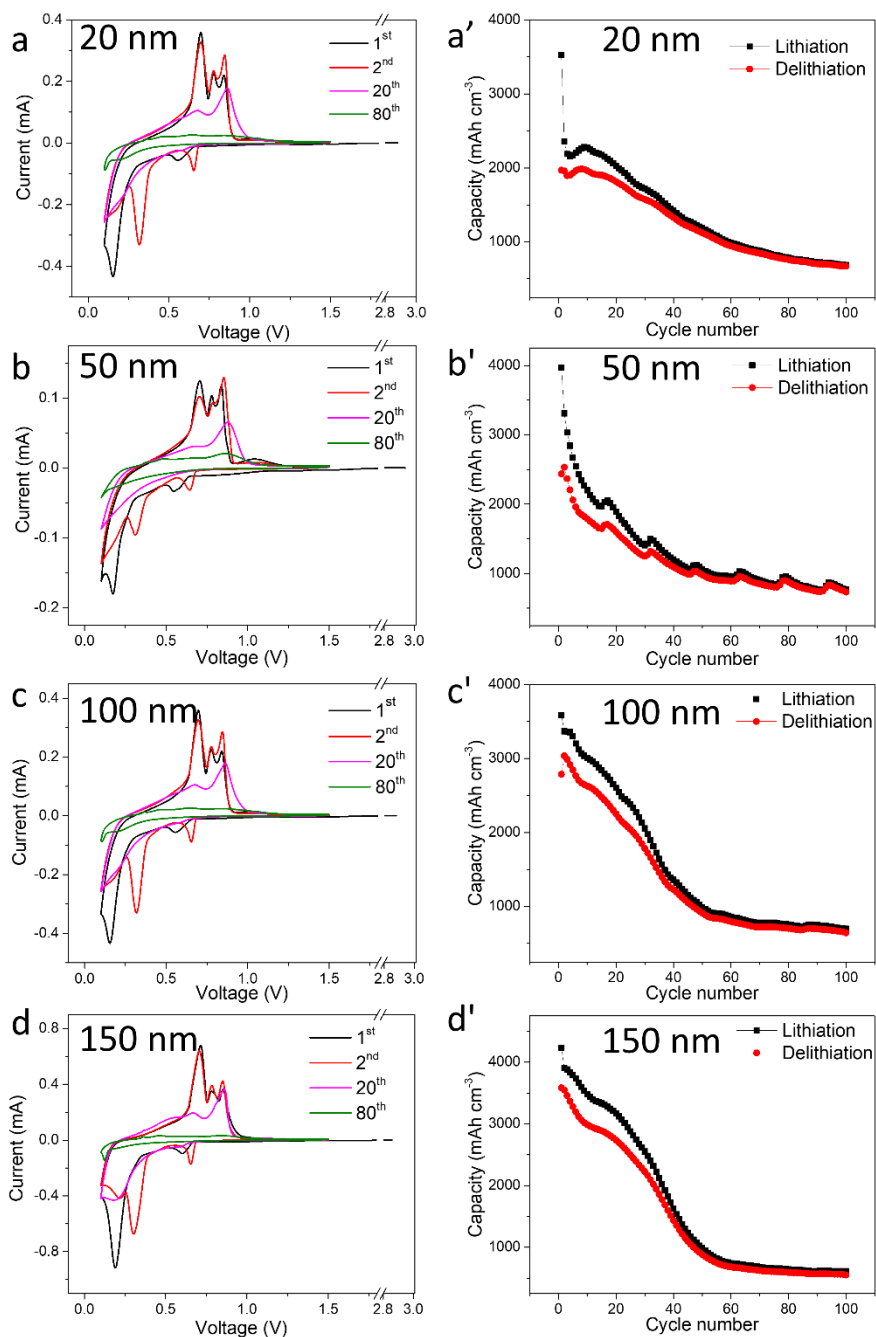


Figure 4.3: CV curves of different cycles as labeled for Sn thicknesses 20 nm (a), 50 nm (b), 100 nm (c) and 150 nm (d); Electrochemical capacity of Sn electrodes of different thickness (a') 20 nm, (b') 50 nm, (c') 100 nm and (d') 150 nm at a scan rate of 0.5 mV/s in a potential window of 0.1 - 1.5 V.

Based on the CV data, the electrochemical capacity of the different Sn anodes was calculated by integrating current over time (see 2.4.1). As shown in Fig 4.3 (a') – (d'), the capacities of all

samples decrease continuously with cycle number until around the 60th cycle and then remain at around 600-750 mAh cm⁻³. This capacity fade has been discussed in chapter 3.

4.3 The SEI formation and cycling behavior on 20 nm Sn

As indicated above, 20 nm Sn exhibits a different SEI formation process. Similar to the analysis in chapter 3, three kinds of MPE curves including the over-all mass spectrum, the real-time MEP and integrated MPE are shown in Fig 4.4, 4.5 and 4.6, respectively.

For the 1st stage (1 cycle), as shown in Fig. 4.6 (a), the organic SEI (MPE = 44.9 g/mol, blue line) forms before the inorganic species (MPE = 23.2 g/mol, orange line). Although, the SEI formation is basically a surface effect, compared with 100 nm Sn (around 2 ug), 20 nm Sn has significant less amount of SEI (around 0.7 ug). Moreover, it is worth to mention that the MPE of the inorganic SEI on 20 nm Sn (23.2 g/mol) is quite bigger than that on 100 nm Sn (17.9 g/mol). As shown in Table. 3.1, for all expected inorganic species, only the MPE of Li₂CO₃ is bigger than 23.2 g/mol. Thus, probably the relative fraction of Li₂CO₃ is increased in the SEI of 20 nm Sn. Obviously, due to the bad protection by thinner SEI, the oxidization of Sn already starts at the end of the delithiation in 1st cycle. For the stage II, same as the CV results (Fig. 4.3 (a)) there is no individual Li₂O formed. However, for the delithiation step, there is no signal that indicates the oxidization of Sn, also in stage III and stage IV. Last but not least, as demonstrated by the abnormal large MPE (39.8 g/mol, blue line in Fig 4.6 (d)), organic SEI is deposited even in stage IV (a stable stage of 100 nm Sn), which is probably due to the organic SEI formation after cracking.

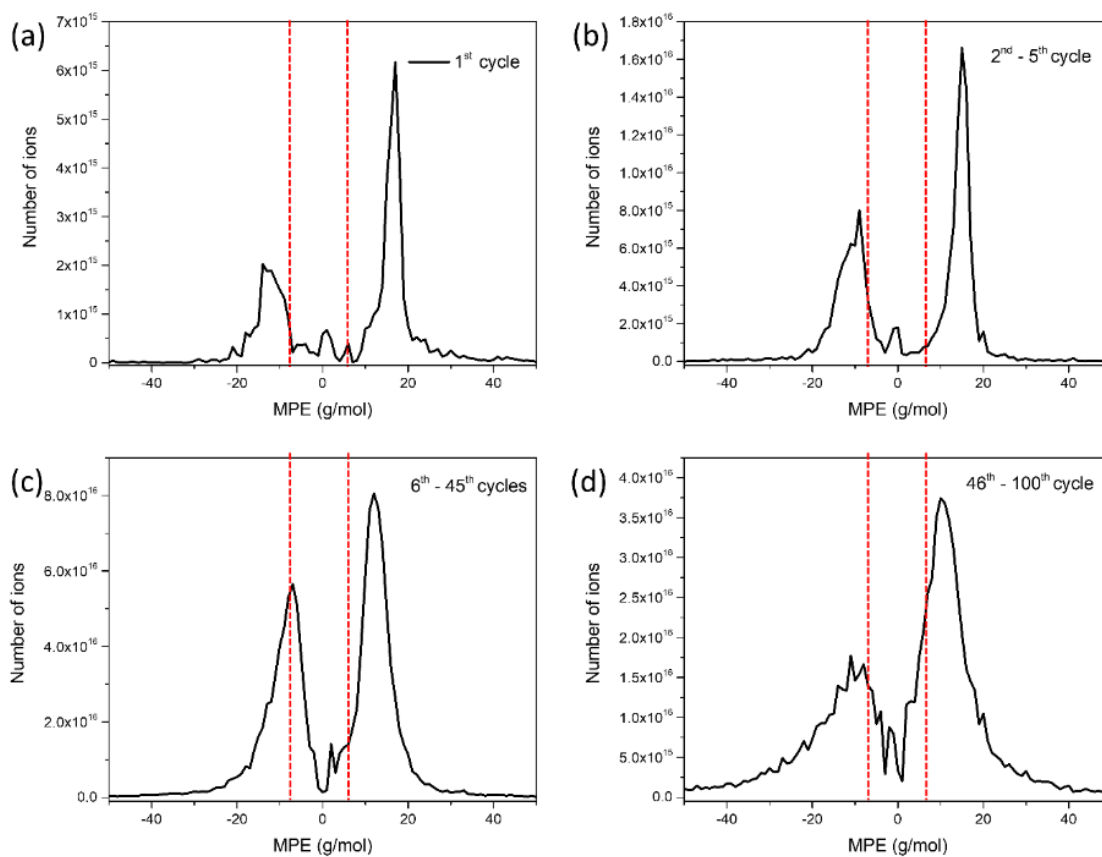


Figure 4.4: Mass spectra of 20 nm Sn after (a) 1st cycle (stage I), (b) 2nd-5th cycles (stage II), (c) 6th-45th cycles (stage III) and (d) 46th - 100th cycles (stage IV).

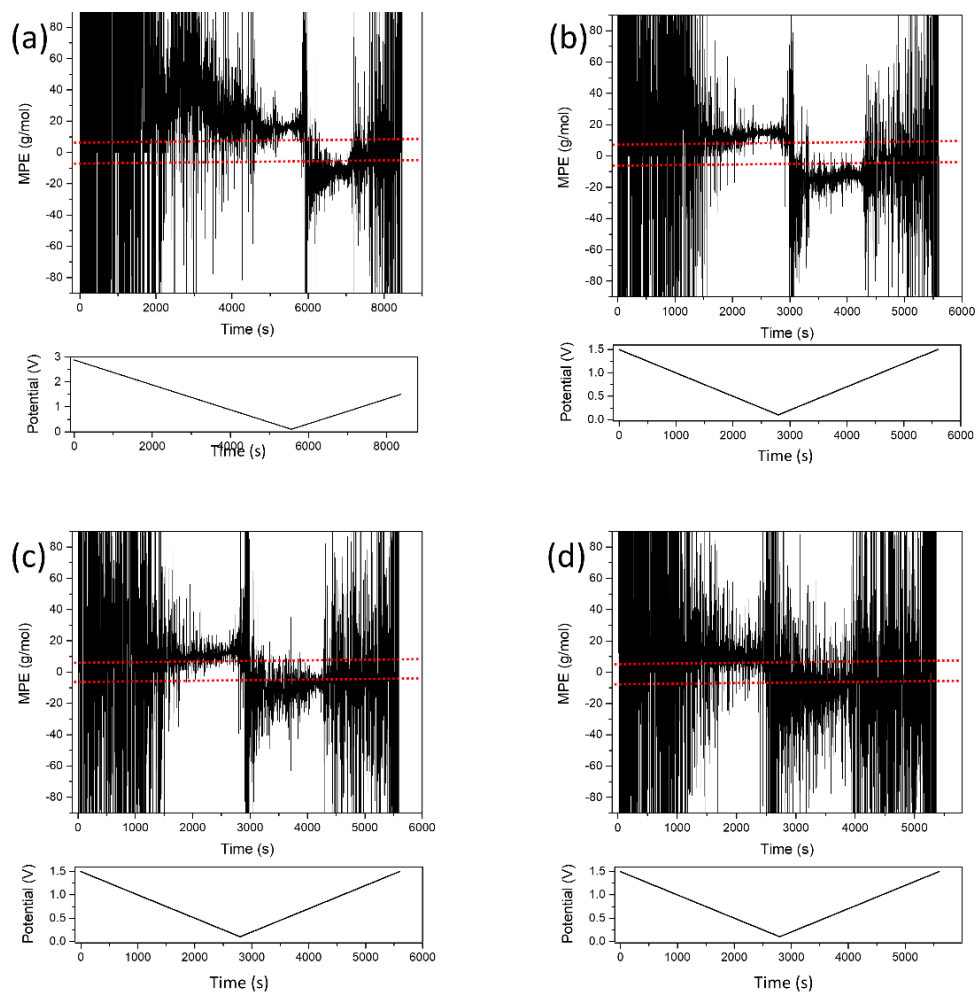


Figure 4.5: Real-time MPE curve of 20 nm Sn (a) 1st cycle (stage I), (c) 2nd cycle (stage II), (d) 20th cycle (stage III) and (d) 80th cycle (stage IV).

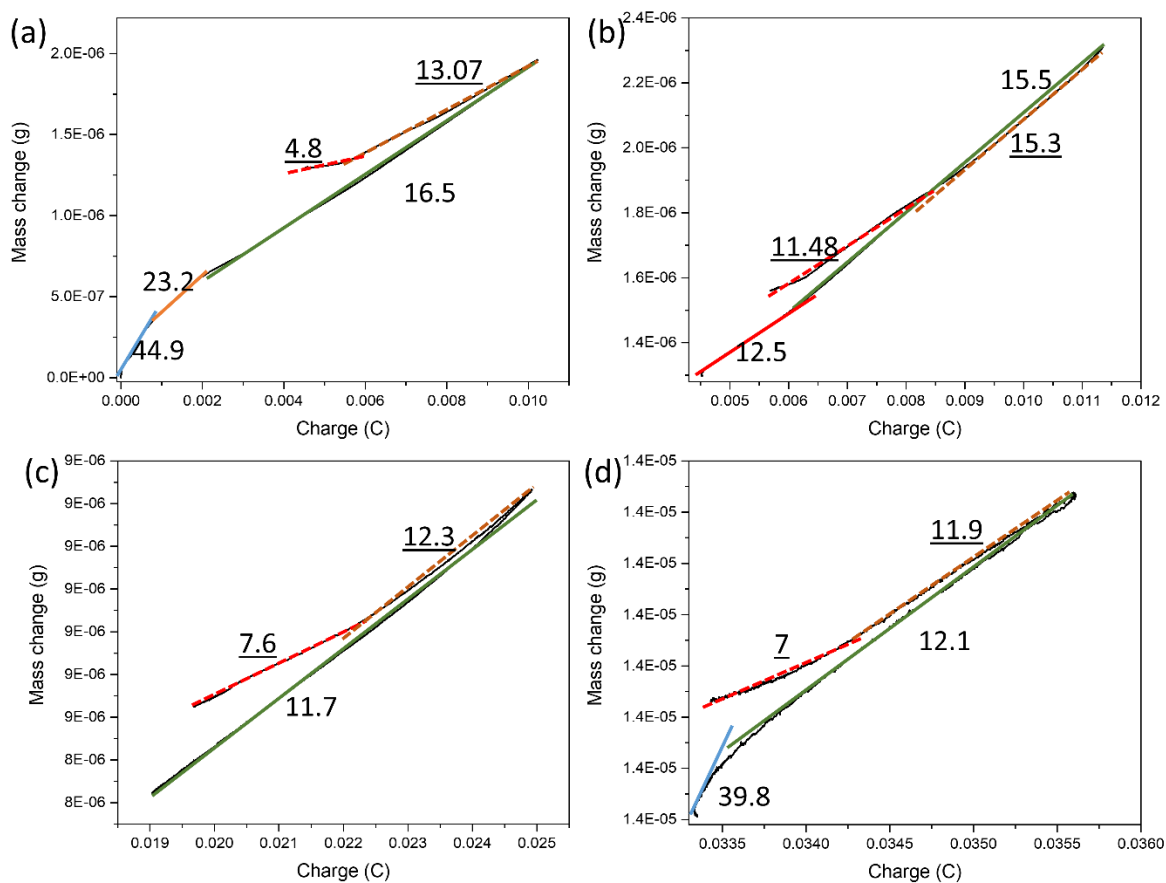


Figure 4.6: The integrated MPE of (a) 1st cycle (stage I), (b) 2nd cycle (stage II), (c) 20th cycle (stage III) and (d) 80th cycle (stage IV). Solid lines mark the MPE during lithiation half cycle, while dotted lines represent the MPE during delithiation half cycle.

4.4 The dependence of SEI growth on the Sn thickness

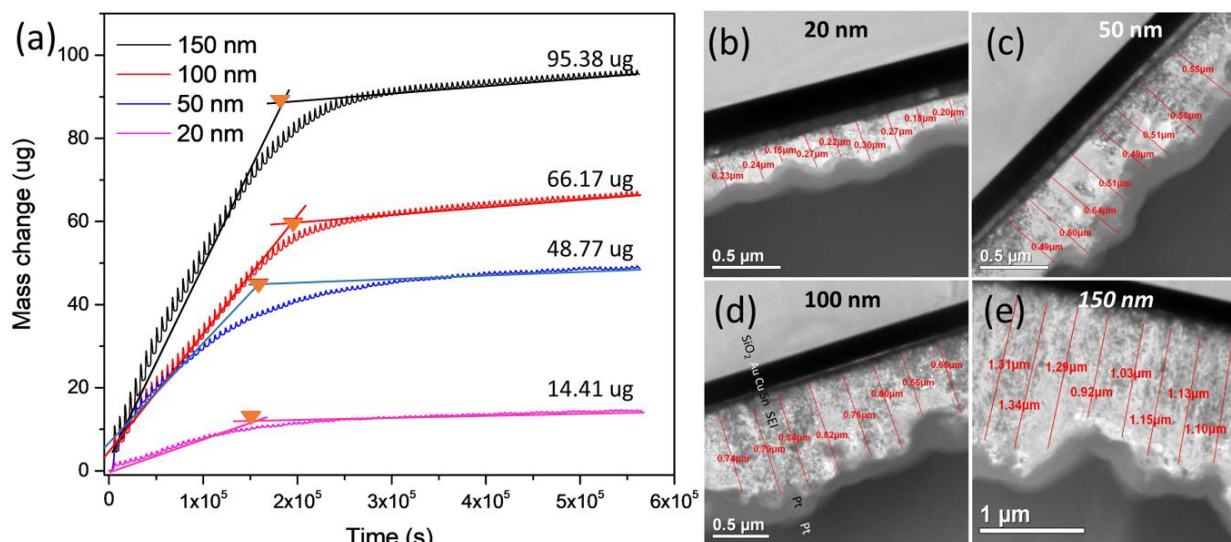


Figure 4.7: (a) Mass changes of different sample thicknesses (20 nm, 50 nm, 100 nm, and 150 nm) measured by QCM from the 1st cycle to the 100th cycle. (b-e) TEM micrographs of electrodes of different thickness after 100 cycles (b) 20 nm, (c) 50 nm, (d) 100 nm and (e) 150 nm.

As discussed in chapter 3, we found that Sn is oxidized and participates in the formation of SEI.

In this case, a certain dependence must be expected. In order to investigate the effect of sample thickness on the formation of SEI, the in-situ mass change of four thickness of Sn (20 nm, 50 nm, 100 nm and 150 nm) were measured by QCM as shown in Fig. 4.7, respectively. As discussed in chapter 3, the continuous increase of the averaged baselines indicates an irreversible mass-load (SEI formation), while the periodic oscillations represent the reversible process of lithiation and delithiation. For each mass change curve, qualitatively, the in-situ mass change of these four samples have a similar increase trend, which can be divided into two steps (the position marked by red triangles may represent the dividing points). The first step (including stages I, II and III)

exhibits a linear growth of SEI which is probably attributed to the Sn cracking, while the second step (stage IV) shows a low and gradually decreasing growth rate that might be understood as a diffusion controlled (parabolic) growth process. After, 100 cycles, the irreversible mass change (SEI mass) of these four sample are 14.41 μg (20 nm), 48.77 μg (50 nm), 66.17 μg (100 nm) and 95.38 μg (150 nm) corresponding to 43.43 $\mu\text{g}/\text{cm}^2$, 146.99 $\mu\text{g}/\text{cm}^2$, 199.43 $\mu\text{g}/\text{cm}^2$ and 287.46 $\mu\text{g}/\text{cm}^2$, respectively. In other words, the SEI mass systematically increases with the Sn thickness, which strongly provide evidence that Sn participates in the formation of SEI. In order to further investigate the relationship between SEI thickness and sample thickness, TEM cross section micrographs of these four samples after 100 cycles were investigated and shown in Fig. 4.7 (b) - (c), respectively. As labeled in Fig. 4.7 (d), the complete layer structures consists of the QCM sensor (quartz, Ti and Au), current collector (Cu), anode (Sn), SEI and protecting layer for lamella lift-out (Pt). In view of the roughness of SEI, 8 positions along the interface were selected to average. As shown in Table. 4.1, the thickness of SEI are 228 ± 4.5 nm (20 nm), 546 ± 5.7 nm (50 nm), 745 ± 9.0 nm (100 nm) and 1158 ± 13.5 nm (150 nm), respectively.

Table 4.1: The comparison between QCM and TEM results on the SEI thickness and the resulting average density

Sample	20 nm	50 nm	100 nm	150 nm
Method				
QCM thickness (nm)	162	549	744	1073
TEM thickness (nm)	228 ± 4.5	546 ± 5.7	745 ± 9.0	1158 ± 13.5
Deviations between TEM and QCM	<u>$40.7 \pm 2.7\%$</u>	$0.5 \pm 1.3\%$	$0.1 \pm 1.2\%$	$7.9 \pm 1.3\%$
Density of SEI (g/cm^3)	<u>1.55 ± 0.06</u>	2.19 ± 0.01	2.18 ± 0.01	2.02 ± 0.03

As shown in Fig. 4.8 (a) and (b), both TEM thickness and SEI mass may be understood through a linear relation with sample thickness. The corresponding equations are shown below:

$$Y_{SEI} = (7.6 \pm 0.8) X_{Sn} + (78.2 \pm 16.8) \text{ nm} \quad (4.1)$$

$$M_{SEI} = (1.7 \pm 0.8) X_{Sn} + (29.73 \pm 25.05) \text{ ug/cm}^2 \quad (4.2)$$

where Y_{SEI} , M_{SEI} and X_{Sn} represent the SEI thickness, SEI mass per area and tin thickness, respectively.

The following discussion will focus on the relationship between TEM thickness of SEI and initial Sn thickness. The comparison between TEM thickness and SEI mass will be discussed afterwards. As discussed above, the uptake of irreversible SEI mass is reasonably split into two parts (shown in Fig. 4.7 (a)). Thicker samples break down to stable sized samples (X_0) yielding larger average crack lengths resulting in more SEI forming per cycle (higher slope of the trendline). Furthermore, as shown in TEM cross section micrographs (Fig. 4.7 (b)-(e)), many black spherical particles (BSP) represent remaining Sn distributed in the SEI. Remarkably, in all of these samples, if we exclude the agglomerated region, the Sn particles have a similar diameter (20-30 nm). Thus, we strongly believe that, with the cycle going on, the Sn thin films with different thickness crack until similarly sized fragments ($X_0 = 20 - 30 \text{ nm}$) are formed. This X_0 suggests the transition from SEI growth by cracking ($X_{Sn} > X_0$), to growth by diffusion ($X_{Sn} \leq X_0$). Therefore, equation 4.1 may be better stated as:

$$Y_{SEI} = 7.6 \cdot (X_{Sn} - X_0) + A \quad (4.3)$$

where A is a constant thickness offset which equals to $78.2 \text{ nm} + 7.6 X_0 \approx 270 \text{ nm}$.

As demonstrated in equation 4.3, the major contribution that is affected by the Sn thickness can be linked to the Sn cracking and the oxidization of Sn. The constant thickness A is probably assigned to both the usual SEI formed according the decomposition of electrolyte especially in the first cycle, and the slow diffusional oxidization of Sn.

To further investigate the difference of the oxidization of Sn on different thickness Sn, the overall mass spectra of different electrode thicknesses are shown in Fig.4.8 (c) - (f). As discussed in chapter 3, the shift of the delithiation peak to absolute values smaller than 7 g/mol is attributed to the oxidization of Sn. Quantitatively, shift (ΔMPE) can be expressed by equation 4.4.

$$\Delta MPE = \text{Measured MPE} - \text{MPE of delithiation} \quad 4.4$$

The measured MPE consists of two parts: delithiation (-7 g/mol) and the oxidization of Sn (8 g/mol). As shown in equation 4.5, the measure *MPE* is the weighted average of these parts.

$$\text{Measured MPE} = \left\{ 8 \frac{Q_{Sn}}{Q_{de}} + (-7) \left(1 - \frac{Q_{Sn}}{Q_{de}} \right) \right\} \quad 4.5$$

Where, Q_{Sn} is the charge transfer attributed to oxidization of Sn, Q_{de} represents the total charge desorbed during a delithiation half cycle, $\frac{Q_{Sn}}{Q_{de}}$ and $\left(1 - \frac{Q_{Sn}}{Q_{de}} \right)$ are the amount proportion of transfer charge for the oxidization of Sn and delithiation, respectively.

Combining equation 4.4 and 4.5, ΔMPE is calculated via equation 4.6. Additionally, for the next comparison between different thicknesses

$$\Delta MPE = \left\{ 8 \frac{Q_{Sn}}{Q_{de}} - 7 \left(1 - \frac{Q_{Sn}}{Q_{de}} \right) \right\} - (-7) = 15 \frac{Q_{Sn}}{Q_{de}} = 15 \frac{Q_{Sn}/volume}{Q_{de}/volume} \quad 4.6$$

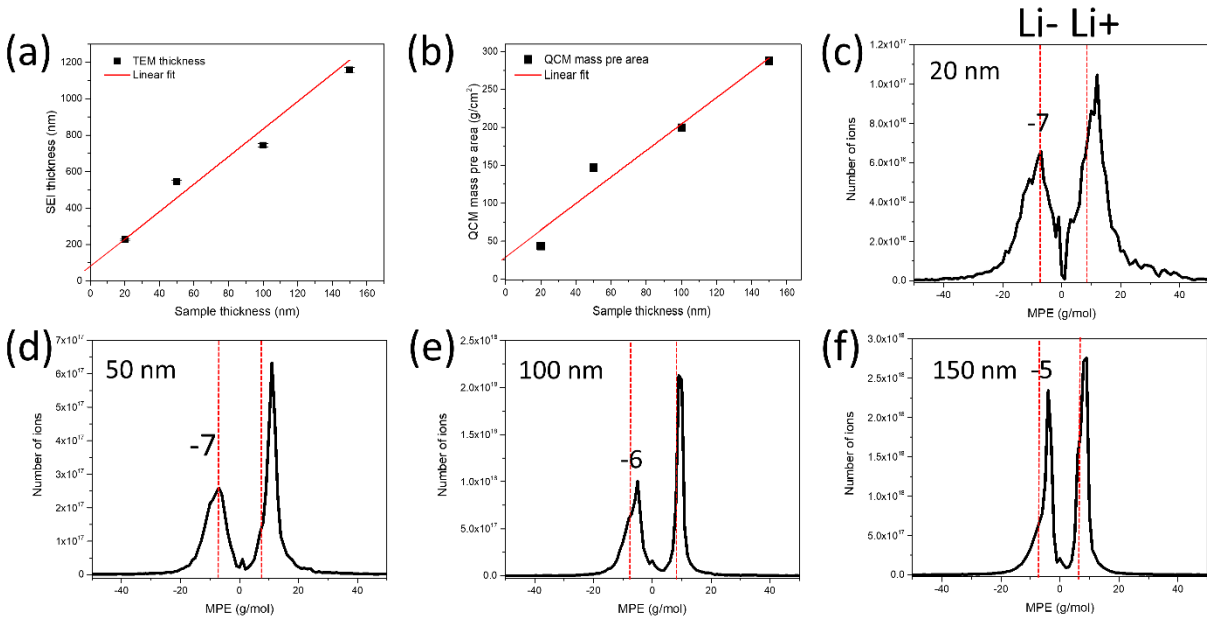


Figure 4.8: The relationship between initial Sn thickness with SEI thickness after 100 cycles as determined by TEM measurement (a), and SEI mass per area after 100 cycles as measured by QCM, the over-all QCM mass spectra of different thickness Sn (c) 20 nm, (d) 50 nm, (e) 100 nm and (f) 150 nm. The exact positions of the delithiation peaks are labeled within the figures.

As shown in Fig. 4.4 (a') - (d'), it is clear that the specific capacities of these four samples are similar. And as shown in Fig. 4.9, Q_{de} has a linear relationship with sample thickness which indicates that the total charge per volume (Q_{de}/volume) keeps constant and independent of sample thickness. Thus, the (Q_{sn}/volume) should increase with sample thickness. In other words, more proportion of Sn was oxidized in thicker sample.

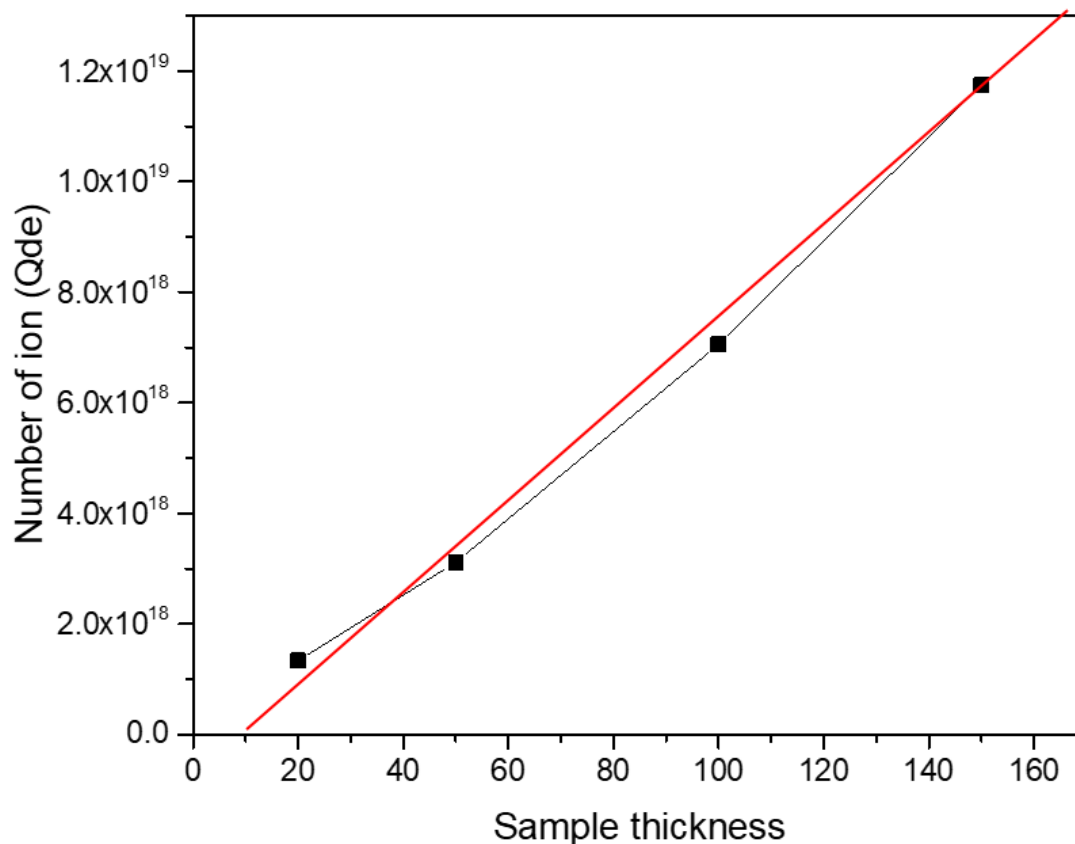


Figure 4.9: Relationship between sample thickness and transferred charge during delithiation (from the 1st – 100th cycle) at a scan rate of 0.5 mV/s.

As discussed in chapter 3, the QCM mass can be converted to the SEI thickness with a reasonable assumption of the density, and a court density (2.18 g/cm^3) was used for the following estimation. As shown in Table. 4.1, except 20 nm Sn, the calculated thickness is in good agreement with its TEM thickness (the error is within 10 % and reasonable in view of roughness). However, in the case of the 20 nm thickness Sn, the huge deviation ($40.7 \pm 2.7\%$) between QCM thickness and TEM thickness must be attributed to the overestimation of the density. As discussed in 4.3, the SEI of 20 nm Sn is an organic-rich layer. The density of possible species in SEI (shown in Table 4.2)

demonstrate that the density of organic species is way smaller than 1.5 g/cm³. Inspired by Table 4.2, a more accurate density of SEI was calculated by QCM mass and TEM thickness by equation 4.5.

$$\bar{\rho} = \frac{\Delta m_{\text{QCM}}}{\text{surface area} \times \text{TEM thickness}} \quad 4.5$$

As shown in Table 4.1, the densities of SEI on 50 nm, 100 nm and 150 nm Sn are indeed close to the assumed density (2.18 g/cm³), which indicates that the SEI mainly consist of inorganic species. On the contrary, the density of SEI on 20 nm Sn is significantly less, which further proves that the SEI on 20 nm Sn is an organic-rich layer.

Table 4.2: The densities of possible species of the SEI

Density of possible species of SEI	
Deposited species	Density (g/cm ³)
Li ₂ O	2.01
Li ₂ CO ₃	2.11
LiCl	2.07
LiOH	2.54
Polyolefins	0.9
Poly(ethylene oxide)	1.13-1.24

Besides the irreversible mass increase (SEI growth), the reversible mass change should also be investigated. As discussed in chapter 3 and previous work⁹¹, both Li and Li₂O are found as reversible species cycling on the anode (Sn and Si). As shown in Fig. 4.10, the amplitudes of the both QCM (black) and CV (red) mass oscillations were strictly calculated by using the ending mass of each half cycle minus its starting mass. In order to investigate the amount of reversible Li₂O,

different ratios of Li_2O and Li used to fit the CV amplitude to the QCM amplitude (the CV mass was calculated under assumption that Li is the only reversible species). Based on this kind of calculation, the proportion of reversibly processed Li_2O is determined to 49% (20 nm), 27% (50nm), 23% (100 nm) and 16% (150 nm), respectively. But, as shown in Fig. 4. 10 (e), the absolute amounts of reversible Li_2O pre cycle is increasing, when calculated as in section 2.4.5. It is clear that the absolute amount of reversible Li_2O increase with the sample thickness. As discussed in chapter 3, the formation of Li_2O is probably due to the decomposition of electrolyte, which should be only attributed to the surface area. However, as discussed in previous work of Si, the amount of Li_2O may be controlled by the over-potential of lithiation. Kinetically, this over-potential increases with the sample thickness. If we think of SEI and Sn in the stable stage as a whole electrode., the thickness of this electrode increase with Sn thickness, as shown in Fig. 4.4 (b) - (e). Thus, similar to the case of Si, the amount of reversible Li_2O increase with sample increase of thickness. We will discuss the reversible Li_2O detailed in chapter 5 (reversible Li_2O formation on Ge anode).

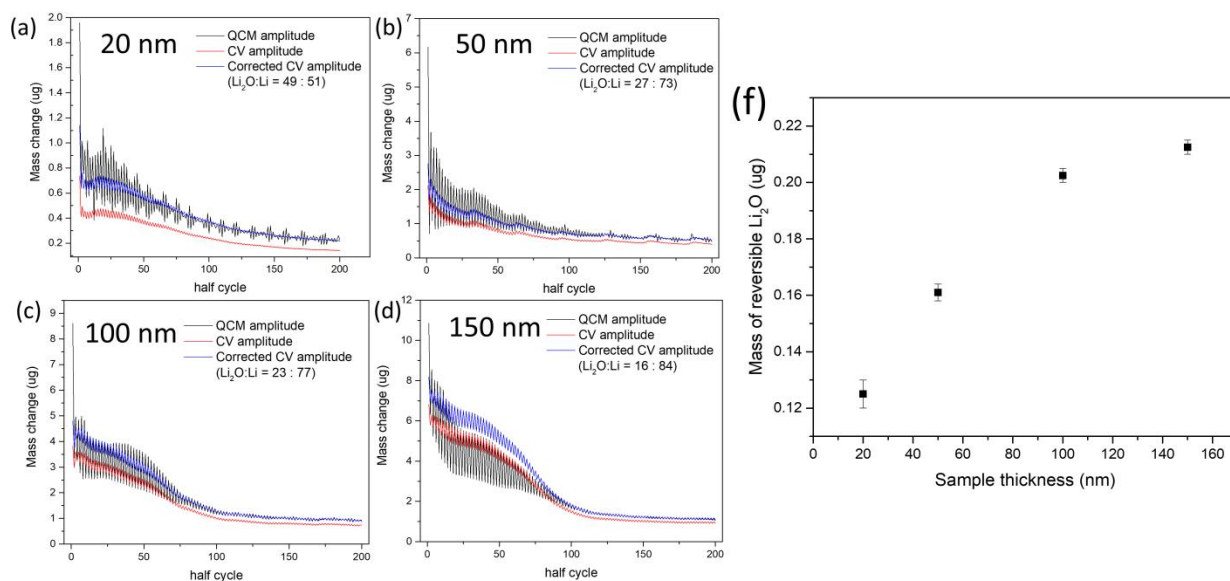


Figure 4.10: The reversible mass change observed for different Sn thickness (a) 20 nm, (b) 50 nm, (c) 100 nm and (d) 150 nm measured by QCM (black), calculated from CV under assumption of purely lithiation (red), derived from CV under assumption of given ratio (as labeled) between Li_2O and Li (blue) and (f) the dependence of the absolute mass of reversibly cycled Li_2O versus the Sn thickness.

4.5 The SEI formation in dependence on potential window of cycling

As indicated in chapter 3, the SEI formation on Sn is a voltage-dependent process, especially the inorganic species are formed in the potential window of 0.36 V - 0.27 V during the later cycle. Moreover, as reported in other works, the amount of Li insertion is also determined by the applied potential window. Thus, widening at the lower margin towards zero voltage vs Li/Li^+ can efficiently increase the amount of inserted Li. In this section, the effect of the working potential window on the SEI formation and cycling behavior is investigated.

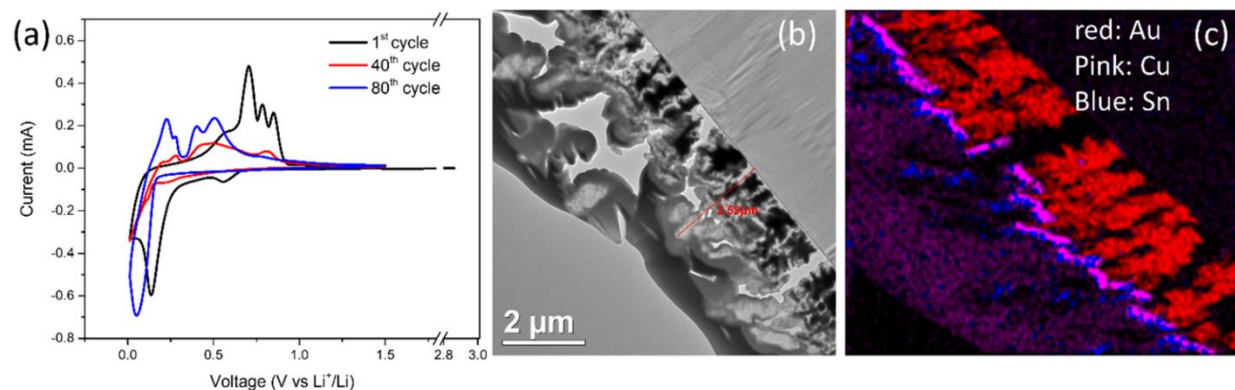


Figure 4.11: (a) CV curves of a 100 nm Sn electrode at a scan rate of 0.5 mV/s in a potential window of 0.01-1.5 V after 100 cycle. (b) TEM micrograph of Sn0.01 after cycling, (c) the corresponding EDX mapping of the TEM micrograph (Au (red), Cu (Pink) and Sn (Blue)).

100 nm thick Sn electrodes were cycled in different voltage ranges (0.01 - 1.5 V, 0.1 - 1.5 V, 0.2 - 1.5 V and 0.4 - 1.5 V), which are labeled as Sn0.01, Sn0.1, Sn0.2 and Sn0.4, respectively. Normally,

with the increase of cycle number, due to the continuous SEI formation, the current of charging should decrease. However, as shown in the CV curve (Fig. 4.11 (a)), the lithiation peak at around 0.2 V first decrease and then increase. In view of the wider potential window, this abnormal phenomenon is probably attributed to reactions after the Sn cracking. A TEM cross section micrograph (Fig. 4. 11 (b)) and corresponding EDX mapping (Fig. 4. 11 (c)) were produced to investigate the microstructure of the electrodes after cycling. The figure makes clear that after 100 cycles, all of the substrate (Au), current collector (Cu) and anode (Sn) were cracked. As reported in previous work, Li alloy with Au at the voltage around 0.2 V (vs. Li/Li⁺)¹¹⁴. Thus, the unusual current increase may be assigned to the alloying of Li into the Au. In view of the working principle of QCM, we are not allowed to separately investigate these two processes (lithiation of Sn and Au). Hence, we did no further analyze this sample.

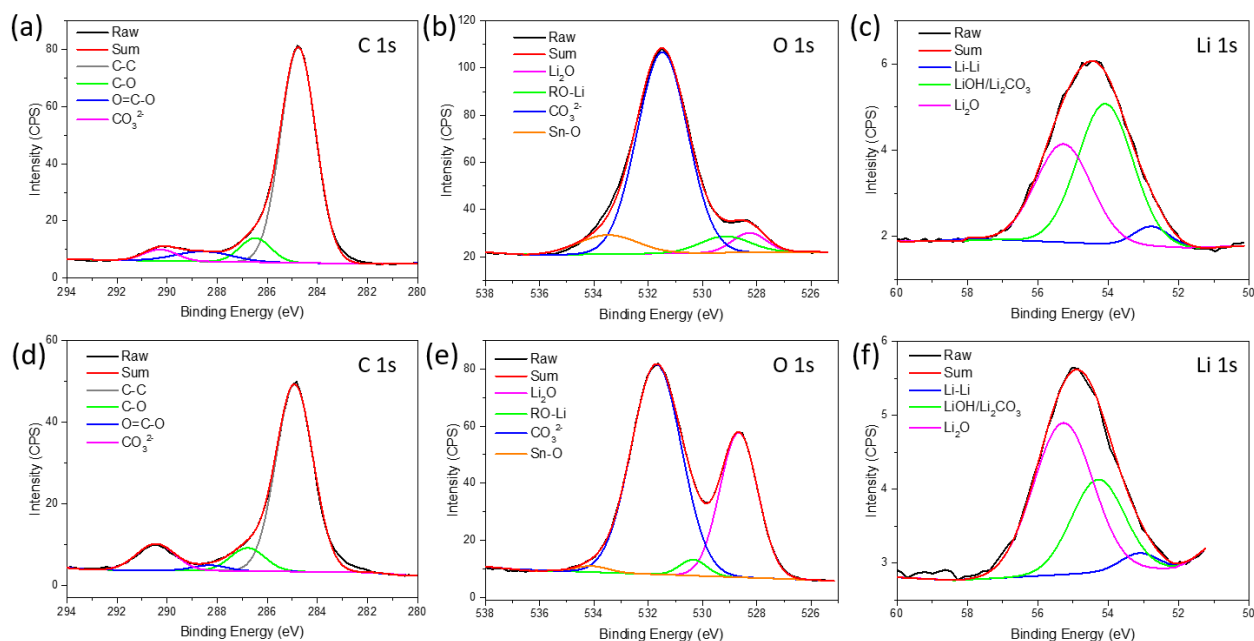


Figure 4.12: XPS data of the 100 nm Sn films processed to different voltage. The data are directly measured from the surface of electrode without any sputtering: First column (a, d) shows the binding

energy of carbon 1s peak, second (b, e) the binding energy of oxygen 1s peak and third column (c, f): the binding energy of lithium 1s peak. The top row (a, b and c) shows the result after one complete cycle and subsequent lithiation to 0.4 V vs Li/Li⁺, the bottom row (d, e and f) after one complete cycle and subsequent lithiation to 0.2 V vs Li/Li⁺.

Besides, the later SEI formation within the voltage range of 0.36 - 0.27 V (stage II) is also interesting. Firstly, the ex-situ XPS measurements of 100 nm Sn cycled at different voltage cut-off (sample 1: one complete cycle and subsequent lithiation to 0.4 V vs Li/Li⁺ and sample 2: one complete cycle and subsequent lithiation to 0.2 V vs Li/Li⁺), respectively. Thus, the extra signal of the sample charged to 0.2 V should stem from the SEI formed in the window of 0.36 - 0.27 V. As shown in Fig 4.12 (a) and (d), the weak increase of the signal at 290.6 eV is assigned to a small amount of Li₂CO₃. But, the significant enhancements of the peaks at 528.4 eV of O 1s and 55.2 eV of Li 1s peak convincingly demonstrate that the main species formed in this potential window is Li₂O.

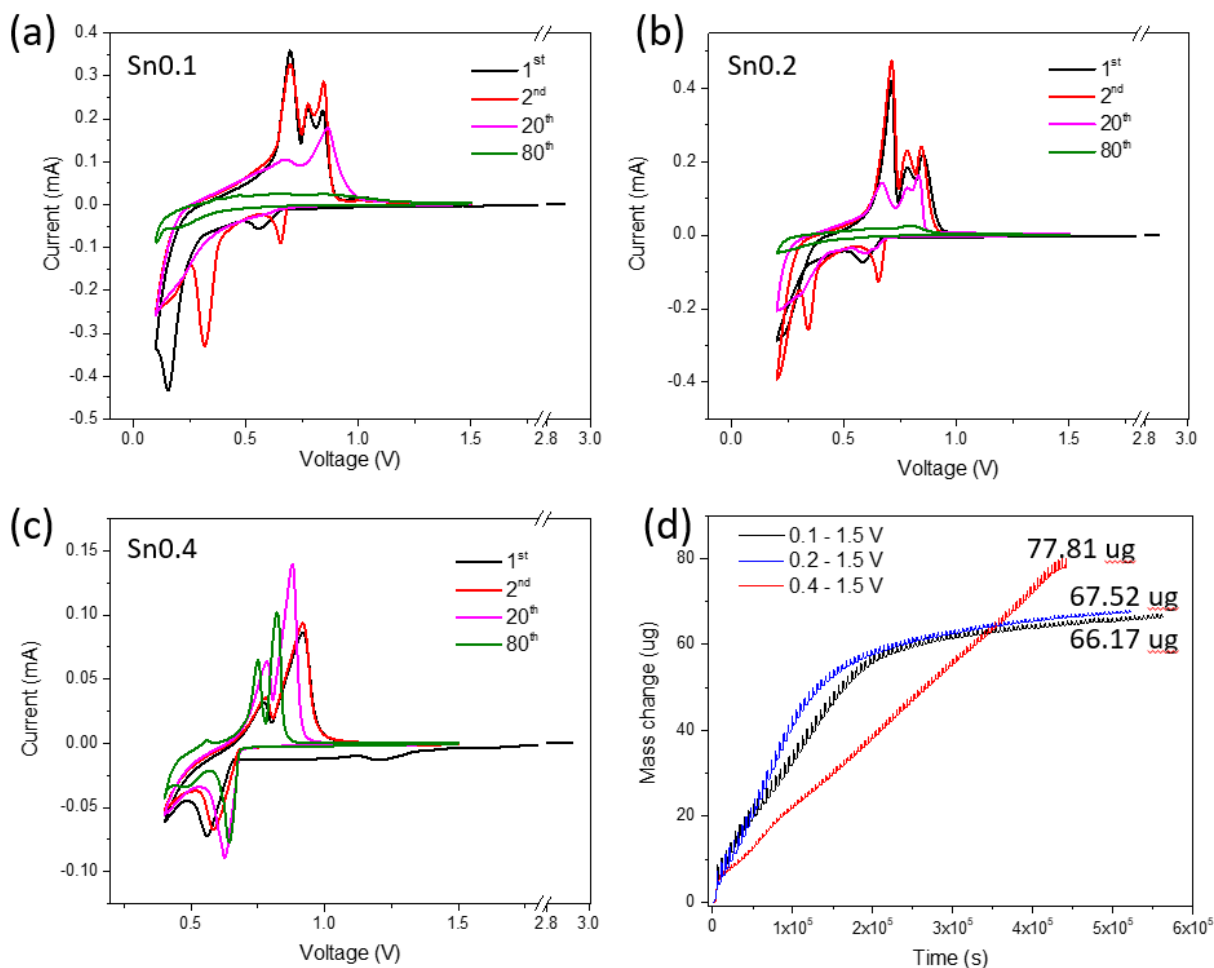


Figure 4.13: CV curves of a 100 nm Sn electrode cycled at 0.5 mV/s in a potential window of (a) 0.1 to 1.5 V, (b) 0.2 to 1.5 V and (c) 0.4 to 1.5 V, and (g) the corresponding QCM mass changes (0.1 - 1.5 V, 0.2 - 1.5 V and 0.4 - 1.5 V).

In order to identify the role of the later SEI (Li_2O and Li_2CO_3) formed in the voltage range of 0.36 - 0.27 V, 100 nm Sn were cycled under different potential windows (with the formation of this later SEI formation: 0.1 - 1.5V and 0.2 - 1.5 V, and without: 0.4 - 1.5 V). As shown in Fig 4. 13. (a) and (b), the CV curve of Sn0.1 and Sn0.2 show a similar redox performance which has been already discussed above. Also, as shown in Fig 4.13 (d), the QCM mass of Sn0.1 (black) and Sn0.2 (red) are very close. However, without the formation of this SEI, as shown in Fig 4.13 (c), the

peaks at around 0.6 V are not weakened. Attributed to less lithium insertion, electrodes cycled within a narrow potential window usually show a more stable electrochemical performance. But interestingly, the irreversible mass change shows continuous linear growth, and the final SEI mass (77.8 ug) is even bigger than those of Sn0.1 (66.17 ug) and Sn0.2 (67.52 ug). It is well accepted that the formed SEI can chemically insulate the electrode from the electrolyte to prevent further decomposition of the latter. However, the linear growth of SEI on Sn0.4 suggests a less-protective SEI against electrolyte decomposition.

To clarify the reason why the SEI formed on Sn0.4 could not prevent the further decomposition of electrolyte, the microstructure and chemical composition of the SEI were investigated. First, the surface structure of these three samples (Sn0.1, Sn0.2 and Sn0.4) after cycling were characterized by SEM. As shown in Fig. 4.14 (a) and (b), both Sn0.1 and Sn0.2 show a smooth and dense surface. To the contrary, as shown in Fig. 4.14 (c), Sn0.4 has a porous and uneven surface. Therefore, the electrolyte can freely transfer across the SEI, and is decomposed at the corresponding voltage (see chapter 3.1).

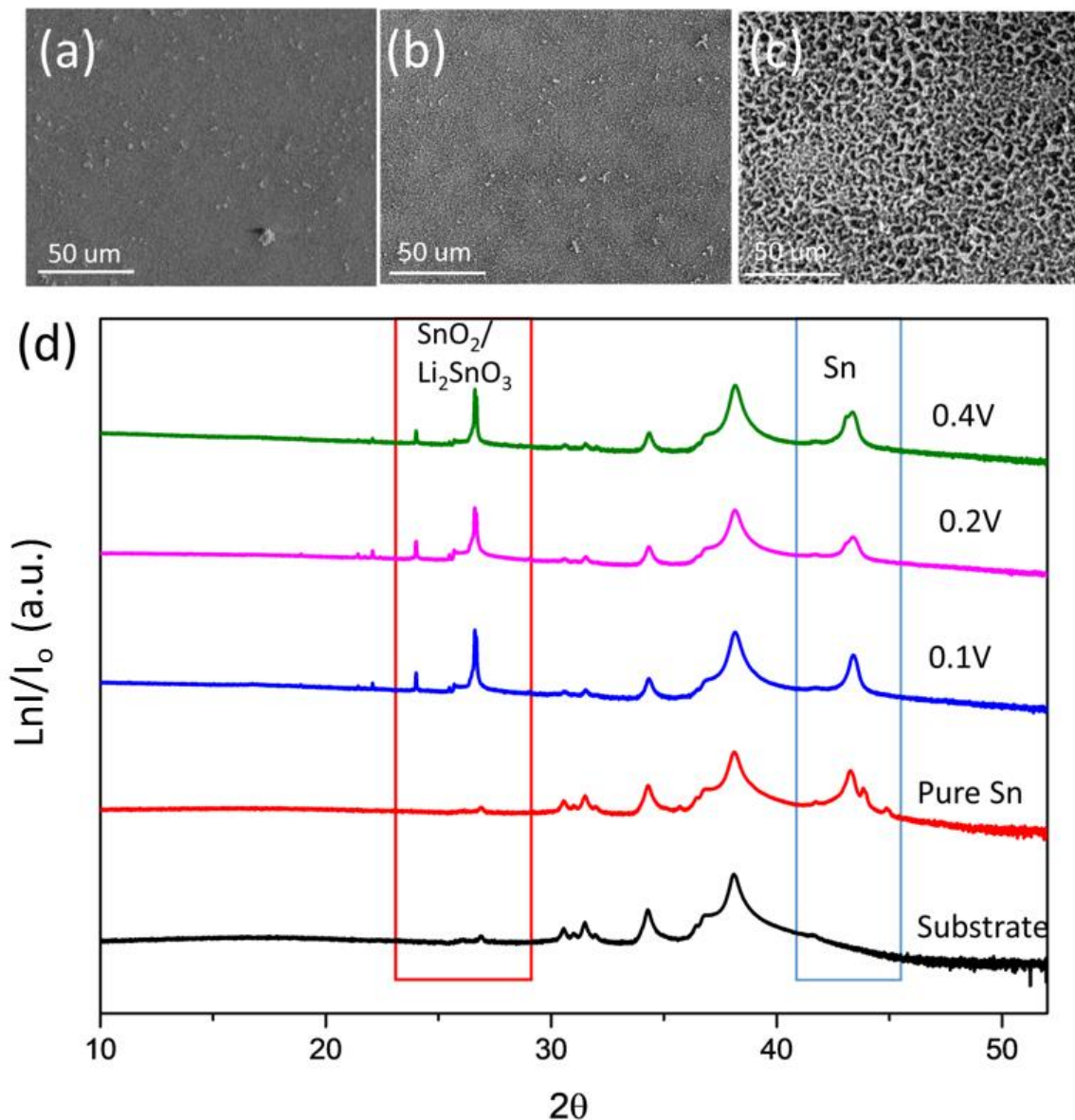


Figure 4.14: SEM images of (a) Sn0.1, (b) Sn0.2, (c) Sn0.4 and (d) XRD pattern of substrate, bare Sn and electrodes after respectively cycling down to 0.1 V, 0.2 V or 0.4 V.

Furthermore, XRD was performed to study the crystal structure of the electrode after cycling. As shown in Fig 4.14 (d), after 100 cycle, there is no signal of Sn (43.8° and 44.9°) in all of three samples (Sn0.1, Sn0.2 and Sn0.4), which demonstrate that most of Sn was consumed and remaining Sn escapes the sensitivity of XRD. Disappearance of the Sn signal and appearance of a

new peak at 26.6° just represents the reaction of Sn to SnO_2 (100) or Li_2SnO_3 (112). After cycling, to different lower voltage boundary, there is no obvious difference in the crystal structure of these three samples. Maybe the reason for the SEI on Sn0.4 being porous is attributed to the amorphous structure.

To clarify even delicate chemical variations, XPS of surface and volume of Sn0.1 and Sn0.4 were taken as shown in Fig. 4.15, respectively. The Li peak is shown in the first column, Fig 4.15 (a) - (d), the oxygen in the second, Fig 4.15 (a') - (d'), and the tin peak in the third row, Fig 4.15 (a'') - (d''). For the lithium signal, both the surface and volume of SEI formed on Sn0.1 and Sn0.4 have a Li-Li signal (around 54.6 eV) caused by incomplete delithiation. However, Li_2O is only found in the volume of Sn0.1 (see Fig 4.15 (c)), which is further proved by the signal of O 1s shown in Fig. 4.15 (c'). Besides, for the oxygen signal, as shown in Fig 4.15 (b') and (d'), the signal at 528.8 eV assigned to the organic species (RO-Li, blue) was only observed on Sn0.4 (both inside and surface). Thus, without the formation of later inorganic SEI (forming at voltage range of 0.36 - 0.27 V), the final SEI is an organic-rich layer. It is well accepted that inorganic SEI has better protective property than that of organic SEI. Consequently, there is a linear growth of SEI on Sn0.4 (as shown in Fig 4.13 (d)). In addition, for the Sn signal shown in Fig. 4.15 (a'') - (d''), there is no signal of pure Sn on both surfaces, but significant portion of pure Sn remains in the volume after 100 cycles of Sn0.1 and Sn0.4, as well. Although, the porous predominantly organic SEI in the case of Sn0.4 cannot well protect the electrode, the smaller volume expansion and thus less cracking due to only shallow lithiation, may prevent Sn from almost fully transforming into Sn oxide, even in the case of Sn0.4, too.

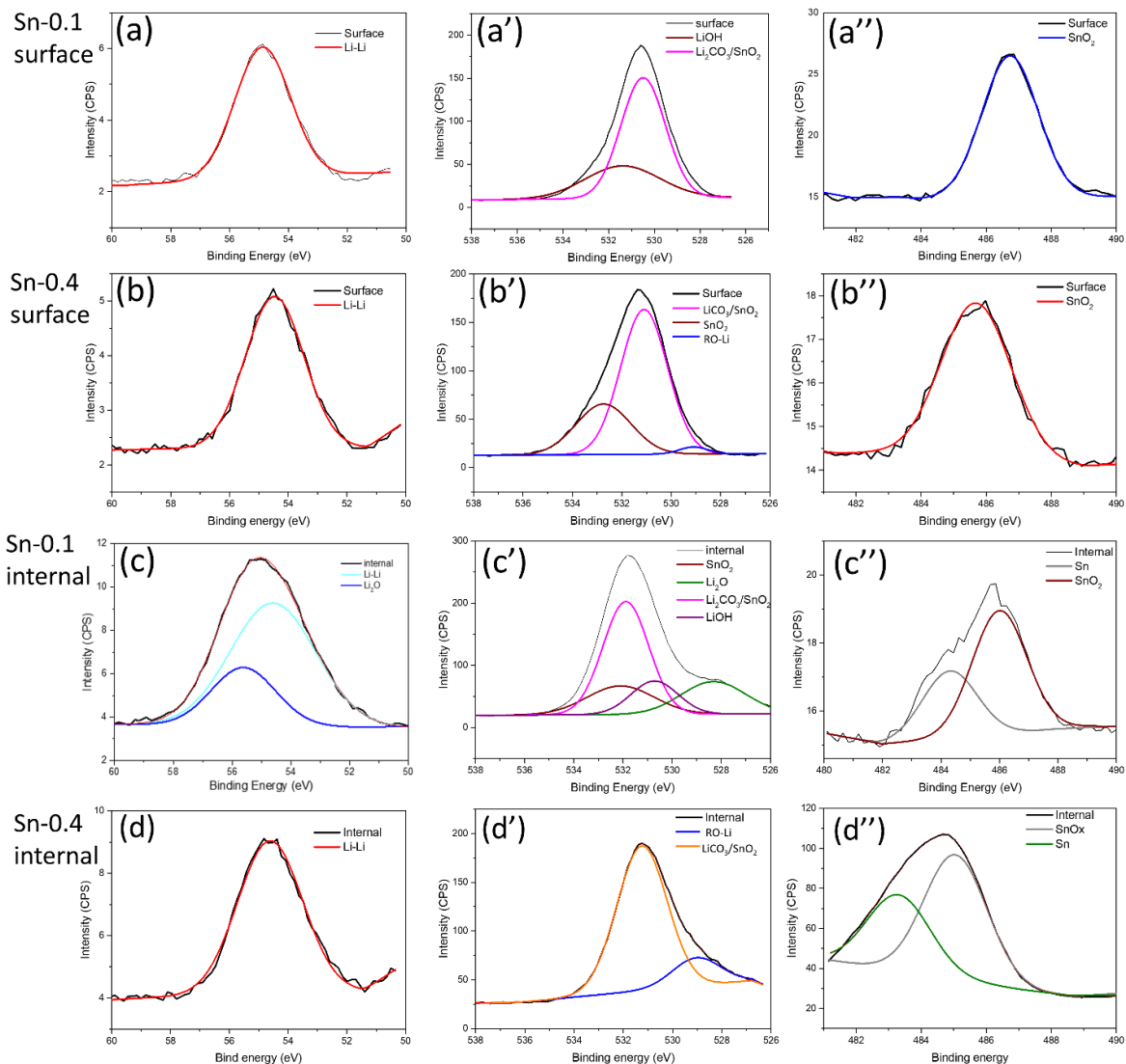


Figure 4.15: XPS data of the Sn anode after 100 cycles of- first raw. (a) - (a'') the surface on Sn-0.1, second raw (b) - (b'') the surface on Sn0.4, third raw (c) - (c'') the volume in Sn-0.1 and last raw(d) - (d'') the volume in Sn-0.4. First column (a) - (d) show the binding energy around the lithium 1s peak; middle column (a') - (d') the binding energy around oxygen 1s peak; last column (a'') - (d'') the binding energy close to tin 3d peak.

4.6 Conclusion

Quartz crystal microbalance (QCM) and Cyclic Voltammetry (CV) were combined to investigate the impact of Sn thickness and potential window of electrochemical cycling on the SEI formation during battery cycling of a Sn anode. Mass change per charge was calculated by combining the results of CV (change of charge) and QCM (change of mass), which allows do distinguish different stages of SEI formation. Results were further corroborated by XPS and XRD data. In addition, the microstructure of SEI was investigated by SEM and TEM, which provides a systematic understanding of SEI formation with Sn electrodes.

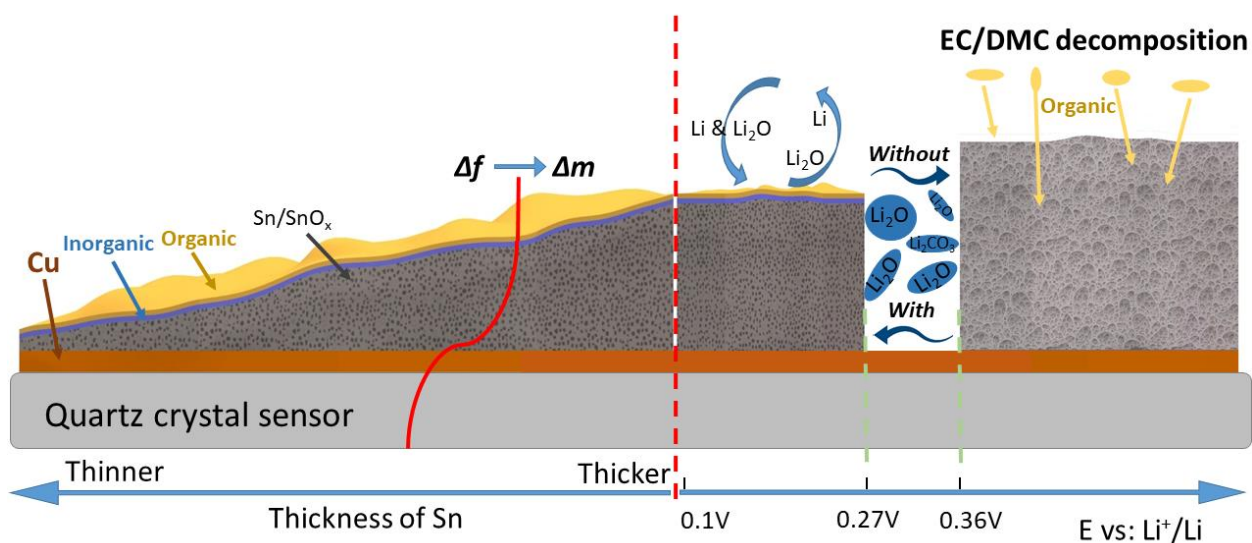


Figure 4.16: Schematic of SEI formation and cycling behavior on Sn

As illustrated in the schematic (Fig. 4.16), it was found that:

1. There is a linear relation between electrode thickness and SEI thickness probably attributed to the intensive Sn cracking and major oxidation of the Sn. Moreover, a critical

fragment size (X_o) is determined at 20 – 30 nm that describes that SEI formation is first dominated by cracking ($X_{sn} > X_o$), later slow dominated by diffusional growth.

2. The calculation of SEI density via combining the results of QCM and TEM is an efficient method to indicate the composition of SEI. Very thin electrode films promote the organic fraction of the SEI.
3. Besides being a viable part of the SEI, Li_2O contributes to reversible charge storage. This study has demonstrated that the relative amount of reversible Li_2O is related to the Sn anode thickness. Specifically, the amount of reversible Li_2O increases with the electrode thickness, which is probably controlled by the larger over-potential required for lithiation of thicker films (it will be further discussed in the next section).
4. The formation of the inorganic SEI is a thickness- and potential-dependent process. This inorganic SEI consisting of Li_2O and Li_2CO_3 plays the most important role in stabilizing the electrode against further corrosion. Without it, the electrolyte continuously decomposes with the consequence of continued linear SEI growth. As a consequence, the electrode is fully transformed into a porous layer.

5 Quantitative investigation of the reversible Li₂O formation on Germanium anodes using time-resolved microgravimetry

The Group IV elements, such as silicon, germanium and tin have attracted considerable attention in recent years, because of their high theoretical capacity (3850 mAh g⁻¹ for Si, 1570 mAh g⁻¹ for Ge, and 990 mAh g⁻¹ for Sn) and low working voltages^{22,115}. In our previous work, we have found that Li as well as Li₂O can act as a reversible species during the cycling of Si, and Li₂O formation is governed by the field across the SEI layer which is controlled by the balance between the Butler-Volmer overpotential at surface to the liquid and the diffusional overpotential driving the ion transport in the electrode volume)⁹¹. Furthermore, in chapter 3 and chapter 4, although the microstructure of Sn electrode after 100 cycles is quite complex, we still found the reversible Li₂O formed on the surface of Sn. Due to the complexity of the microstructure of Sn electrode after stability (stage IV), it is impossible to quantitatively investigate the formation of reversible Li₂O. Therefore, other electrodes having the same lithium storage mechanism need to be investigated for further understanding the formation of reversible Li₂O.

Germanium (Ge) has been gaining recent attention as a promising candidate for the next-generation of lithium-ion anodes. In comparison to silicon, which is the most probable candidate to replace graphite (perhaps only partly in the form of a composite electrode of Si and graphite), Ge has faster lithiation diffusivity and higher electronic conductivity which are around 400 times and 5000 times than those of Si, respectively¹¹⁶. Thus, the goal of chapter 5 is understanding the reversible formation of Li₂O on Ge anode to improve the mechanism of reversible Li₂O formation.

5.1 The microstructure of as-deposited Ge thin film

Similar to section 4.1, the microstructure of as-deposited Ge thin film was characterized by SEM and TEM. As shown in Fig. 5.1 (a) and (b), the sputtered Ge thin film has a smooth surface. Different to previous work on Sn, this uniform growth mode is probably due to the high recrystallization temperature of Ge. Furthermore, as shown in Fig 5.1 (b) the Ge layer appears to be amorphous without any crystallographic features like grains or grain boundaries.

5.2 100 nm thick Ge film cycled between 0.1 V - 1.5V vs Li/Li⁺ at 0.5mV/s

Firstly, the electrochemical performance of a 100 nm Ge thin film anode was characterized by CV measurement (shown in Fig. 5.1 (c)) cycled at a scan rate of 0.5 mV/s in a potential window of 0.1-1.5 V, where the 1st, 21st, 41st, 61st and 81st cycle were selected to represent different stages of the battery “life”. At the initial stage (1st cycle), similar with others works, the lithiation occurs below 0.58 V, while the delithiation peak is centered at 0.66 V¹¹⁷. However, it is remarkable and strange that with the cycles going on, the peak of delithiation shifts chaotically. This could be due to cracking which would change the conductive pathways and hence the overpotential for driving the reaction. And as shown in Fig. 5.1 (d), as the cycle number increases, the capacity continuously increases until a cliff drop at around 50th cycles. In view of the big volume expansion caused by a huge volumetric capacity (5800 mAh/cm³), the Ge anode is probably broken at around 50th cycles. Thus, the severely reduced efficiency after the 55th cycle is attributed to the fresh electrode being exposed to the electrolyte after the rupture, which leads to the decomposition of electrolyte. To visualize the rupture of Ge thin film, the SEM micrographs of

the electrode after 100 cycles was captured as shown in Fig. 5.1 (e). There are many cracks on the surface of Ge (bottom of Fig. 5.1 (d)) making many island-like structures (size of 3-6 μm are evenly distributed) on the electrode. Moreover, the internal microstructure of the unbroken parts (marked by red rectangular area) was investigated by the TEM cross section. As shown in Fig. 5.1 (f), the thin film electrode has completely pulverized and is intermixed with the SEI. Considering that the thickness of Ge and the SEI combined is $157 \pm 12\text{nm}$ and the thickness of Ge has been 100 nm before cycling, the thickness of SEI is roughly $57 \pm 12\text{ nm}$. Compared with that of Sn (around 700 nm SEI on 100 nm shown in Fig. 3.4), after cycling, the SEI of GE is quite thin even though Ge is largely fragmented.

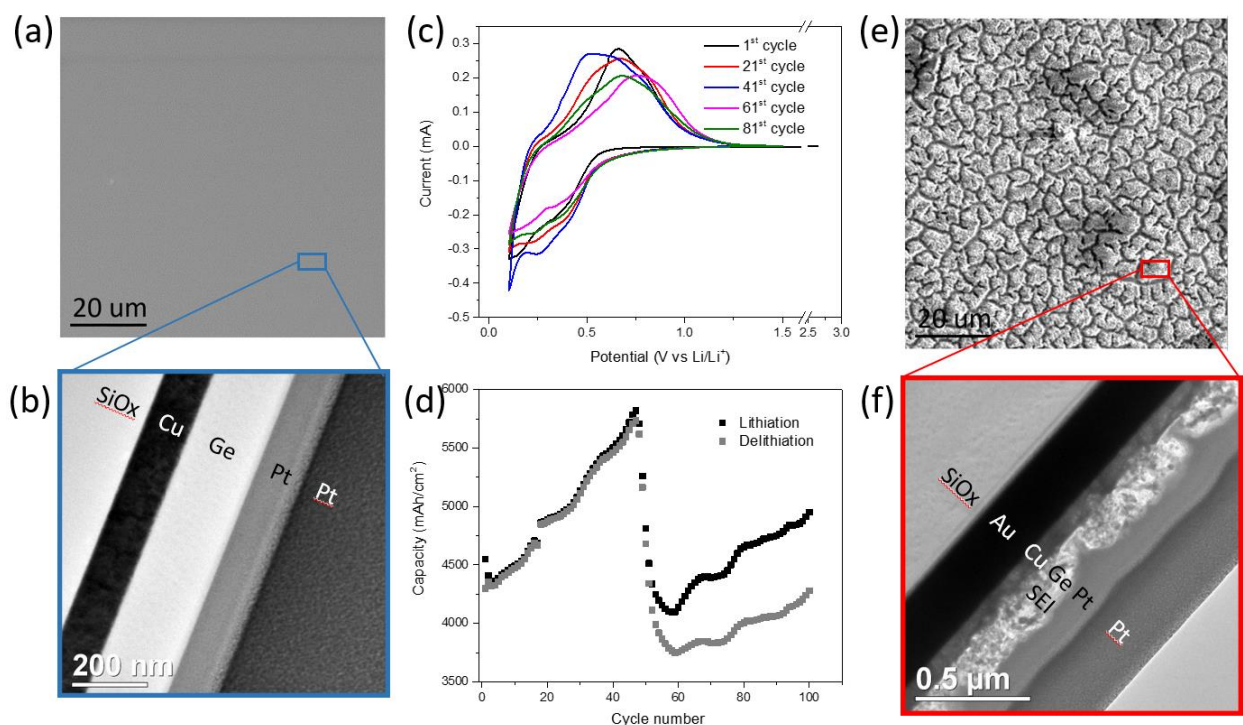
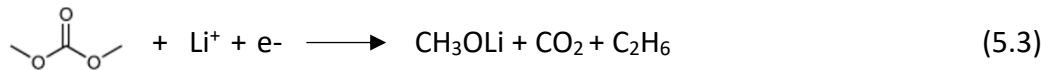
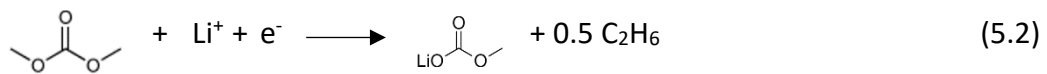
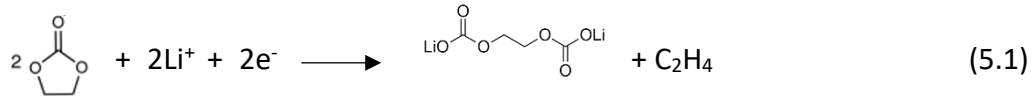


Figure 5.1: The (a) SEM image and (b) TEM cross section micrograph of 100 nm Ge electrode; (c) the CV curve and (d) electrochemical capacity of a 100 nm Ge film at a scan rate of 0.5 mV/s in the potential window of 0.1 - 1.5 V; (e) the SEM image and (f) TEM cross section micrograph of 100 nm Ge electrode after 100 cycles.

Following, besides the electrochemical testing, the SEI formation and cycling behavior on Ge anode was firstly investigated by the QCM mass change of this Ge layer as shown in Fig. 5.2 (a). The similarly as discussed in chapter 3 and 4, the trend line of mass change indicates the irreversible mass deposition, which can probably be attributed to the SEI formation, while the characteristic periodic oscillations, shown in the inset of Fig. 5.2 (a), represent the reversible process of lithiation and delithiation. Quantitatively, the big irreversible mass change (2.69 μg , or specifically 8.107 $\mu\text{g}/\text{cm}^2$) of the first cycle is attributed to the initial SEI formation derived from the decomposition of the electrolyte. To investigate the species involved in the SEI formation process, the MPE-based curves were analyzed as shown in Fig.5.2 (b) and (c). At the initial stage of the first cycle (1.4 – 0.8 V), the MPE value of 81 g/mol (yellow line) is well agreement with that of the decomposition products of solvents shown in equation (5.1) and (5.2) ⁹²(C₄H₄O₆Li₂: MPE = 81 g/mol from EC reduction, C₂H₃O₃Li: MPE = 82 g/mol from DMC reduction). The MPE value of 69.9 g/mol (green line) should be attributed to an average of decomposition products of DMC since they are happening simultaneously i.e. C₂H₃O₃Li (82 g/mol) and CH₃OLi (MPE = 38 g/mol see equation (5.3)).

Then, in the potential range of 0.48 – 0.41 V, the MPE value of 11.5 g/mol (black line) may indicate the formation of inorganic species, like Li₂O (14.9 g/mol) LiOH (23.9 g/mol) or Li₂CO₃ (36.9 g/mol), although the observed 11.5 g/mol is smaller than any MPE of them. In view of the fact that the onset of lithiation in Ge appears already at 0.5 V, the shift to smaller mass is probably due to the simultaneous insertion of Li (MPE = 6.9 g/mol). Finally, the MPE value decreases to 7 g/mol (blue solid line) which demonstrates exclusive lithiation of Ge. As shown in Fig. 5.2 (a), after the initial SEI formation, the trendline become stable until a rapid increase sets in at around the 45th cycle

(after red dashed line in Fig. 5.2 (a)). As reported in previous work⁹¹, such sharp increase is probably attributed to the sudden electrode cracking (derived from the volume expansion) which leads to the continuous decomposition of the electrolyte and formation of new SEI. This cracked surface and the consequent microstructure can be clearly seen after 100 cycles by the SEM and TEM images as shown in Fig. 5.1 (d) and (f).



The cycling behavior of the electrode after rupture is too complex for a detailed QCM analysis. Thus, in the next part, we will focus on the investigation of the stable stage (from 1st cycle to 43th cycle). Fig. 5.2 (d) shows the MPE mass spectrum collected from 1st to 40th cycle. There are two peaks located at 7 g/mol and -6.5 g/mol representing the lithiation and delithiation, respectively. Strikingly, both of these two peaks have a tail ranging from 10 g/mol to 20 g/mol (positive and negative value represents mass loaded and uploaded, respectively). This kind of small tail could be attributed to the formation and decomposition of reversible Li₂O as suggested in previous work on Si. In order to prove this assumption and locate the voltage range of Li₂O forming, the MPE based curves of the 10th cycle are shown in Fig. 5.2 (e) and (f), respectively. In particular the integrated MPE, which suppresses the noise, clearly indicates beside the expected mass of Li the additional mass changes of 15.4 g/mol (lithiation half cycle) and 15.1 g/mol (delithiation half cycle) which closely matches to the mass per elementary charge of Li₂O. Similar to the observation at Si, the Li₂O is formed and decomposed before lithiation and delithiation, respectively, in the

potential ranges of 1.15V - 0.56 V (cathodic scan, lithiation) and of 0.28-0.42 V (anodic scan, delithiation).

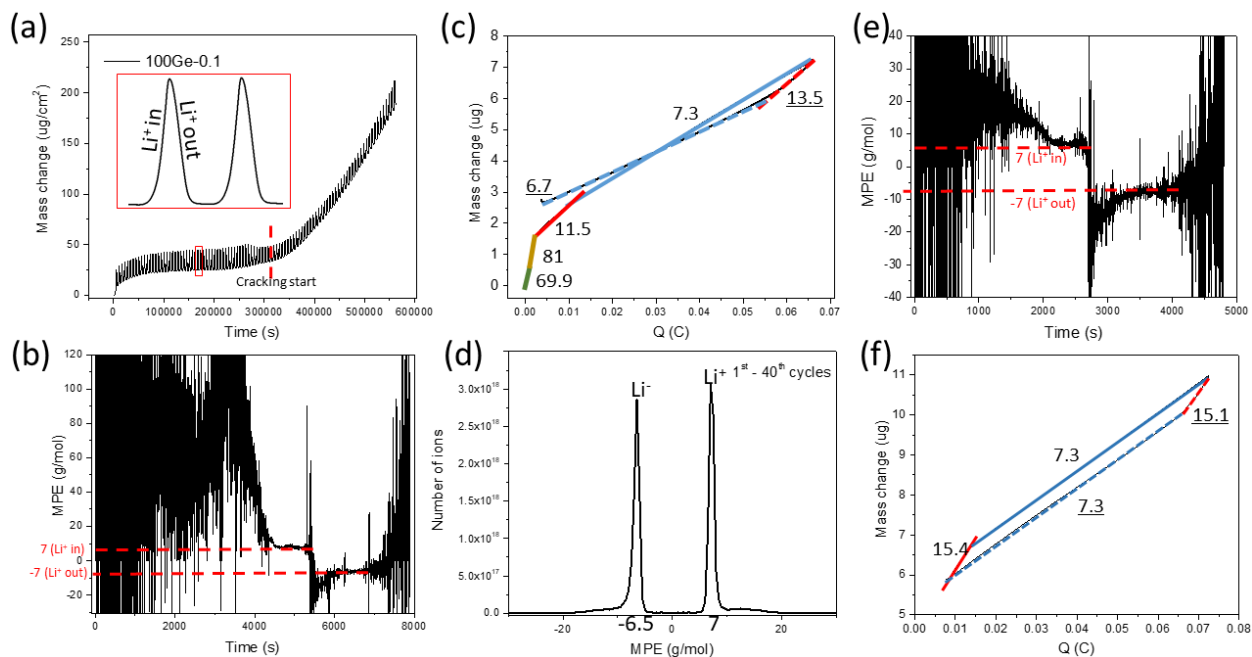


Figure 5.2: (a) The mass change of a 100 nm Ge cycled between 0.1 and 1.5 V as measured by QCM, (b) the real-time MPE and (c) the integrated MPE of the 1st cycle, (d) the mass spectrum obtained between the 1st to 40th cycles, (e) the real-time MPE curve and (f) the integrated MPE curve of the 10th cycle.

To further prove that the reversible species is Li₂O, the ex-situ XPS measurements of 100 nm Ge cycled to different voltage cut-off (Sample 1: one complete cycle and subsequent lithiation to 0.45 V vs Li/Li⁺ and sample 2: one complete cycle). Thus, the extra signal of sample 1 is mostly derived from the reversible species deposited through 1.5 V and 0.45 V. As shown in Fig. 5.3 (b) and (c), the Li₂O signals at 55.1 eV (Li 1s) and 528.3 eV (O 1s) confirm that the reversible species is Li₂O. Furthermore, the signal of Ge²⁺ and Ge⁴⁺ shown in Fig. 5.3 (d) and (d') is probably due to the oxide termination of the Ge thin film¹¹⁸.

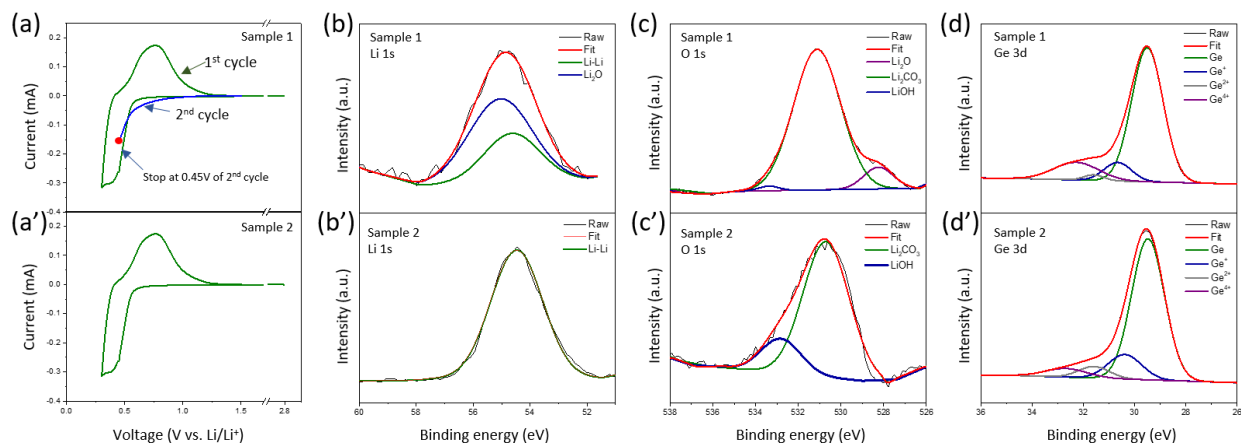


Figure 5.3: CV curve of 100 nm Ge thin film: sample 1 (a) one complete cycle and subsequently lithiated to 0.45V vs Li/Li⁺; sample 2 (a') one complete cycle and stop at voltage of 1.5 V vs Li/Li⁺; XPS data of sample 1 ((b'), (c') and (d')) and sample 2 ((b), (c) and (d)). (b) and (b') shows the binding energy around the lithium 1s peak; (c) and (c') show the binding energy around oxygen 1s peak; (d) and (d') show the binding energy close to the binding energy to Ge 3d peak.

5.3 100 nm thick Ge film cycled between 0.3 V – 1.5 V vs Li/Li⁺ at

0.5mV/s

It is well established that reducing the amount of inserted lithium is an effective way to reduce the volume expansion of electrode. Thus, the working potential window was shortened to 0.3 - 1.5 V. As shown in Fig. 5.4 (a), in direct comparison to previous experiment, after reducing the potential window, the amplitude of the QCM oscillations decreases, while the irreversible mass change becomes more stable (only a tiny increase in the last five cycles) pointing out significantly less cracking for the smaller voltage window. As shown in Fig. 5.4 (b), the SEM micrograph reveals many local ruptures instead of the completely damaged surface that was observed previously. Furthermore, the microstructure of electrode (marked by red cycled area) was investigated by analyzing a cross section of the electrode using a TEM and shown in Fig. 5.4 (c). After 100 cycles,

the Ge thin film is well intact and the SEI formation happened only on the surface and it does not destroy the morphology of the electrode. The formed SEI appears to be non-uniform. The thinner part shown in the red rectangular is shown at a higher magnification in Fig. 5.4 (d). As can be seen in Fig. 5.4 (d), the thickness of the unbroken SEI amounts to 15.2 ± 2.42 nm.

In order to explore the cycling behavior (reversible reactions) of the Ge anodes and to find out what causes the Ge anode's gradual cracking, as shown in Fig. 5.4 (e) and (f), the amplitudes of the QCM oscillations (black curve) were strictly calculated by using the ending mass of each half cycle minus its starting mass, while the CV mass oscillations (green curve) were calculated from the processed charge under the assumption that only Li ions are reversibly processed. The CV mass curves were corrected (not shown here) using equation 2.7 - 2.9 (seen in section 2.4.4) to accommodate for reversible Li₂O processing. Ideally for only lithium insertion, the ratio between these two curves i.e. the QCM and CV mass curves (blue curve) should be one. However, the continuous variation of the ratio QCM ampl. / CV ampl. shows that the proportion of reversibly processed Li and Li₂O is varying with cycle number. This could be either due to the variation in the amount of Li₂O formed or in the amount of inserted Li (or both). Based on Fig. 5.4 (e) and (f), the amount of reversible Li₂O for the samples processed in the two different voltage windows were calculated as shown in Fig. 5.4 (g). It can be seen that the amount of reversible Li₂O on both samples decreases during longer cycling. However, in the case of the larger voltage window (1.5 V - 0.1 V) with significantly stronger cracking, the decrease in the amount of Li₂O formation/removal is much faster. This will be further discussed in the subsequent sections.

As discussed above (Fig. 5.2 (c) and (d)), Li₂O is significantly formed in the voltage range of 1.15 - 0.56 V which is within the working potential windows of both of the presented two samples

(having same thickness). Consequently, as shown in Fig. 5.4 (h), the amount of Li₂O is almost the same, and the different working potential windows of these two samples only makes a difference to the absolute amount of inserted Li.

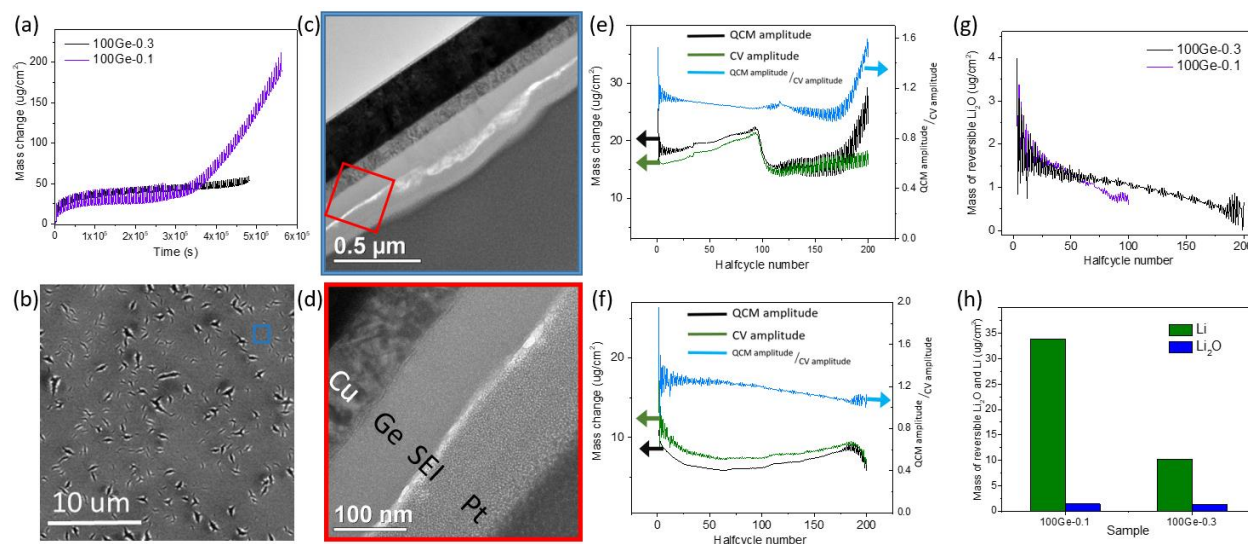


Figure 5.4: (a) The mass change of 100Ge-0.1 (black) and 100Ge-0.3 (purple); (b) the SEM of the surface of 100Ge-0.3; (c) Less magnified TEM image of the cross section of 100Ge-0.3; (d) higher magnified TEM image of the area highlighted in red in subfigure (c); The amplitude of the reversible QCM mass change (black), the CV mass change (green) and the ratio between both (blue, note different y-axes) in the case of (e) 100Ge-0.1 and (f) 100Ge-0.3, (g) the mass of reversibly processed Li₂O on 100Ge-0.1 as a function of the half cycle number, (h) the amount of reversibly processed Li and Li₂O at the 10th cycle of 100Ge-0.1 and 100Ge-0.3.

5.4 20 nm thick Ge film cycled between 0.3 V – 1.5 V vs Li/Li⁺ at

0.5mV/s

To further stabilize the electrode against cracking and to study the effect of film thickness, the thickness of the Ge thin film was reduced to 20nm. As shown in Fig. 5.5 (a), different to 100Ge-0.3, except the capacity fade in the initial cycles, 20Ge-0.3 exhibit a highly stable capacity of 3750

mAh/cm³, and the coulombic efficiency after 100 cycles is way above 90%. As shown in Fig. 5.5 (b), the mass change in 20Ge-0.3 definitely shows an irreversible increase especially in the beginning which is naturally attributed to SEI mass. In the subsequent cycles however, the QCM data of 20Ge-0.3 show a slowly growing trendline. The total irreversible mass change after 100 cycles is 8.38 μg. Fig. 5.5 (c) shows the SEM image of the surface after 100 cycles and Fig. 5.5 (d) the TEM cross section micrograph. Both images prove that there is no cracking in case of the 20 nm Ge film. The SEI thickness on 20Ge-0.3 amounts to 21.5 ± 7.55 nm. As shown in Fig. 5.5 (e), the stable amplitudes of the periodic oscillations of QCM and CV mass demonstrate that all reactions occurring after initial SEI formation are mostly reversible. Motivated by the previous, comparing QCM and CV mass amplitude, quantitatively, the relative contribution of reversible Li₂O amounts to 4%. Remarkably no variation is seen over 100 cycles, which leads us to the conclusion that the above observed variation of Li₂O proportion for sample cycled down to 0.1 V can be safely attributed to irregular cracking of Ge thin film. Furthermore, significantly more reversible Li₂O, is observed for the thicker films. The dependency of the reversible Li₂O on thickness of Ge is presented in Fig. 5.5 (f), the amount of Li₂O increase by factors when increasing the Ge thickness from 20 nm to 100 nm. Similarly, the amount of Li, however, it should be noted that unlike Li₂O, the absolute amount of Li alloying is expected to vary proportional to the bulk volume. The real behavior is however under proportional probably as a consequence of limited transport kinetics under fast assuming.

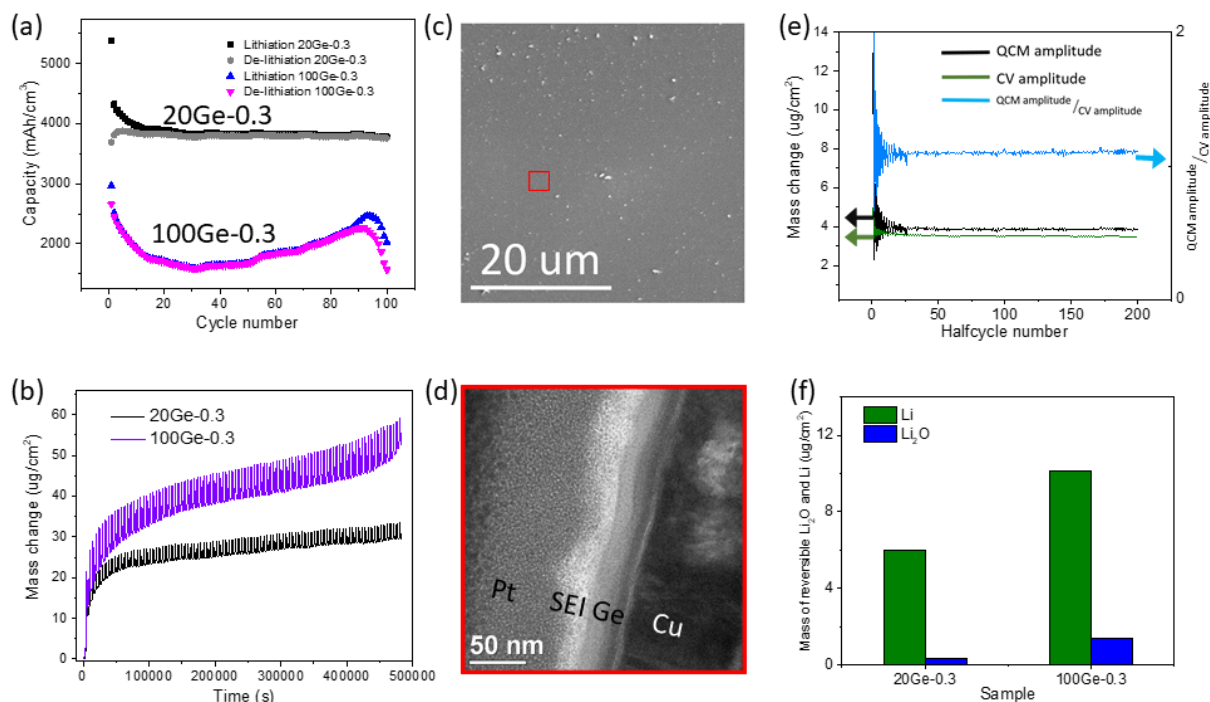


Figure 5.5: The cycling capacity (a) and mass change (b) of 20Ge-0.3 and 100Ge-0.3, the SEM surface image (c) and TEM cross section (d) of 20Ge-0.3 after cycling, (e) The amplitude of the QCM mass change (black), the CV mass (green) change and the ratio between both (blue) for the 20 nm Ge and (f) the amount of Li and Li₂O at the 20th cycle of 20Ge-0.3 and 100Ge-0.3.

5.5 20 nm thick Ge film cycled between 0.3 V – 1.5 V vs Li/Li⁺ at different scan rates (from 0.125mV/s to 16mV/s)

Finally, we would like to clarify the effect of the scanning rate on the electrochemical cycle behavior of the Ge anode. As shown in Fig. 5.6 (a), a 20 nm Ge was cycled at different scan rates in the fixed potential window of 0.3 - 1.5 V. The Ge anode exhibits similar redox behavior at the different scan rates. However, according to the Butler-Volmer equation, the over potential to drive the ions into the electrode increases with the current density. Thus, with the increasing scan rate, the de-lithiation peak shifts systematically towards higher voltage. Correspondingly,

the mass change reduce which can be seen in Fig. 5.6 (b). The same is also documented by the increase of capacity of the films for slower scanning as shown in Fig. 5.6 (c). Furthermore, the ratio of Li₂O/Li as a function of scan rate is determined, see Fig. 5.6 (d) whereas Figure 5.6 (e) shows the absolute amount of reversibly processed Li and LiO_{0.5} at different scan rates. The amount of alloyed Li decreases when increasing the scan rate, while the reversible LiO_{0.5} remains almost constant (decreases very slightly). As shown in Fig. 5.6 (f), the faster the scan rate of the anode, the lower is the potential at which the Li₂O formation is totally changed to lithiation, which is in a good agreement with the observation that the over potential of lithiation increases as the increase of scan rate.

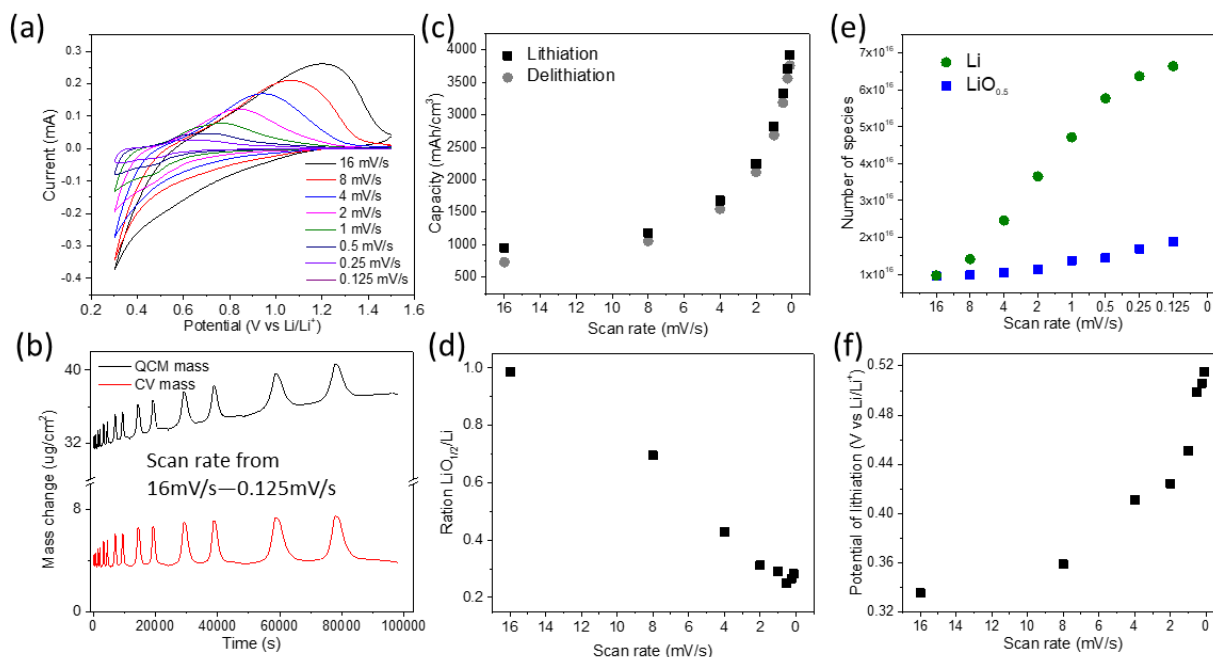


Figure 5.6: (a) The CV curves, (b) the mass change curve, (c) the cycle capacity and (d) the ratio of LiO_{0.5}/Li, (e) the absolute amounts of Li and LiO_{0.5} of 20Ge-0.3 cycled at different scan rates, (f) the position of delithiation peak.

5.6 Li₂O formation mechanism: Silicon vs Germanium

After the detailed investigation on the reversible Li₂O formation on Ge, it is naturally suggested to compare with the behavior of the chemically similar Si electrodes (see Fig. 5.7 (a)-(c)). Remarkably 20 nm silicon shows a significantly larger (almost double) amount of reversible Li₂O than that on 20 nm Ge.

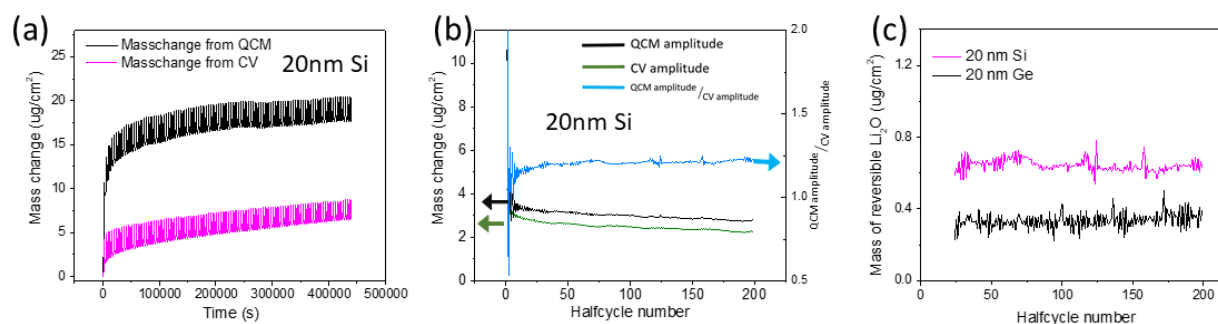


Figure 5.7: (a) Mass change from CV and QCM of 20 nm Si at a scan rate of 0.5 mV/s in the potential window of 0.1 - 1.5 V⁹¹, (b) The amplitude of the QCM mass change (black), of CV mass (green) change and the ratio between QCM amplitude and CV amplitude (blue) of 20 nm Si, (c) the amount of reversibly cycle Li₂O on 20 nm Si and 20 nm Ge.

We assumed that the Li₂O formation is the reaction at the electrode surface derived by the reduction of the electrolyte (same with the formation of SEI) and both Ge and Si do not take active part in this process⁹¹. Thus, we expect the reversible formation of an oxide layer between the anode and the irreversible SEI. In view that electrons are needed to reduce the electrolyte and so to form Li₂O, the maximum thickness of the oxide is postulated to be controlled by the maximum voltage drop, respectively the field across the Li₂O layer which is driving the electron flux.

As shown in Fig 5.8 (a), the voltage drop across the oxide is established as balance between the Butler-Volmer overpotential at the surface to the liquid (increase with the scan rate) and the diffusional overpotential driving the ion transport in the electrode volume.

Nevertheless, the difference in the amount of Li₂O must be attributed to the different properties of the electrode material. Notably, in our prior study⁹¹, we neglected the electronic part of the over-potential. As shown in Table.5.1, silicon has definitely a way lower ionic than electronic conductivity. Thus, slow ionic migration controls the necessary transport over-potential inside the electrode, which has been investigated in other electrodes via appropriate models^{119,120}.

Table 5.1: Parameter comparison of Si and Ge^{121–124}

Anode	Voltage vs Li/Li ⁺ (V) for X ₁ Li ₁	Diffusion coefficient (cm ² /s) at RT	Ionic conductivity (from Diffusion coefficient) (S/cm)	Intrinsic electronic resistivity (Ohm-cm)
Ge	0.55	6.14×10 ⁻¹²	1.84*10 ⁻⁶	47
Si	0.4	3 × 10 ⁻¹⁴	1.01×10 ⁻⁸	2.3×10 ⁵

Moreover, as shown in table.5.1, Ge also has roughly 400 times higher ionic diffusivity (responsible for diffusional overpotential) than silicon¹¹⁶. Thus, as shown in Fig. 5.8 (a) (purple dotted line and blue short-dashed line for Si and Ge, respectively), at the same lithiation rate, the field or voltage drop across the Li₂O layer is significantly higher in the case of Si than in case of Ge. Therefore, for the same thickness and scan rate, Si is naturally expected to show the larger amount of Li₂O formation, which matches very well to our experiments (shown in Fig. 5.7 (b)). It should be clarified that here we ignore the difference in thermodynamic properties of Ge and Si. We will discuss the effect of thermodynamic property in fellow section.

Furthermore, as illustrated in Fig. 5.8 (a) (green long-dashed line), the thicker the sample is, the higher is the required diffusional over-potential, which promotes the formation of Li₂O (more Li₂O formed at thicker than thinner samples). Moreover, it is clear that the volume expansion derived by the insertion of excessive Li induces many cracks. After cracking, the length of the migration pathways for lithium is reduced, which can be considered as the same effect as reducing the thickness of the electrode. Thus, an electrode with more cracks shows less Li₂O formation attributed to the reduction of the diffusional over-potential which well match the stronger decrease of Li₂O formation in case of 100Ge-0.1 (high cracking) compared to 100Ge-0.3 (low cracking) (see Fig. 5.4 (g)).

Next, the Butler-Volmer (B.V.) interfacial potential need to be discussed to understand the scan rate dependence. It has a negative effect on the total potential drop across the Li₂O. Meaning, the increase of scanning rate slightly decreases the amount of Li₂O (shown in Fig. 5.6 (e)). Obviously, the increase of the B.V. overpotential slightly overcompensates the increase of the diffusional over-potential (red dot-dashed line and in Fig. 8 (a)).

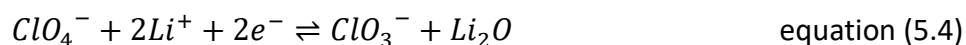
Finally, the thermodynamic effects, the different onset voltage of lithiation (for the first intermetallic phase Li₁X₁, where X is Si or Ge) should be taken into account, which are 0.5 and 0.4 V vs Li/Li⁺ for Ge and Si, respectively. As shown in Fig. 5.8 (b), if the applied voltage (black solid line) is below the equilibrium lithiation potential, the lithium will start alloying into the electrode. This happens in germanium sooner than in silicon. In other words, in the case of Si, due to the lower onset voltage (0.4 V) for lithiation, the voltage range for exclusive Li₂O formation is wider than for Ge. Therefore, from the thermodynamic view, cycling of Si should produces more Li₂O than Ge. However, after calculating the diffusion over-potentials from the ionic conductivities

Lithiation is already possible in case of Ge, whereas in the case of Si, only Li₂O formation can take place. (c) Schematic representation of the lithiation voltage in a general electrode. As the thickness of Li₂O layer increases (Δx_{Li_2O}) the net field i.e. gradient in potential decreases thereby decelerating the growth of Li₂O. Whereas in (d), the opposite case can be seen during delithiation that, once the voltage drop is established the field responsible for the dissolution only increases as the thickness of Li₂O is reduced until it vanishes. In (c) and (d), point A is controlled by the equilibrium voltage or OCV (in accordance to Poisson's equation for the formation of electrical double layer, B is controlled by the B.V. overpotential, C is controlled by the applied voltage, and D is the OCV/equilibrium voltage.

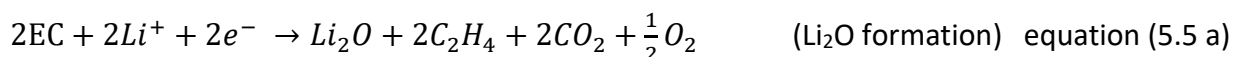
Until now, we only have discussed the formation of Li₂O but not thought about the decomposition of Li₂O on the electrode's surface during the delithiation half cycle. First, let us discuss the process of Li₂O formation/decomposition. In view that the evolution of Li from LiClO₄ to Li₂O make no charge transfer, the charge transfers to understand the controls by electrochemical process must be derived from the decomposition of electrolyte.

From the presented experiments, the chemical reactions leading to the formation of Li₂O remain unclear (charge transfer derived from lithium salt or solvent). But presently, we may consider the following possible reactions:

- (i) Li₂O formation/dissolution assisted by the decomposition of anions of the lithium salt



- (ii) Or decomposition of the solvent:





Next, let us discuss the mechanism for the decomposition of Li₂O during the delithiation, the arguments of lithiation step should also hold true during the delithiation. Fig. 5.8 (c) shows the postulated mechanism for the formation Li₂O during lithiation (as discussed above). Specifically, At the beginning of the cycle all potential points A, B, C, and D are at the same level (assume the open circuit voltage). The points A and D should proportionally vary due the electrical double layer formation in accordance to the Poisons-Boltzmann equation¹²⁵. First, the applied voltage (C) is lowered to drive ions into the electrode. As a consequence of the developing flux, point B is lowered by the B.V. drop with a certain retardation. As soon as a negative voltage gradient is present across the oxide, electrons will flow towards the electrolyte side, where they induce fresh oxide (e.g. according to Eqs. 5.4 or 5.5a, see below). In this case, the growing Li₂O layer (Δx_{Li_2O} in Fig. 8(c)) decreases the gradient and hence the growth of the oxide is decelerated in time (self-limiting reaction). During delithiation, as illustrated in fig. 8(d), again we start at the equilibrium voltage of the charged electrode but now we have to elevate the voltage. So, at the anode, with the same arguments, a voltage gradient is established in opposite direction, driving electrons into the electrode and thus dissolving the oxide at the surface (as per eq. 5.4 or 5.5b). However, in this case shrinkage of the oxide even increases the gradient and thus also the current, explaining why dissolution of the oxide is fast and can be almost completed before major delithiation sets in.

5.7 Conclusion

In this section, quartz crystal microbalance and cyclic voltammetry were combined to quantitatively investigate the SEI formation and cycling behavior on Ge anodes. Li_2O was identified as an additional reversible species cycled on Ge anode and further confirmed by XPS. Attributed to the over-potential of lithiation determined by kinetic properties, the amount of reversible Li_2O increases with the increasing thickness of Ge anode. Inevitably, the volume expansion determined from the insertion of excessive Li induces many cracks in the Ge anode. These ruptures decrease the amount of reversible Li_2O via shorting the pathways of Li transport (similar to a decrease of the thickness of the Ge anode). Meanwhile, the decrease on the amount of Li_2O reduces the protection ability of the SEI. Significantly, a direct comparison of the amount of Li_2O between Si and Ge shows that the formation of Li_2O and the insertion of Li are competitive reactions. The slower lithiation of Si caused by lower diffusivity in comparison to Ge, provokes a larger amount of Li_2O . In addition, the amount of reversible Li_2O also weakly depends on the different onset potentials of lithiation in both electrode materials.

6 Conclusion

This thesis innovates and utilizes new methodologies for investigating the formation of the solid electrolyte interphase and the cycling behavior of the anodes (group IV: Sn and Ge) in a lithiation ion battery. For this purpose, QCM was combined with simultaneous CV measurements. The in-situ mass change during the cycling was detected by EQCM, while the amount of charge transfer was recorded by CV measurements. After combining the results of EQCM and CV, mass per charge (MPE) was calculated which provides an opportunity to visualize the in-situ chemical composition change during the cycling. Short time interval used in this thesis of around 14 s allows detecting various species when processed separately in a timely order. The huge amount of data points attributed to the small time interval were calculated and analyzed by a MATLAB routine.

Sputtered thin film anodes (Sn and Ge) and current collector (Cu) were used which conveniently enables a quantitative control of different thicknesses. In addition, sputter deposited films have the advantage of being free from conductivity or binder additives excluding the interference with these factors. Meanwhile, without binder or conductivity additives, the spatial structure of electrode after cycles (from TEM cross section micrograph) are easier to identify.

In case of the Sn anode: Combined QCM-CV was used in a first step to investigate the SEI formation and cycling behavior on Sn anodes. For the long-term analysis of cycling, three different characteristics namely mass spectra, real-time MPE and average MPE were combined for the overall and segmented study of different stages of the battery life. Different to the cases of Si and Ge, during the delithiation half cycle, the recrystallization of Sn destroys the morphology

of SEI and meanwhile, Sn also participate directly in the formation of SEI. Therefore, attributed to the complexity of SEI formation on Sn, the whole process was divided into four stages. Stage I comprises only the first charging/discharging cycle. A layer of organic (CH_3OLi and $\text{CH}_2\text{OCO}_2\text{Li}$) and inorganic SEI (Li_2O , LiOH , and Li_2CO_3) formed before significant lithiation. Stage II ranges from the 2nd to 5th cycles. Further growth of inorganic SEI (Li_2O and more complex oxides) is detected during the lithiation particularly in the potential range of 0.36 – 0.27 V. In addition, Sn begins to become oxidized in the delithiation half cycles (above 0.92 V). The onset of stage III is marked by the 6th cycle, in which the deposition of irreversible Li_2O stops and further significant growth of the SEI is noticed only by the oxidation of Sn during the delithiation. Transition to the final stage IV is observed at about the 45th cycle. This stage presents a quite stable electrode in which SEI only grows slowly probably under diffusion control. As the second interesting aspect discovered by quantitative analysis of the processed mass, a heavier species (probably Li_2O) is demonstrated to contribute with a relative fraction of 23 % to the reversible charge storage of 100 nm thick Sn films.

Besides a four-stage formation of the SEI, the effect of sample thickness and working potential window on the SEI formation and cycling behavior of Sn anodes were investigated quantitatively. Firstly, a linear relationship was found between sample thickness (Sn) and SEI thickness, probably attributed to the cracking and oxidation of the Sn. Moreover, a critical fragment size (X_0) is determined at 20 – 30 nm that describes that SEI formation is first dominated by cracking ($X_{\text{Sn}} > X_0$). Second, based on the calculation of SEI density via combining the results of QCM and TEM, we found that very thin electrode films promote the organic fraction of the SEI. In addition to being a viable part of the SEI, Li_2O also works as reversible shuttle and provides part of the charge

storage. We found that the relative amount of this reversible Li_2O increases with the Sn thickness, an effect which is probably controlled by the larger over-potential required for lithiation of thicker films.

The major part of the inorganic SEI consisting of Li_2O and Li_2CO_3 , formed within the potential window of 0.27 - 0.36 V in stage II. It plays the most important role in stabilizing the electrode against further corrosion. Without it, the electrolyte continuously decomposes with the consequence of continued SEI growth at a constant rate. Finally, the electrode is then fully transformed into a porous layer.

Similar investigations were performed with Ge anodes: Since Ge does not participate in the formation of SEI, compared to Sn, Ge demonstrate an easier SEI forming process comprising the initial SEI formation in the first cycle and the later SEI formation dominated by diffusion. For the thicker Ge thin film anode or for cycling in wider potential window (more Li insertion), Ge undergoes cracking and consequent reformation of the SEI on the surface of the fresh anode. Besides the formation of irreversible SEI, Li_2O was also identified as a reversible species formed/removed during the lithiation/delithiation on the Ge anode which was further proved by XPS.

7 Outlook

The present thesis provides a framework to in-situ characterize the long-term SEI formation and cycling behavior of anodes at the example of Sn and Ge which could be easily extended to other anode materials such as metal oxides (Fe_2O_3), alloys (Al, Zn) and sulfides (Co_9S_8). In view of the irreversible phase transition of quartz if the temperature is above $573\text{ }^\circ\text{C}$, but most of cathodes must be annealed at temperature up to $700\text{ }^\circ\text{C}$, application of the quartz as QCM sensor is limited. Thus, some alternative piezoelectric crystals such as langasite ($\text{Ga}_5\text{La}_3\text{O}_{14}\text{Si}$) or Gallium phosphate (GaPO_4), which have higher phase transition or melting temperature may allow us to deposit the layers and perform subsequent annealings up to $900\text{ }^\circ\text{C}$. Thus, the cathode electrolyte interphase (CEI) and the release of lattice oxygen could be detected quantitatively via QCM too, if the alternative piezo-crystals could be established.

We have already tried to characterize the long-term SEI formation on the commercial graphite anodes (deposited by magnetron sputtering). However, the experiments were not successful, which the graphite thin film totally dispersed in the electrolyte after a few cycles. As reported elsewhere⁹², the co-intercalation of solvents exfoliates the graphite layers from the bulk graphite anode. The anodes used in this work are binder-free thin films, without the protection of binder, graphite is exfoliated easily. Moreover, as discussed in chapter 5.6, the SEI formed on Si and Ge could not completely prevent the charge transfer to electrolyte, otherwise there would be no formation of Li_2O . Thus, graphite or even conductive carbon could not be cycled stably in this electrolyte (1 M LiClO_4 in DMC:EC). Therefore, if the reversibly cycled Li_2O on Si or Ge wants long-term application, the conductive carbon may need to be replaced by other conductive material.

Furthermore, the reversibly cycled Li_2O appears as a quite general effect for the alloying electrodes of group IV elements (Si, Ge and Sn). The amount of Li_2O is controlled by both kinetic (the thickness of electrode and the cycling scan rate) and thermodynamic properties (the onset of lithiation). In my view, this reversibly cycled Li_2O should occur on other anodes, too if the onset of lithiation of the anode is after the formation of Li_2O . Because the formation of Li_2O and lithiation appear as two separate processes (one occurring at the interface and one taking place in the bulk). Various suitable anodes should be investigated to further check this idea.

Next, let us try to think about the role of reversibly cycled Li_2O . First of all, there is no doubt that the formation/decomposition of Li_2O provides charge transfer which absolutely increases the specific capacity of the anode. Moreover, Li_2O , as an electronic insulator, is one of the most important component of the SEI which has been reported by other researches¹²⁶. However, different from the views that the SEI blocks other irreversible reactions, dynamic SEI model could be more appropriate as it provides both increase of capacity and protection of the anode.

However, when we turn our attention to the electrolyte, the reversibly cycled Li_2O is not necessarily a desirable phenomenon. As discussed in equation 5.4 and 5.5, if the charge transfer derives from lithium salt, the reaction with the electrolyte could be also reversible. Thus, the redox shuttle would be $\text{ClO}_4^- / \text{ClO}_3^-$. However, if the charge transfer stems from solvent, the reaction of the electrolyte is irreversible. The solvent works as sacrificial reagent and the produced gases will possibly destroy the packaging of the battery in long-term application. Thus, the possible routine of chemical reaction should be processed via other technique such as in situ differential electrochemical mass spectrometry. On the other hand, one could also design the composition of the electrolyte to introduce other redox shuttles to optimize this dynamic SEI.

References

1. WMO. State of the global climate 2020[M]. *World Meteorol. Organ.* (2021).
2. Niclas D. Weimar. Energy Density and Specific Energy of Battery. <https://sinovoltaics.com/learning-center/storage/energy-density-and-specific-energy-of-battery/>.
3. Ioannis Tsiropoulos, Dalius Tarvydas & Natalia Lebedeva. *Li-ion batteries for mobility and stationary storage applications - Scenarios for costs and market growth* . (2018). doi:10.2760/8717.
4. FAA. National Blueprint for Runway Safety. 1–38 (2021).
5. Trasatti, S. 1799–1999: Alessandro Volta's 'Electric Pile'. *J. Electroanal. Chem.* **460**, 1–4 (1999).
6. Heng Z. et al. From Solid-Solution Electrodes and the Rocking-Chair Concept to Today's Batteries. *Angew.Chemie.Int.Ed.* **59**, 534–538 (2022).
7. Besenhard, J. O. & Eichinger, G. High energy density lithium cells. Part I. Electrolytes and anodes. *J. Electroanal. Chem.* **68**, 1–18 (1976).
8. Besenhard, J. O. & Eichinger, G. High energy density lithium cells. Part II Cathode and complete cells. *J. Electroanal. Chem.* **72**, 1–32 (1976).
9. Mizushima, K., Jones, P. C., Wiseman, P. J. & Goodenough, J. B. Li_xCoO_2 ($0 < x < 1$): A new cathode material for batteries of high energy density. *Solid State Ionics* **3–4**, 171–174 (1981).
10. Maier, J. Thermodynamics of electrochemical lithium storage. *Angew.Chemie.Int.Ed.* **52**, 4998–5026 (2013).
11. Goodenough, J. B. & Kim, Y. Challenges for rechargeable Li batteries. *Chem. Mater.* **22**, 587–603 (2010).
12. Goriparti, S. et al. Review on recent progress of nanostructured anode materials for Li-ion batteries. *J. Power Sources* **257**, 421–443 (2014).
13. Kwon, S. J., Lee, S. E., Lim, J. H., Choi, J. & Kim, J. Performance and life degradation characteristics analysis of NCM LIB for bess. *Electron.* **7**, 1–19 (2018).

14. Liu, D. H. *et al.* *Developing high safety Li-metal anodes for future high-energy Li-metal batteries: Strategies and perspectives. Chemical Society Reviews* vol. 49 (2020).
15. Zhang, X. Q., Cheng, X. B. & Zhang, Q. Advances in Interfaces between Li Metal Anode and Electrolyte. *Adv. Mater. Interfaces* **5**, (2018).
16. Xu, X. L. *et al.* The suppression of lithium dendrite growth in lithium sulfur batteries: A review. *J. Energy Storage* **13**, 387–400 (2017).
17. Li, W. *et al.* The synergetic effect of lithium polysulfide and lithium nitrate to prevent lithium dendrite growth. *Nat. Commun.* **6**, (2015).
18. Moradi, B. & Botte, G. G. Recycling of graphite anodes for the next generation of lithium ion batteries. *J. Appl. Electrochem.* **46**, 123–148 (2016).
19. Lijing Xie, Cheng Tang, Zhihong Bi, Mingxin Song, Yafeng Fan, Chong Yan, X. L. & Fangyuan Su,* Qiang Zhang, and C. C. Hard Carbon Anodes for Next-Generation Li-Ion Batteries Review and Perspective. 21016 (2021).
20. Zhao, L. F. *et al.* Hard Carbon Anodes: Fundamental Understanding and Commercial Perspectives for Na-Ion Batteries beyond Li-Ion and K-Ion Counterparts. *Adv. Energy Mater.* **11**, 1–28 (2021).
21. Zhang, C. *et al.* Strong anchoring effect of ferric chloride-graphite intercalation compounds (FeCl₃-GICs) with tailored epoxy groups for high-capacity and stable lithium storage. *J. Mater. Chem. A* **6**, 17982–17993 (2018).
22. Li, W., Sun, X. & Yu, Y. Si-, Ge-, Sn-Based Anode Materials for Lithium-Ion Batteries: From Structure Design to Electrochemical Performance. *Small Methods* **1**, (2017).
23. Eom, K. S. *et al.* Improved stability of nano-Sn electrode with high-quality nano-SEI formation for lithium ion battery. *Nano Energy* **12**, 314–321 (2015).
24. Xu, H. *et al.* Roll-to-roll prelithiation of Sn foil anode suppresses gassing and enables stable full-cell cycling of lithium ion batteries. *Energy Environ. Sci.* **12**, 2991–3000 (2019).
25. Zhang, M., Qiu, Y., Han, Y., Guo, Y. & Cheng, F. Three-dimensional tungsten nitride nanowires as high performance anode material for lithium ion batteries. *J. Power Sources* **322**, 163–168 (2016).
26. Wang, M., Weng, G. M., Yasin, G., Kumar, M. & Zhao, W. A high-performance tin

- phosphide/carbon composite anode for lithium-ion batteries. *Dalt. Trans.* **49**, 17026–17032 (2020).
27. Zhang, H. *et al.* $\text{Li}_4\text{Ti}_5\text{O}_{12}$ spinel anode: Fundamentals and advances in rechargeable batteries. *InfoMat* **4**, 1–29 (2022).
 28. Wang, X. *et al.* Ultralong-life and high-rate web-like $\text{Li}_4\text{Ti}_5\text{O}_{12}$ anode for high-performance flexible lithium-ion batteries. *Nano Res.* **7**, 1073–1082 (2014).
 29. Ferraresi, G. *et al.* SnO_2 Model Electrode Cycled in Li-Ion Battery Reveals the Formation of Li_2SnO_3 and Li_8SnO_6 Phases through Conversion Reactions. *ACS Appl. Mater. Interfaces* **10**, 8712–8720 (2018).
 30. Hu, R. *et al.* Dramatically enhanced reversibility of Li_2O in SnO_2 -based electrodes: The effect of nanostructure on high initial reversible capacity. *Energy Environ. Sci.* **9**, 595–603 (2016).
 31. Liu, C., Neale, Z. G. & Cao, G. Understanding electrochemical potentials of cathode materials in rechargeable batteries. *Mater. Today* **19**, 109–123 (2016).
 32. Zhou, S., Mei, T., Wang, X. & Qian, Y. Crystal structural design of exposed planes: Express channels, high-rate capability cathodes for lithium-ion batteries. *Nanoscale* **10**, 17435–17455 (2018).
 33. Chen, S., Jeong, S. R. & Tao, S. Key materials and future perspective for aqueous rechargeable lithium-ion batteries. *Mater. Reports Energy* **2**, 100096 (2022).
 34. Aboulaich, A. *et al.* Improving thermal and electrochemical performances of LiCoO_2 cathode at high cut-off charge potentials by MF_3 (M=Ce, Al) coating. *Mater. Res. Bull.* **73**, 362–368 (2016).
 35. Yu, L. *et al.* Investigation on the Overlithiation Mechanism of LiCoO_2 Cathode for Lithium Ion Batteries. *J. Electrochem. Soc.* **168**, 050516 (2021).
 36. Biasi, L. de & AlexanderSchiele, MariaRoca-Ayats, Grecia Garcia, Torsten Brezesinski, PascalHartmann, and J. Phase Transformation Behavior and Stability of LiNiO_2 Cathode Material for Li-Ion Batteries.pdf. *ChemSusChem* **12**, 2240–2250 (2019).
 37. Kim, H. *et al.* Role of Na^+ in the Cation Disorder of $[\text{Li}_{1-x}\text{Na}_x]\text{NiO}_2$ as a Cathode for Lithium-Ion Batteries. *J. Electrochem. Soc.* **165**, A201–A205 (2018).

38. Li, J. *et al.* Impact of the Synthesis Conditions on the Performance of $\text{LiNi}_x\text{Co}_y\text{Al}_z\text{O}_2$ with High Ni and Low Co Content . *J. Electrochem. Soc.* **165**, A3544–A3557 (2018).
39. Armstrong, A. R. & Bruce, P. G. ChemInform Abstract: Synthesis of Layered LiMnO_2 as an Electrode for Rechargeable Lithium Batteries. *ChemInform* **27**, 499–500 (2010).
40. Chen, Z., Chao, D., Lin, J. & Shen, Z. Recent progress in surface coating of layered $\text{LiNi}_x\text{Co}_y\text{Mn}_z\text{O}_2$ for lithium-ion batteries. *Mater. Res. Bull.* **96**, 491–502 (2017).
41. Manthiram, A., Song, B. & Li, W. A perspective on nickel-rich layered oxide cathodes for lithium-ion batteries. *Energy Storage Mater.* **6**, 125–139 (2017).
42. Shao-Lun Cui, Ming-Yue Gao, Guo-Ran Li, * and Xue-Ping Gao. Insights into Li-Rich Mn-Based Cathode Materials with High Capacity from.pdf. *Adv. Energy Mater.* **12**, 2003885 (2022).
43. Wang, Dong-Liang Peng, H. Z. H. G. L. L. Q. X. L. H. Recent developments and challenges of Li-rich Mn-based cathode materials for high-energy lithium-ion batteries. *Mater. today energy* **18**, 100518 (2020).
44. Yimeng Huang, Yanhao Dong, Sa Li, Jinhyuk Lee, Chao Wang, Zhi Zhu, W. X. & Yao Li, and J. L. Lithium Manganese Spinel Cathodes for Lithium-Ion Batteries. *Adv. Energy Mater.* **11**, 2000997 (2021).
45. Salpakari, J., Rasku, T., Lindgren, J. & Lund, P. D. Flexibility of electric vehicles and space heating in net zero energy houses: an optimal control model with thermal dynamics and battery degradation. *Appl. Energy* **190**, 800–812 (2017).
46. Zhang, W. J. Structure and performance of LiFePO_4 cathode materials: A review. *J. Power Sources* **196**, 2962–2970 (2011).
47. Wu, H., Liu, Q. & Guo, S. Composites of graphene and LiFePO_4 as cathode materials for lithium-ion battery: A mini-review. *Nano-Micro Lett.* **6**, 316–326 (2014).
48. Takalani, R. & Masisi, L. Energetic Macroscopic Representation Based Electric Bus Modelling and Energy Management Strategy. *IEEE Int. Symp. Ind. Electron.* **2022-June**, 955–958 (2022).
49. Xu, K. Nonaqueous liquid electrolytes for lithium-based rechargeable batteries. *Chem. Rev.* **104**, 4303–4417 (2004).

50. Fan, X. & Wang, C. High-voltage liquid electrolytes for Li batteries: progress and perspectives. *Chem. Soc. Rev.* **101**, (2021).
51. Song, J. Y., Wang, Y. Y. & Wan, C. C. Review of gel-type polymer electrolytes for lithium-ion batteries. *J. Power Sources* **77**, 183–197 (1999).
52. Cho, E. *et al.* Corrosion/passivation of aluminum current collector in bis(fluorosulfonyl) imide-based ionic liquid for lithium-ion batteries. *Electrochem. commun.* **22**, 1–3 (2012).
53. Wang, A., Kadam, S., Li, H., Shi, S. & Qi, Y. Review on modeling of the anode solid electrolyte interphase (SEI) for lithium-ion batteries. *npj Comput. Mater.* **4**, (2018).
54. An, S. J. *et al.* The state of understanding of the lithium-ion-battery graphite solid electrolyte interphase (SEI) and its relationship to formation cycling. *Carbon N. Y.* **105**, 52–76 (2016).
55. Peljo P, Girault H H. Electrochemical potential window of battery electrolytes: the HOMO–LUMO misconception[J]. *Energy & Environmental Science*, 2018, 11(9): 2306-2309.
56. Peled, E. The Electrochemical Behavior of Alkali and Alkaline Earth Metals in Nonaqueous Battery Systems—The Solid Electrolyte Interphase Model. *J. Electrochem. Soc.* **126**, 2047–2051 (1979).
57. E. Peled. Film forming reaction at the lithium/electrolyte interface. *J. Power Sources* **9**, 253–266 (1983).
58. Nazri, G. & Muller, R. H. Composition of Surface Layers on Li Electrodes in PC, LiClO₄ of Very Low Water Content. *J. Electrochem. Soc.* **132**, 2050–2054 (1985).
59. Aurbach, D., Daroux, M. L., Faguy, P. W. & Yeager, E. Identification of Surface Films Formed on Lithium in Propylene Carbonate Solutions. *J. Electrochem. Soc.* **134**, 1611–1620 (1987).
60. Peled, E., Golodnitsky, D. & Ardel, G. Advanced Model for Solid Electrolyte Interphase Electrodes in Liquid and Polymer Electrolytes. *J. Electrochem. Soc.* **144**, L208–L210 (1997).
61. Aurbach, D. *et al.* New insights into the interactions between electrode materials and electrolyte solutions for advanced nonaqueous batteries. *J. Power Sources* **81–82**, 95–111 (1999).
62. Edström, K., Herstedt, M. & Abraham, D. P. A new look at the solid electrolyte interphase on graphite anodes in Li-ion batteries. *J. Power Sources* **153**, 380–384 (2006).

63. Li, Y. *et al.* Atomic structure of sensitive battery materials and interfaces revealed by cryo-electron microscopy. *Science*. **358**, 506–510 (2017).
64. Zhou, Y. *et al.* Real-time mass spectrometric characterization of the solid–electrolyte interphase of a lithium-ion battery. *Nat. Nanotechnol.* **15**, 224–230 (2020).
65. Zhang, Z. *et al.* Capturing the swelling of solid-electrolyte interphase in lithium metal batteries. *Science*. **375**, 66–70 (2022).
66. Kitz, P. G., Novák, P. & Berg, E. J. Influence of Water Contamination on the SEI Formation in Li-Ion Cells: An Operando EQCM-D Study. *ACS Appl. Mater. Interfaces* **12**, 15934–15942 (2020).
67. Atkins, D. *et al.* Understanding Battery Interfaces by Combined Characterization and Simulation Approaches: Challenges and Perspectives. *Adv. Energy Mater.* **12**, (2022).
68. Shadike, Z. *et al.* Identification of LiH and nanocrystalline LiF in the solid–electrolyte interphase of lithium metal anodes. *Nat. Nanotechnol.* **16**, 549–554 (2021).
69. Bing Han, Zhen Zhang, Yucheng Zou, Kang Xu, Guiyin Xu, Hong Wang, Hong Meng, Yonghong Deng,* Ju Li, and M. G. Stability of Li_2CO_3 in the Solid Electrolyte Interphase of a Lithium-Metal Anode. *Adv. Energy Mater. energy Mater.* **33**, 2100404 (2021).
70. Ballauff, Sebastian Risse, et al. Surface structure inhibited lithiation of crystalline silicon probed with operando neutron reflectivity. *energy storage Mater.* **18**, 182–189 (2019).
71. Rus, E. D. & Dura, J. A. In Situ Neutron Reflectometry Study of Solid Electrolyte Interface (SEI) Formation on Tungsten Thin-Film Electrodes. *ACS Appl. Mater. Interfaces* **11**, 47553–47563 (2019).
72. Lim, L. Y., Liu, N., Cui, Y. & Toney, M. F. Understanding phase transformation in crystalline Ge anodes for Li-ion batteries. *Chem. Mater.* **26**, 3739–3746 (2014).
73. Kühne, M. *et al.* Reversible superdense ordering of lithium between two graphene sheets. *Nature* **564**, 234–239 (2018).
74. Han, B. *et al.* Additive stabilization of SEI on graphite observed using cryo-electron microscopy. *Energy Environ. Sci.* **14**, 4882–4889 (2021).
75. Ebner, M., Marone, F., Stampanoni, M. & Wood, V. of Electrochemical and Mechanical. *Science (80-.).* **342**, 716–721 (2013).

76. Beaulieu, L. Y., Hatchard, T. D., Bonakdarpour, A., Fleischauer, M. D. & Dahn, J. R. Reaction of Li with Alloy Thin Films Studied by In Situ AFM. *J. Electrochem. Soc.* **150**, A1457 (2003).
77. Schulz, N., Hausbrand, R., Wittich, C., Dimesso, L. & Jaegermann, W. XPS-Surface Analysis of SEI Layers on Li-Ion Cathodes: Part II. SEI-Composition and Formation inside Composite Electrodes. *J. Electrochem. Soc.* **165**, A833–A846 (2018).
78. Wood, K. N. & Teeter, G. XPS on Li-Battery-Related Compounds: Analysis of Inorganic SEI Phases and a Methodology for Charge Correction. *ACS Appl. Energy Mater.* **1**, 4493–4504 (2018).
79. Kalha, C. *et al.* Hard x-ray photoelectron spectroscopy: A snapshot of the state-of-the-art in 2020. *J. Phys. Condens. Matter* **33**, (2021).
80. Xiangsi Liu, Ziteng Liang, Yuxuan Xiang, Min Lin, Qi Li, Zigeng Liu, Guiming Zhong, Riqiang Fu, and Y. Y. Solid-State NMR and MRI Spectroscopy for Li Na Batteries Materials Interface and In.pdf. *Adv. Mater.* **33**, 202005878 (2021).
81. Shi, F. *et al.* A catalytic path for electrolyte reduction in lithium-ion cells revealed by in situ attenuated total reflection-fourier transform infrared spectroscopy. *J. Am. Chem. Soc.* **137**, 3181–3184 (2015).
82. Pengbo Zhai, Tianshuai Wang, Huaning Jiang, Jiayu Wan, Yi Wei, Lei Wang, Wei Liu, Qian Chen, Weiwei Yang, Yi Cui, * and Yongji Gong. Artificial Solid-Electrolyte Interphase for Lithium Metal Anodes Enabled by Insulator. *Adv. Mater.* **33**, 2006247 (2021).
83. Ma, C., Xu, F. & Song, T. Dual-Layered Interfacial Evolution of Lithium Metal Anode: SEI Analysis via TOF-SIMS Technology. *ACS Appl. Mater. Interfaces* **14**, 20197–20207 (2022).
84. Buttry, D. A. & Ward, M. D. Measurement of Interfacial Processes at Electrode Surfaces with the Electrochemical Quartz Crystal Microbalance. *Chem. Rev.* **92**, 1355–1379 (1992).
85. Sauerbrey, G. Verwendung von Schwingquarzen zur Wägung dünner Schichten und zur Mikrowägung. *Zeitschrift für Phys.* **155**, 206–222 (1959).
86. Ji, Y. *et al.* From bulk to interface: Electrochemical phenomena and mechanism studies in batteries: Via electrochemical quartz crystal microbalance. *Chem. Soc. Rev.* **50**, 10743–10763 (2021).
87. Yin, Z. W. *et al.* Revealing of the Activation Pathway and Cathode Electrolyte Interphase

- Evolution of Li-Rich $_{0.5}$ Li $_2$ MnO $_3$ · 0.5LiNi $_{0.3}$ Co $_{0.3}$ Mn $_{0.4}$ O $_2$ Cathode by in Situ Electrochemical Quartz Crystal Microbalance. *ACS Appl. Mater. Interfaces* **11**, 16214–16222 (2019).
88. Dargel, V. *et al.* In situ real-time gravimetric and viscoelastic probing of surface films formation on lithium batteries electrodes. *Nat. Commun.* **8**, (2017).
89. Wang, K., Joshi, Y., Chen, H. & Schmitz, G. In-situ analysis of solid-electrolyte interphase formation and cycle behavior of Sn battery anodes. *J. Power Sources* **535**, 231439 (2022).
90. Yang, Z., Dixon, M. C., Erck, R. A. & Trahey, L. Quantification of the mass and viscoelasticity of interfacial films on tin anodes using EQCM-D. *ACS Appl. Mater. Interfaces* **7**, 26585–26594 (2015).
91. Kohler, T., Hadjixenophontos, E., Joshi, Y., Wang, K. & Schmitz, G. Reversible oxide formation during cycling of Si anodes. *Nano Energy* **84**, 105886 (2021).
92. Liu, T. *et al.* In situ quantification of interphasial chemistry in Li-ion battery. *Nat. Nanotechnol.* **14**, 50–56 (2019).
93. Li, J. T., Chen, S. R., Fan, X. Y., Huang, L. & Sun, S. G. Studies of the interfacial properties of an electroplated Sn thin film electrode/electrolyte using in situ MFTIRS and EQCM. *Langmuir* **23**, 13174–13180 (2007).
94. Shpigel, N. *et al.* In situ hydrodynamic spectroscopy for structure characterization of porous energy storage electrodes. *Nat. Mater.* **15**, 570–575 (2016).
95. KaiYang, YiweiLi, LanglangJia, YanWang, ZijianWang, YuChenJi, ShichunYang, MagdaTitirici, XinhuaLiu, LuyiYang, F. Atomic/nano-scale in-situ probing the shuttling effect of redox mediator in Na–O $_2$ batteries. *J. Energy Chem.* **56**, 438–443 (2021).
96. Tomita, K., Noguchi, H. & Uosaki, K. Effect of Water and HF on the Distribution of Discharge Products at Li-O $_2$ Battery Cathode. *ACS Appl. Energy Mater.* **1**, 3434–3442 (2018).
97. Kitz, P. G., Lacey, M. J., Novák, P. & Berg, E. J. Operando investigation of the solid electrolyte interphase mechanical and transport properties formed from vinylene carbonate and fluoroethylene carbonate. *J. Power Sources* **477**, 0–8 (2020).
98. Keiji Kanazawa, K. & Gordon, J. G. The oscillation frequency of a quartz resonator in contact with liquid. *Anal. Chim. Acta* **175**, 99–105 (1985).
99. Shpigel, N. *et al.* In Situ Acoustic Diagnostics of Particle-Binder Interactions in Battery

- Electrodes. *Joule* **2**, 988–1003 (2018).
100. Shpigel, N. *et al.* In Situ Monitoring of Gravimetric and Viscoelastic Changes in 2D Intercalation Electrodes. *ACS Energy Lett.* **2**, 1407–1415 (2017).
 101. Levi, M. D. *et al.* In situ tracking of ion insertion in iron phosphate olivine electrodes via electrochemical quartz crystal admittance. *J. Phys. Chem. C* **117**, 1247–1256 (2013).
 102. Rodahl, M., Höök, F., Krozer, A., Brzezinski, P. & Kasemo, B. Quartz crystal microbalance setup for frequency and Q-factor measurements in gaseous and liquid environments. *Rev. Sci. Instrum.* **66**, 3924–3930 (1995).
 103. Shpigel, N., Levi, M. D., Sigalov, S., Daikhin, L. & Aurbach, D. In Situ Real-Time Mechanical and Morphological Characterization of Electrodes for Electrochemical Energy Storage and Conversion by Electrochemical Quartz Crystal Microbalance with Dissipation Monitoring. *Acc. Chem. Res.* **51**, 69–79 (2018).
 104. Terwort, J., Berkemeier, F. & Schmitz, G. $\text{Li}_x\text{V}_2\text{O}_5$ – Analysis of surface reactions by spectroscopic quartz crystal microgravimetry. *J. Power Sources* **336**, 172–178 (2016).
 105. Joshi, Y., Saksena, A., Hadjixenophontos, E., Schneider, J. M. & Schmitz, G. Electrochromic Behavior and Phase Transformation in $\text{Li}_{4+x}\text{Ti}_5\text{O}_{12}$ upon Lithium-Ion Deintercalation/Intercalation. *ACS Appl. Mater. Interfaces* **12**, 10616–10625 (2020).
 106. Aurbach, D. & Zaban, A. The application of EQCM to the study of the electrochemical behavior of propylene carbonate solutions. *J. Electroanal. Chem.* **393**, 43–53 (1995).
 107. Kamali, A. R. & Fray, D. J. Tin-based materials as advanced anode materials for lithium ion batteries: A review. *Rev. Adv. Mater. Sci.* **27**, 14–24 (2011).
 108. Qiao, R. *et al.* Distinct Solid-Electrolyte-Interphases on Sn (100) and (001) Electrodes Studied by Soft X-Ray Spectroscopy. *Adv. Mater. Interfaces* **1**, 1–6 (2014).
 109. Nimisha, C. S., Venkatesh, G., Rao, K. Y., Rao, G. M. & Munichandraiah, N. Morphology dependent electrochemical performance of sputter deposited Sn thin films. *Mater. Res. Bull.* **47**, 1950–1953 (2012).
 110. Wu, M. *et al.* Fabrication of Sn film via magnetron sputtering towards understanding electrochemical behavior in lithium-ion battery application. *Electrochim. Acta* **123**, 144–150 (2014).

111. Li, Q. *et al.* Study of copper foam-supported Sn thin film as a high-capacity anode for lithium-ion batteries. *Electrochim. Acta* **54**, 5884–5888 (2009).
112. Cao, C. *et al.* Solid Electrolyte Interphase on Native Oxide-Terminated Silicon Anodes for Li-Ion Batteries. *Joule* **3**, 762–781 (2019).
113. Chao, S. C. *et al.* A study on the interior microstructures of working Sn particle electrode of Li-ion batteries by in situ X-ray transmission microscopy. *Electrochem. commun.* **12**, 234–237 (2010).
114. Bach, P., Stratmann, M., Valencia-Jaime, I., Romero, A. H. & Renner, F. U. Lithiation and delithiation mechanisms of gold thin film model anodes for lithium ion batteries: Electrochemical characterization. *Electrochim. Acta* **164**, 81–89 (2015).
115. Wu, F., Maier, J. & Yu, Y. Guidelines and trends for next-generation rechargeable lithium and lithium-ion batteries. *Chem. Soc. Rev.* **49**, 1569–1614 (2020).
116. Xiao, X. *et al.* Nanostructured Germanium Anode Materials for Advanced Rechargeable Batteries. *Adv. Mater. Interfaces* **4**, (2017).
117. Yoon, T. *et al.* Intramolecular deformation of zeotype-borogermanate toward a three-dimensional porous germanium anode for high-rate lithium storage. *J. Mater. Chem. A* **6**, 15961–15967 (2018).
118. Yu, Q. *et al.* Constructing Effective Interfaces for Li 1.5 Al_{0.5} Ge_{1.5} (PO₄)₃ Pellets to Achieve Room-temperature Hybrid Solid-State Lithium Metal Batteries. *ACS Appl. Mater. Interfaces* **11**, 9911–9918 (2019).
119. De Klerk, N. J. J. & Wagemaker, M. Space-Charge Layers in All-Solid-State Batteries; Important or Negligible? *ACS Appl. Energy Mater.* **1**, 5609–5618 (2018).
120. Raijmakers, L. H. J., Danilov, D. L., Eichel, R. A. & Notten, P. H. L. An advanced all-solid-state Li-ion battery model. *Electrochim. Acta* **330**, 135147 (2020).
121. Morris, A. J., Grey, C. P. & Pickard, C. J. Thermodynamically stable lithium silicides and germanides from density functional theory calculations. *Phys. Rev. B - Condens. Matter Mater. Phys.* **90**, 22–24 (2014).
122. Graetz, J., Ahn, C. C., Yazami, R. & Fultz, B. Nanocrystalline and Thin Film Germanium Electrodes with High Lithium Capacity and High Rate Capabilities. *J. Electrochem. Soc.* **151**,

- A698 (2004).
123. Ozanam, F. & Rosso, M. Silicon as anode material for Li-ion batteries. *Mater. Sci. Eng. B Solid-State Mater. Adv. Technol.* **213**, 2–11 (2016).
 124. Porter, D. A., Easterling, K. E. & Sherif, M. Y. *Phase transformations in metals and alloys, third edition. Phase Transformations in Metals and Alloys, Third Edition* (2009).
 125. López-García, J. J., Horno, J. & Grosse, C. Poisson-Boltzmann description of the electrical double layer including ion size effects. *Langmuir* **27**, 13970–13974 (2011).
 126. Guo, R. & Gallant, B. M. Li₂O Solid Electrolyte Interphase: Probing Transport Properties at the Chemical Potential of Lithium. *Chem. Mater.* **32**, 5525–5533 (2020).

Acknowledgement

It is a long way to finish my PhD thesis and put it in front of you. Tracking back to ten years ago, with an interest in science, a boy chose materials science and try to open a brand new world. Although, the road of exploration is full of challenges, all the way until now, I would like to thank a lot of people.

First, I would like to thank Prof. Dr. Dr. h.c. Guido Schmitz for giving me an opportunity to study in his group and carry out my thesis. I still remember that he always guided me to think more logically, and never blame me. I am also grateful for all the fruitful discussions, without his help, I could not accomplish this thesis. Furthermore, I want to acknowledge Prof. Dr. Joachim Maier as my second examiner, for his deeply insightful comments and suggestions which helped me a lot. I also want to express my gratitude to Prof. Dr. Oliver Clemens for his willingness to chair the examination committee.

I am thankful to Yug joshi for the fruitful discussions which helped me a quite lot during my PhD study. I would also like to express my acknowledgement to not only to my colleague but also my family in Stuttgart: Helena, Yoonhee, Sam, Jianshu, Ahmed, Ruya, Kuan, Robert, Peter, Frank, Jackie and Patrick. I would specially like to thank Efi and Tobias who helped me a quite lot in the beginning of my PhD.

Outside of the lab, I would like to thank my friends: Rui, Hong, Jie, Peiwen, Xin, Kun, Wansheng, Weiwei, Chunhui, Xiang and Zhen who always listens to my complaints and give me many encouragements. Around 4 years of studying abroad, I have never felt lonely.

I also would like to honor the never-ending love of my families. Their encouragements and supports make my life easier and more wonderful.

Last but not least. I want to thank myself for overcoming many kinds of difficulties and finishing this dissertation. But that doesn't mean stopping on the way to the science. I do not have too huge dreams. If I can make some positive changes for battery development, my life has been worth living.

Ke Wang

Stuttgart, 03. 10. 2022

Appendix

Matlab for the data analysis (shown in chapter 2.4)

Data basic parameters

```

%CV data
%Number of halfcycles+1, so 50 cycles are numbcycles = 101
numbcycles = :;
%Number of datapoints
datapoints = :;
%define volume of sample in cm^3
V = 50*10^-7*1.4113;
%define sweeprate in V/s
%sweeprate = 0.0005;

%QCM data|
%active area of the resonator ((resonating area)/(area of electrode))
activearea = 0.28969;
%sensitivity of the resonator
sensitivity = 1.767*10^-8;
%area of the active resonator region
surfarea = 0.41753;
%corrected time of QCM in seconds
coritime = QCMdata(:,1)*60;
%frequency change
freqchange = QCMdata(:,2);

```

File separation

```

%Counts the halfcycles
i = 1;

%Counts the datapoints
m = 1;

%Creates an array were the separated data is stored
halfcycle = cell(numbcycles,1);

%Current value stored in c for cut critereon
c = CVdata(m,9);

```

```
%Loop that continues until all CV cycles are done
while i < numbcycles

    %Counts the datapoints in the new file
    n = 1;

    %Loop to store the negative halfcycles (critereon is negative current)
    while c < 0
        %Save one datapoint in from old to new file
        halfcycle{i}(n,1:12) = CVdata(m,1:12);
        %Count upwards for next datapoint and get new c for cut critereon
        n = n+1;
        m = m+1;
        c = CVdata(m,9);
    end

    %Next halfcycle
    i = i+1;

    %Set back n to one since new row in the array will beginn
    n = 1;

    %Loop to store positive halfcycles (with positive current)
    while c > 0
        %Save datapoint from old to new file
        halfcycle{i}(n,1:12) = CVdata(m,1:12);
        %Count upwards for new datapoint
        n = n+1;

        %Only proceed if there are still datapoints left in the CVdata file
        if m < datapoints
            m = m+1;
            c = CVdata(m,9);
        %If all datapoints are processed, end the skript
        else
            break;
        end
    end

    %Count upwards for next halfcycle
    i = i+1;
end
```

Charge integration

```

%create array for each charge curve of each halfcycle
chargehalfcycle = cell(numbcycles,1);

%define loop parameter
i = 1;

%define charge uptake and release
mp = 1;

%calculation for each halfcycle
while i < numbcycles
    %Calculation of charge by Q = (1/v)*(I dt)
    %chargehalfcycle{i} = mp*(1/sweepirate)*cumtrapz(halfcycle{i}(:,8),0.001*halfcycle{i}(:,9));
    %Calculation of charge by Q = activepartofresonator*(I dt)
    chargehalfcycle{i} = activearea*cumtrapz(halfcycle{i}(:,6),0.001*halfcycle{i}(:,9));
    i = i+1;
    %change sign for next halfcycle
    %mp = mp*(-1);
end

```

Cycle capacity

```

%create array for each charge curve of each halfcycle
%capacityhalfcycle = cell(63,1);

%define loop parameter
i = 1;

%define charge uptake and release
o = 1;

%calculation for each halfcycle
while i < numbcycles
    %Calculation of specific capacity by C = (1/V)* I dt in mAh/cm^3
    capacityhalfcycle(o,1) = (1/(V*3600))*10^3*trapz(halfcycle{i}(:,6),0.001*halfcycle{i}(:,9));
    i = i+1;
    if i < numbcycles
        capacityhalfcycle(o,2) = (1/(V*3600))*10^3*trapz(halfcycle{i}(:,6),0.001*halfcycle{i}(:,9));
        o = o+1;
        i = i+1;
    else
        break;
    end
end

plot(abs(capacityhalfcycle), 's', 'MarkerSize', 8, 'linewidth', 2);
xlabel('cycle number');
ylabel('{\it C} [mAh/cm^{3}]');
legend('delithiation', 'lithiation');

```

CV mass (mass by charge)

```
%calculation of the mass by the charge with the assumption of Li+ as the
%only ion that delivers the charge

%calculation of mass by m = activeareaofresonator*(mLi/e)*(I dt)
massbycharge = -(activearea*(1.15258*10^-23)/(1.602177*10^-19))*cumtrapz(CVdata(:,6),0.001*CVdata(:,9));

%plot mass change according to CV vs. time
plot(CVdata(:,6),massbycharge,'linewidth',1.2);
xlabel('\it t [s]');
ylabel('\it \Deltam [g]');
```

QCM mass

```
%calculate masschange = frequencychange*sensitivity*surface area
masschange = -freqchange*sensitivity*surfarea;

%plot frequency change vs. corrected time
figure;
axis tight
figure
plot(corrtime,freqchange,'linewidth',1.2);
xlabel('\it t [s]');
ylabel('\it \Deltaf [Hz]');
ylim([-25000 20000]);
%plot mass change by QCM and mass change by charge in one diagrammV, surfarea, sensitivity
figure;
plot(corrtime,masschange,'linewidth',1.2);
hold on;
massbycharge = -(activearea*(1.15258*10^-23)/(1.602177*10^-19))*cumtrapz(CVdata(:,6),0.001*CVdata(:,9));

%plot mass change according to CV vs. time
plot(CVdata(:,6),massbycharge,'linewidth',1.2);
xlabel('\it t [s]');
ylabel('\it \Deltam [g]');
ylim([-0.0005 0.0005]);
legend('Mass from QCM','Mass calculated from charge');
```

MPE (mass per charge)

```
%interpolate the masschange to get same matrix size as of the CV data
intmasschange = interp1(corrtime,masschange,CVdata(1:datapoints,6));

%store data of chargehalfcycle from the array to a double
k = 1;
l = 1;
u = 1;
p = 1;

while k < datapoints
    if u > length(chargehalfcycle)
        break;
    elseif p <= length(chargehalfcycle(u))
        intchargehalfcycle(l,1) = chargehalfcycle(u)(p,1);
        k = k+1;
        l = k;
        p = p+1;
    else
        u = u+1;
        p = 1;
    end
end
```

```

%differentiate the interpolated mass change and the double charge half
%cycle. Additionally the mass is multiplied by the faraday constant
diffintmasstimesF = (96485.3329*diff(intmasschange(1:datapoints-1,1)));
diffintchargehalfcycle = abs(diff(intchargehalfcycle));

%divide the change of masschange*F by the change in the charge of each
%halfcycle to get the mass per charge
q = 1;

while q < datapoints-3
    masspercharge(q,1) = diffintmasstimesF(q,1)/diffintchargehalfcycle(q,1);
    q = q+1;
end

%Smoothing of the masspercharge
smoothed = smoothdata(masspercharge, 'sgolay', 'SmoothingFactor', 0.001);

%plotting mpe and also the potential in one figure
figure;
%first subplot for mpe curve
subplot(3,1,1:2);
plot(CVdata(1:datapoints-4,6), smoothed(1:datapoints-4,1));
line([0 1000000], [7 7], 'color', 'red', 'linestyle', '--');
line([0 1000000], [-7 -7], 'color', 'red', 'linestyle', '--');
line([0 1000000], [14.9 14.9], 'color', 'red', 'linestyle', '--');
line([0 1000000], [-14.9 -14.9], 'color', 'red', 'linestyle', '--');
ylabel('\itM/z [g/mol]');
ylim([-50 150]);
yticks([-50 -40 -30 -20 -10 0 10 20 30 40 50 60 70 80 90]);
%set(gca, 'xticklabel', []);
%second subplot for potential vs. time
subplot(3,1,3);
plot(CVdata(1:datapoints-4,6), CVdata(1:datapoints-4,8));
xlabel('time [s]');
ylabel('\it E vs. Li/Li^{+} [V]');
axis tight;
%link the x-axis which simplifies zooming in the picture
linkaxes([subplot(3,1,1:2) subplot(3,1,3)], 'x');

```

QCM mass spectra

```

%define lower and upper limit for the mass spectrum, s is defined in
%halfcycles
s = 1;
lowerlim = 1;

while s < 7,
    lowerlim = lowerlim + length(halfcycle(s));
    s = s+1;
end

upperlim = lowerlim;

while s < 11,
    upperlim = upperlim + length(halfcycle(s));
    s = s+1;
end

%smooth the masspercharge curve within the chosen limits
shortmasspercharge = smoothed(lowerlim:upperlim-5);

%Massspectrum
%calculating the masspercharge value for a specific time intervall
%calculating the mean mpe value for tint values
tint = 1;
lowt = 1;
i = 1;
while lowt < length(shortmasspercharge)-tint,
    tintmpe(i,1) = (1/(tint+1))*(sum(shortmasspercharge(lowt:lowt+tint)));
    i = i+1;
    lowt = lowt + tint+1;
end

%calculating the mass change during this tint
lowt = 1;
i = 1;
cutmasschange = intmasschange(lowerlim:upperlim-5);

```



```

while lowt < length(cutmasschange)-tint
    tintmasschange(i,1) = cutmasschange(lowt+tint,1)-cutmasschange(lowt,1);
    i = i+1;
    lowt = lowt + tint+1;
end

%calculating the number of molecules/atoms during the intervall tint
i = 1;
while i < length(tintmasschange)
    numatoms(i,1) = (6.02214*10^23)*(tintmasschange(i,1)/tintmpe(i,1));
    i = i+1;
end

%calculating the resulting mass spectrum
massspectrum(1:length(numatoms),1) = tintmpe(1:length(numatoms),1);
massspectrum(1:length(numatoms),2) = numatoms(:,1);
%massspectrum will be not sorted for mpe values. This happens here:
sortedmassspectrum = sortrows(massspectrum,1);
%calculate the final massspectrum with a stepsize of s
i = -90;
m = 1;
n = 1;
s = 0.5;
%define the variable finalmassspectrum
finalmassspectrum = zeros((180/s)+1,2);
finalmassspectrum(:,1) = [-90:s:90];

%add up the values that are within the intervall of s in terms of mpes
while i < 90.1
    if n > length(sortedmassspectrum)
        break;
    else
        if i > sortedmassspectrum(n,1)
            finalmassspectrum(m,2) = finalmassspectrum(m,2) + sortedmassspectrum(n,2);
            n = n + 1;

        else
            m = m + 1;
            i = i + s;
        end
    end
end
end

```

```
%plotting the massspectrum
figure;
plot(finalmassspectrum(:,1),finalmassspectrum(:,2)/4.2,'LineWidth',1.5);
xticks(-90:10:90);
ylim([-10000 5*10^18]);
xlabel('{\itM/z} [g/mol]','FontSize',12);
ylabel('number of ions per cycle per cm^2','FontSize',12);
line([7 7],[-10000 10^19],'color','red','linestyle','--');
line([-7 -7],[-10000 10^19],'color','red','linestyle','--');
set(gca,'FontSize',12)
legend('cycle 1 to 1');
```

List of Figures

Figure 1.1: (a) Specific Energy densities of different kinds batteries (source: www.epectc.com), (b) Annual sales of the electric vehicle (source: BloombergNEF Long-Term Electric Vehicle Outlook 2019).	2
Figure 1.2: (a) Discharging and (b) charging of a lithium ion battery.....	3
Figure 1.3: Comparison between specific capacity and operating potential of various anode materials (a) ¹² and cathode materials (b) ¹³	5
Figure 1.4: Schematic energy diagram of an aqueous electrolyte. (a) Φ_A and Φ_C are the work function of anode and cathode, respectively; E_g is the thermodynamic stability window of electrolyte; μ_A and μ_C are the redox potential of the anode and cathode, respectively. A $\mu_A > \text{LUMO}$ or $\mu_C < \text{HOMO}$ requires a kinetic stability by the formation of an SEI layer ¹¹ . (b) the electrochemical stability of electrolytes was corrected to the potential of electrolyte reduction at negative potentials, and of potential of solvent oxidation at positive potentials ⁵⁵	14
Figure 1.5: A brief history of SEI on anode.	16
Figure 1.6: An overview of different characterization to study the SEI formation ⁶⁷	17
Figure 1.7: An external electrical field induces strain in an acentric AT-cut quartz single crystal (a) and (b). Resonance wavelength increase with layer deposition on the sensor surface (c) and (d).	22
Figure 2.1: Schematics of (a) the DC ion beam sputtering and (b) the RF ion beam sputtering.	28
Figure 2.2: Scheme of (a) the working electrode and (b) of the setup for the CV-QCM measurement with the working electrode at the bottom.	33
Figure 3.1: The (a) SEM surface image, (b) TEM cross section micrograph and (c) XRD pattern of as-deposited 100 nm Sn.	38
Figure 3.2: (a) CV curves of different cycles and (b) electrochemical capacity of a 100 nm Sn electrode at a scan rate of 0.5 mV/s in a potential window of 0.1-1.5V.....	39
Figure 3.3: (a) Mass change during CV measured by QCM (black) and calculated from CV (red). (b) shows the irreversible mass change (SEI mass change) per cycle (stage I: 1 st cycle, stage II: 2 nd -5 th cycles, stage III: 6 th -45 th cycles) and stage IV: 46 th - 100 th cycles).	40

Figure 3.4: (a) TEM micrograph of 100 nm Sn after cycling, labeled with the thickness of SEI layer and (b) the corresponding EDX mapping of the TEM micrograph (Au (red), Cu (Pink) and Sn (Blue)).	42
Figure 3.5: The over-all QCM mass spectrum.	44
Figure 3.6: (a) The mass spectra of first stage (1 st cycle), (b) CV curve, (c) real MPE curve and (c) average MPE curve of 1 st cycle	49
Figure 3.7: (a) The mass spectra of second stage (2 nd – 5 th cycles), (b) CV curve, (c) real time MPE curve and (c) integrated MPE curve of 2 nd cycle	51
Figure 3.8: (a) The mass spectrum of third stage (6 th – 45 th cycles), (b) CV curve, (c) real time MPE curve and (c) integrated MPE curve of 20 th cycle.	52
Figure 3.9: (a) The mass spectrum of fourth stage (46 th – 100 th cycles), (b) CV curve, (c) real time MPE curve and (c) integrated MPE curve of 80 th cycle.	53
Figure 3.10: The mass change for every half cycle calculated by QCM and CV for (a) the lithiation half cycle and (b) the delithiation half cycle. (c) The ratio between QCM mass change and CV mass change for every half cycle and (d) The Coulombic Efficiency (CE), the Mass Efficiency (ME) and the ratio of ME to CE	55
Figure 3.11: (a) XRD pattern of substrate (logarithmic intensity axis), as-deposited Sn on substrate (quartz, Ti and Au) and the electrode after cycling. (b) TEM micrograph of 100 nm Sn after cycling and (c) The diffraction pattern corresponding to the red cycle in the TEM micrograph.	58
Figure 3.12: XPS data of surface (top (a), (b) and (c)) and volume of the SEI (bottom (d), (e) and (f)). (a) and (d) show the binding energy around the lithium 1s peak; (b) and (e) the binding energy around oxygen 1s peak; (c) and (f) the binding energy close to tin 3d peak.	59
Figure 3.13: Characterization of 100 nm SnO _x anode prepared by ion-beam sputter (a) SEM image, (b) TEM cross section micrograph and (c) XRD pattern of SnO _x .	60
Figure 3.14: (a). Mass change measured by QCM and (b) over-all QCM mass spectrum of SnO _x .	61
Figure 3.15: Schematics of long-term cycling and SEI formation of Sn.	62
Figure 4.1: CV curves of a 100 nm Sn electrode at a scan rate of 0.5 mV/s in a potential window of 0.1-1.5V (1 st , 2 nd , 20 th and 80 th are selected to represent different stage, respectively).	65
Figure 4.2: SEM surface images of different thickness of Sn (a) 20 nm, (b) 50 nm, (c) 100 nm and (d) 150 nm.	66

- Figure 4.3:** CV curves of different cycles as labeled for Sn thicknesses 20 nm (a), 50 nm (b), 100 nm (c) and 150 nm (d); Electrochemical capacity of Sn electrodes of different thickness (a') 20 nm, (b') 50 nm, (c') 100 nm and (d') 150 nm at a scan rate of 0.5 mV/s in a potential window of 0.1 - 1.5 V..... 68
- Figure 4.4:** Mass spectra of 20 nm Sn after (a) 1st cycle (stage I), (b) 2nd-5th cycles (stage II), (c) 6th-45th cycles (stage III) and (d) 46th - 100th cycles (stage IV). 70
- Figure 4.5:** Real-time MPE curve of 20 nm Sn (a) 1st cycle (stage I), (c) 2nd cycle (stage II), (d) 20th cycle (stage III) and (d) 80th cycle (stage IV). 71
- Figure 4.6:** The integrated MPE of (a) 1st cycle (stage I), (b) 2nd cycle (stage II), (c) 20th cycle (stage III) and (d) 80th cycle (stage IV). Solid lines mark the MPE during lithiation half cycle, while dotted lines represent the MPE during delithiation half cycle. 72
- Figure 4.7:** (a) Mass changes of different sample thicknesses (20 nm, 50 nm, 100 nm, and 150 nm) measured by QCM from the 1st cycle to the 100th cycle. (b-e) TEM micrographs of electrodes of different thickness after 100 cycles (b) 20 nm, (c) 50 nm, (d) 100 nm and (e) 150 nm..... 73
- Figure 4.8:** The relationship between initial Sn thickness with SEI thickness after 100 cycles as determined by TEM measurement (a), and SEI mass per area after 100 cycles as measured by QCM, the over-all QCM mass spectra of different thickness Sn (c) 20 nm, (d) 50 nm, (e) 100 nm and (f) 150 nm. The exact positions of the delithiation peaks are labeled within the figures. 77
- Figure 4.9:** Relationship between sample thickness and transferred charge during delithiation (from the 1st – 100th cycle) at a scan rate of 0.5 mV/s. 78
- Figure 4.10:** The reversible mass change observed for different Sn thickness (a) 20 nm, (b) 50 nm, (c) 100 nm and (d) 150 nm measured by QCM (black), calculated from CV under assumption of purely lithiation (red), derived from CV under assumption of given ratio (as labeled) between Li₂O and Li (blue) and (f) the dependence of the absolute mass of reversibly cycled Li₂O versus the Sn thickness..... 81
- Figure 4.11:** (a) CV curves of a 100 nm Sn electrode at a scan rate of 0.5 mV/s in a potential window of 0.01-1.5 V after 100 cycle. (b) TEM micrograph of Sn_{0.01} after cycling, (c) the corresponding EDX mapping of the TEM micrograph (Au (red), Cu (Pink) and Sn (Blue))..... 81
- Figure 4.12:** XPS data of the 100 nm Sn films processed to different voltage. The data are directly measured from the surface of electrode without any sputtering: First column (a, d) shows the binding energy of carbon 1s peak, second (b, e) the binding energy of oxygen 1s peak and third column (c, f): the binding energy of lithium 1s peak. The top row (a, b and c) shows the result after one complete cycle and subsequent lithiation to

- 0.4 V vs Li/Li⁺, the bottom raw (d, e and f) after one complete cycle and subsequent lithiation to 0.2 V vs Li/Li⁺. 82
- Figure 4.13:** CV curves of a 100 nm Sn electrode cycled at 0.5 mV/s in a potential window of (a) 0.1 to 1.5 V, (b) 0.2 to 1.5 V and (c) 0.4 to 1.5 V, and (g) the corresponding QCM mass changes (0.1 - 1.5 V, 0.2 - 1.5 V and 0.4 - 1.5 V). 84
- Figure 4.14:** SEM images of (a) Sn0.1, (b) Sn0.2, (c) Sn0.4 and (d) XRD pattern of substrate, bare Sn and electrodes after respectively cycling down to 0.1 V, 0.2 V or 0.4 V. 86
- Figure 4.15:** XPS data of the Sn anode after 100 cycles of- first raw. (a) - (a'') the surface on Sn-0.1, second raw (b) - (b'') the surface on Sn0.4, third raw (c) - (c'') the volume in Sn-0.1 and last raw (d) - (d'') the volume in Sn-0.4. First column (a) - (d) show the binding energy around the lithium 1s peak; middle column (a') - (d') the binding energy around oxygen 1s peak; last column (a'') - (d'') the binding energy close to tin 3d peak. 88
- Figure 4.16:** Schematic of SEI formation and cycling behavior on Sn 89
- Figure 5.1:** The (a) SEM image and (b) TEM cross section micrograph of 100 nm Ge electrode; (c) the CV curve and (d) electrochemical capacity of a 100 nm Ge film at a scan rate of 0.5 mV/s in the potential window of 0.1 - 1.5 V; (e) the SEM image and (f) TEM cross section micrograph of 100 nm Ge electrode after 100 cycles. 93
- Figure 5.2:** (a) The mass change of a 100 nm Ge cycled between 0.1 and 1.5 V as measured by QCM, (b) the real-time MPE and (c) the integrated MPE of the 1st cycle, (d) the mass spectrum obtained between the 1st to 40th cycles, (e) the real-time MPE curve and (f) the integrated MPE curve of the 10th cycle. 96
- Figure 5.3: CV curve of 100 nm Ge thin film: sample 1 (a) one complete cycle and subsequently lithiated to 0.45V vs Li/Li⁺; sample 2 (a') one complete cycle and stop at voltage of 1.5 V vs Li/Li⁺; XPS data of sample 1 ((b'), (c') and (d')) and sample 2 ((b), (c) and (d)). (b) and (b') shows the binding energy around the lithium 1s peak; (c) and (c') show the binding energy around oxygen 1s peak; (d) and (d') show the binding energy close to the binding energy to Ge 3d peak. 97
- Figure 5.4: (a) The mass change of 100Ge-0.1 (black) and 100Ge-0.3 (purple); (b) the SEM of the surface of 100Ge-0.3; (c) Less magnified TEM image of the cross section of 100Ge-0.3; (d) higher magnified TEM image of the area highlighted in red in subfigure (c); The amplitude of the reversible QCM mass change (black), the CV mass change (green) and the ratio between both (blue, note different y-axes) in the case of (e) 100Ge-0.1 and (f) 100Ge-0.3, (g) the mass of reversibly processed Li₂O on 100Ge-0.1 as a function of the half cycle number, (h) the amount of reversibly processed Li and Li₂O at the 10th cycle of 100Ge-0.1 and 100Ge-0.3. 99

- Figure 5.5:** The cycling capacity (a) and mass change (b) of 20Ge-0.3 and 100Ge-0.3, the SEM surface image (c) and TEM cross section (d) of 20Ge-0.3 after cycling, (e) The amplitude of the QCM mass change (black), the CV mass (green) change and the ratio between both (blue) for the 20 nm Ge and (f) the amount of Li and Li₂O at the 20th cycle of 20Ge-0.3 and 100Ge-0.3..... 101
- Figure 5.6:** (a) The CV curves, (b) the mass change curve, (c) the cycle capacity and (d) the ratio of LiO_{0.5} /Li, (e) the absolute amounts of Li and LiO_{0.5} of 20Ge-0.3 cycled at different scan rates, (f) the position of delithiation peak. 102
- Figure 5.7:** (a) Mass change from CV and QCM of 20 nm Si at a scan rate of 0.5 mV/s in the potential window of 0.1 - 1.5 V⁹¹, (b) The amplitude of the QCM mass change (black), of CV mass (green) change and the ratio between QCM amplitude and CV amplitude (blue) of 20 nm Si, (c) the amount of reversibly cycle Li₂O on 20 nm Si and 20 nm Ge. 103
- Figure 5.8** (a) Schematic of the voltage profiles established during intercalation: potential in the electrolyte (solid yellow), equilibrium potential of intercalation (solid black), the Butler-Volmer (B.V.) drop in fast (red dotted) and slow scanning (yellow dotted). The blue short-dashed line, the violet short-dotted line, the green long-dashed line and the red dashed-dotted line represents the potential applied to the electrode in case of slow scanning in Ge, slow scanning in Si, slow scanning in thick Ge electrode and fast scanning in Ge electrode, respectively. The higher is the potential difference ΔV across the Li₂O layer, the more is the driving force (as it drives more electrons) for the chemical reaction to form the oxide as shown in Eq. 5.4. (b) Schematic representation of the effect of different lithiation potentials of Si (violet solid) and Ge (blue solid) when applying a voltage in between the two insertion potentials. At intermediate applied voltage, Lithiation is already possible in case of Ge, whereas in the case of Si, only Li₂O formation can take place. (c) Schematic representation of the lithiation voltage in a general electrode. As the thickness of Li₂O layer increases (Δx_{Li_2O}) the net field i.e. gradient in potential decreases thereby decelerating the growth of Li₂O. Whereas in (d), the opposite case can be seen during delithiation that, once the voltage drop is established the field responsible for the dissolution only increases as the thickness of Li₂O is reduced until it vanishes. In (c) and (d), point A is controlled by the equilibrium voltage or OCV (in accordance to Poisson's equation for the formation of electrical double layer, B is controlled by the B.V. overpotential, C is controlled by the applied voltage, and D is the OCV/equilibrium voltage. 106

List of Tables

Table 1.1: Overview of typical electrolyte solvent used in LIB.....	11
Table 1.2: Overview of lithium slats used in LIB.....	12
Table 1.3: summary of works reported by combining QCM and other in situ techniques..	24
Table 3.1: Chemical composition and corresponding MPE values for expect species in the LiClO ₄ /EC + DMC electrolyte.	48
Table 4.1: The comparison between QCM and TEM results on the SEI thickness and the resulting average density.....	74
Table 4.2: The densities of possible species of the SEI.....	79
Table 5.1: Parameter comparison of Si and Ge ¹²¹⁻¹²⁴	104

List of publications (2019-2022)

1. Kohler T, Hadjixenophontos E, Joshi Y, Ke W et al. Reversible oxide formation during cycling of Si anodes[J]. Nano Energy, 2021, 84: 105886.
2. Wang K, Joshi Y, Chen H, et al. In-situ analysis of solid-electrolyte interphase formation and cycle behavior of Sn battery anodes[J]. Journal of Power Sources, 2022, 535: 231439.
3. Wang K, Joshi Y, Chen H, et al. Quantitative investigation of the cycling behavior and SEI formation of tin anode through time-resolved microgravimetry. Journal of Power Sources **under review (minor revision)**
4. Wang K, Joshi Y, Guido Schmitz Reversible Li_2O formation on Germanium battery anodes. **Submitted**

Curriculum vitae

- Name: Ke Wang
- Telephone: +491638322706
- Date of birth: 05.02.1994
- Email: Ke.Wang@mp.imw.uni-stuttgart.de
- Address: Heisenbergstr. 3 70569 Stuttgart, Germany



Education

01.04.2019 - now	University of Stuttgart	PhD	Material Physics
01.09.2012 – 31.12.2018	University of Zhengzhou	Master and Bachelor	Material science and engineering

Skills

Hardware: Raman, FT-IR, TEM, SEM, FIB, XRD, Ion-Beam Sputter deposition, Electrochemical Workstation, Mechanical Lathe, Quartz Crystal Microbalance, UV-Vis absorption and Reflection.

Software: Office, 3Dmax, Photoshop, Matlab, Origin and Chemdraw.

Tutor (supervisor in laboratory course)

Photolithography and Liquid Crystal display

White-Light Interferometry

Ion-beam sputter deposition